Measurement of (n, γ)-Rates of Light Neutron-Rich Nuclei for the r-Process Nucleosynthesis

Messung von (n, γ)-Übergangsraten Leichter Neutronenreicher Kerne für die r-Prozeß Nukleosynthese
Zur Erlangung des Grades eines Doktors der Naturwissenschaften (Dr. rer. nat.)
genehmigte Dissertation von Dipl.-Phys. Marcel Heine aus Bad Muskau
2015 — Darmstadt — D 17

TECHNISCHE
UNIVERSITÄT
DARMSTADT

Fachbereich Physik
Institut für Kernphysik

Measurement of (n, γ)-Rates of Light Neutron-Rich Nuclei for the r-Process Nucleosynthesis
Messung von (n, γ)-Übergangsraten Leichter Neutronenreicher Kerne für die r-Prozeß Nukleosynthese

Genehmigte Dissertation von Dipl.-Phys. Marcel Heine aus Bad Muskau

1. Gutachten: Prof. Dr. Thomas Aumann
2. Gutachten: Prof Dr. Dr. h.c Norbert Pietralla

Tag der Einreichung: 27.05.2014
Tag der Prüfung: 09.07.2014

Darmstadt — D 17

Am Anfang gehts um explodierende Sterne.
Dann werden Formeln eingestreut.

Contents

List of Figures

List of Tables

Abstract

Exclusive neutron capture cross sections of ^{17}C and associated stellar reaction rates have been derived from Coulomb dissociation of ^{18}C using the R^{3}B-LAND setup at GSI in Darmstadt (Germany). The secondary beam of relativistic ^{18}C at approximately 430 AMeV was generated by fragmentation of primary ^{40}Ar on a beryllium target. In the FRagment Separator (FRS) the nuclei of interest were selected and subsequently guided to the experimental setup at Cave C. There the ions were excited electromagnetically in the electric field of lead target nuclei and the de-excitation process was detected with the R^{3}B-LAND setup. All reaction products of the one-neutron evaporation channel including gammas from de-exciting states of fragments were measured and the invariant mass was reconstructed. A similar measurement of ^{17}C Coulomb dissociation served as a benchmark to validate the accuracy of the present results with respect to previously published data.

The measured relative energy spectra of ^{18}C Coulomb dissociation to the ground state of ^{17}C as well as the first and second excited state in ^{17}C qualitatively match theoretical calculations of the Coulomb-dissociation process in an independent-particle model. In particular, the shapes of experimental data are reproduced. The measured spectroscopic factors were compared to an exclusive one-neutron knockout measurement on ^{18}C, which is consistent within the respective uncertainties.

The energy differential cross sections were converted into photo-absorption cross sections $^{18}\mathrm{C}(\gamma,n)^{17}\mathrm{C}$ with virtual-photon theory. Subsequently, exclusive neutron-capture cross sections $^{17}\mathrm{C}(n,\gamma)^{18}\mathrm{C}$ to the ground state were derived using the detailed-balance theorem. The neutron-capture cross sections were used to calculate stellar reaction rates, where the neutron velocities follow a Maxwell-Boltzmann distribution. The results were compared to thermonuclear reaction rates from a statistical Hauser-Feshbach model (HF). The uncertainty of the experimental results is at maximum around 60% at $T_9 = 1$ GK for neutron capture in the ground state of ^{17}C. This is accompanied by an uncertainty of a factor of ten in the HF calculation.

Zusammenfassung

Mit dem R^3B-LAND genannten experimentellen Aufbau an der GSI in Darmstadt wurden nach Coulomb Aufbruch vom ^{18}C exklusive Neutroneinfang-Wirkungsquerschnitte von ^{17}C ermittelt und daraus stellare Reaktionsraten berechnet. Der Sekundärstrahl mit relativistischen ^{18}C Ionen mit Energien von ungefähr 430 AMeV wurde durch Fragmentation von ^{40}Ar Primärstrahl in einem Beryllium Target erzeugt. Anschließend wurden die interessierenden Ionen im FRagment Separator (FRS) ausgewählt und zur Experimentierhalle Cave C geleitet. Dort wurden die ^{18}C Ionen im elektrischen Feld der Bleikerne des Sekundärtargets angeregt. Der anschließende Abregungsprozeß wurde mit dem R^3B-LAND Aufbau detektiert. Dabei wurden alle Reaktionsprodukte des ersten Neutronenseparationskanals, einschließlich Gammas aus Kernabregungen angeregter Fragmente, kinematisch bestimmt. Aus dieser Messung wurde die invariante Masse rekonstruiert. Im Vergleich einer Messung des Coulomb Aufbruch von ^{17}C mit einer früheren Veröffentlichung wurde die Genauigkeit der hier präsentierten Auswertung bestätigt.

Die Relativenergiespektren des (^{17}C-n) Systems bei ^{18}C Coulomb Aufbruch mit ^{17}C im Grundzustand, sowie dem ersten und zweiten angeregten Zustand wurden experimentell ermittelt. Diese Spektren können mit theoretischer Berechnungen des elektromagnetischen Aufbruchprozesses in einem Modell nicht-wechselwirkender Teilchen reproduziert werden, wobei insbesondere die Form des Spektrums eindeutig abgebildet wird. Die gemessenen spektroskopischen Faktoren stimmen mit denen aus einer Veröffentlichung zu nuklearen Aufbruch von ^{18}C überein.

Aus den energieabhängigen Wirkungsquerschnitttten wurden im Rahmen der Theorie virtueller Photonen Photoabsorptions-Wirkungsquerschnitte $^{18}\mathrm{C}(\gamma,n)^{17}\mathrm{C}$ berechnet. Daraus wurden im Reaktionsgleichgewicht exklusive Neutroneneinfangs-Wirkungsquerschnitte $^{17}\mathrm{C}(n,\gamma)^{18}\mathrm{C}$ in den Grundzustand von ^{18}C ermittelt. Diese wurden verwendet um stellare Reaktionsraten zu errechnen, wobei die Neutronengeschwindigkeiten mit einer Maxwell-Boltzmann Verteilung beschrieben wurden. Die Resultate wurden mit thermonuklearen Reaktionsaten aus der theoretischen Beschreibung des Neutroneneinfangprozesses in einem statistischen Hauser-Feshbach Modell (HF) verglichen. Die Messungenauigkeit der experimentellen Ergebnisse ist im schlechtesten Fall 60% bei $T_9 = 1$ GK. In der HF-Rechnung hingegen wird die Unsicherheit mit einen Faktor zehn beziffert.

1 Introduction

In the physicist's comprehension all elements were formed in the Big Bang and various synthesis processes along the lifetime of stars [1]. Such, the observed atomic abundance pattern of the solar system is understood qualitatively. The stellar nucleosynthesis model comprises sequences of stellar burning phases as well as explosive scenarios like the r-process. In these synthesis processes nuclear reactions are involved, which are investigated in nuclear physics experiments in the laboratory. This knowledge is indispensable to validate astrophysical models and to improve their accuracy.

In the r-process nucleosynthesis mechanism a series of neutron captures is interspersed with β-decays. It takes place on a timescale of a few seconds and is responsible for the production of half of the nuclei in the mass range $70 \leq A \leq 209$ and the actinides [2]. In an astrophysical site with sufficiently high neutron concentration neutron captures (n,γ) dominate over β-decays and neutron-rich matter is created. The reaction flow through light neutron-rich nuclei is sketched in figure 1.1 by red arrows. In this excerpt of the chart of nuclides stable nuclei are indicated by black boxes, while neutron-rich and neutron-deficient species are shown in blue and pink, respectively. The illustrated nucleosynthesis *via* a typical r-process path taken from Terasawa *et al.* [4] involves exotic neutron-rich nuclei and proceeds close to the neutron drip line. Depending on the temperature, photodisintegration (γ,n) counteracts radiative neutron captures and the matter configuration is defined. The neutron-rich matter 'freezes-out', when a cooling mechanism takes action. Subsequently, the nuclei β-decay towards the line of stability and form the observable abundance pattern.

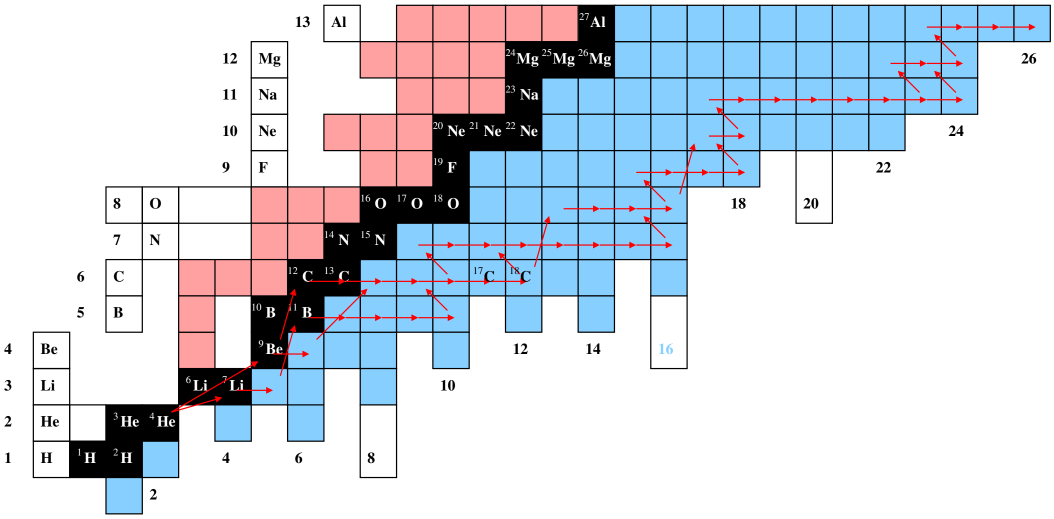

Figure 1.1.: Chart of the nuclides for light nuclei with $T_{1/2} > 10^{-6}$ s [3]. A typical r-process nucleosynthesis path from Terasawa *et al.* [4] is indicated by red arrows. The neutron shell closures of stable nuclei at $N = 8, 20$ are shown, as well as the proposed magic number for light neutron-rich nuclei at $N = 16$ [5].

In the shock front of a core-collapse supernova the neutrino wind heats up the collapsing matter, which gets decomposed into α-particles and neutrons and is accelerated outwards, where it cools down to the r-process temperature regime [6]. In this way, the reactions involving charged particles that lead to the seed nuclei die out comparably fast and the r-process neutron capture sequence proceeds on the seed nuclei.

A hydrodynamical study by Sumiyoshi *et al.* [7] established r-process nucleosynthesis assuming a $2.0\,M_\odot$ proto-neutron star of 10 km radius and with simplified treatment of the neutrino luminosities and spectra. This model was utilised by Terasawa *et al.* [4] for a study of the influence of the reaction network on the produced abundances in a supernova explosion. It was found that reactions of light neutron-rich nuclei severely affect the neutron-to-seed ratio, which has a crucial impact on the final abundance pattern. Particularly, neutron capture on ^{17}C,

$$^{17}\mathrm{C} + \mathrm{n} \rightarrow {}^{18}\mathrm{C} + \gamma, \tag{1.1}$$

was identified to be of high importance. The neutron separation energy of ^{18}C of 4.18 MeV [3] is high compared to its neighbours ^{17}C (0.73 MeV) and ^{19}C (0.53 MeV [8]), while the β-decay half-lives are similar. Due to this configuration, ^{18}C can be highly abundant in the r-process reaction path and its feeding from neutron capture and the β-decay put time constraints on the entire synthesis flow.

The sensitivity of the r-process nucleosynthesis to nuclear reaction rates of light elements was investigated by Sasaqui *et al.* [9]. Again, “semi-waiting points” among the carbon isotopes were identified. There, the stellar reaction rate for the neutron capture (1.1) was found to be uncertain by a factor of ten. Thus, their experimental determination was considered to strongly impact the comprehension of the r-process abundances.

Since ^{17}C is unstable, the neutron capture of interest cannot be measured directly but is accessible by the time-reversed process, *i.e.* the Coulomb dissociation of ^{18}C,

$$^{18}\mathrm{C} + \gamma^* \rightarrow {}^{17}\mathrm{C} + \mathrm{n}. \tag{1.2}$$

The excitation process is conducted by a virtual photon γ^* and takes place when medium- or high-energy projectiles cross the electromagnetic field of a high-charge target nucleus. The patterns of the subsequent de-excitation process also exhibit nuclear structure information of the projectile. In this way, halo nuclei were investigated by Nakamura *et al.* [8], and neutron skins of exotic nuclei were studied by Klimkiewicz *et al.* [10].

The focus of this work is set on the analysis of a Coulomb-dissociation experiment carried out in 2010 with the LAND-R^{3}B setup at GSI. The excitation of ^{18}C projectiles with energies of around 430 AMeV, directed on a lead target, was investigated. The theoretical principles required for the description of the excitation mechanism are depicted in Chapter 2 of this thesis. In the case of excitations beyond the particle-emission threshold, neutron-rich nuclei decay mostly by emission of neutrons. In the presented experiment, such neutrons were detected in coincidence with the ^{17}C fragments on an event-by-event basis. Additionally, gammas from the fragment’s de-excitation were measured. The experimental setup and the calibration of the detector systems are described in the Chapters 3 and 4. A detailed characterisation of the analysis concept, including the definition of the reaction channel, follows in Chapter 5. Finally, energy-differential exclusive cross sections and deduced thermonuclear reaction rates for neutron capture on ^{17}C are presented in Chapter 6. After the discussion, conclusions are drawn from the analysed experiment.

2 Experimental Technique

In the reaction flow of the r-process nucleosynthesis short-lived nuclei far away from the β-stability line are involved. Neutron capture reactions (n,γ) in this region cannot be studied directly in an experiment, but *via* the inverse process (γ,n) when the target and projectile role are exchanged.

The $^{14}\mathrm{C}(n,\gamma)^{15}\mathrm{C}$ reaction has been studied directly applying the activation technique [11] and in the inverse direction by means of electromagnetic dissociation [12], that is the excitation of a projectile-like target in relativistic electromagnetic fields. The neutron-capture cross sections deduced from the latter approach are in good agreement with directly measured ones [11]. Furthermore, they agree well with theoretical predictions of the reaction rate [13] based on measured spectroscopic factors from the $^{14}\mathrm{C}(d,p)^{15}\mathrm{C}$ neutron-stripping reaction. Therefore, Coulomb dissociation is an established tool to investigate neutron-capture rates of short-lived nuclei.

2.1 Reaction Mechanism in Relativistic Electromagnetic Collisions

The description of electromagnetic excitations in relativistic collisions induced by heavy ions is based on the equivalent photon method, which goes back to Fermi [14]. There it was used to explain absorption of optical light in mercury. In the non-relativistic approach the electric field of a moving charge passing a particle at rest was considered. By means of a Fourier transform its harmonic components were obtained and interpreted as a continuous distribution of equivalent photons struck from the moving particle. The equivalent photon method was developed further by Weizsäcker [15] and Williams independently by taking relativistic effects into account. Thereby, in the former publication for example electromagnetic radiation due to bremsstrahlung was described.

In figure 2.1, the electromagnetic excitation process at relativistic energies in inverse kinematics is sketched. The (red) projectile is moving towards the (blue) target nucleus and the distortion of the electric-field lines due to the relativistic energy of the projectile are also indicated. While in inverse

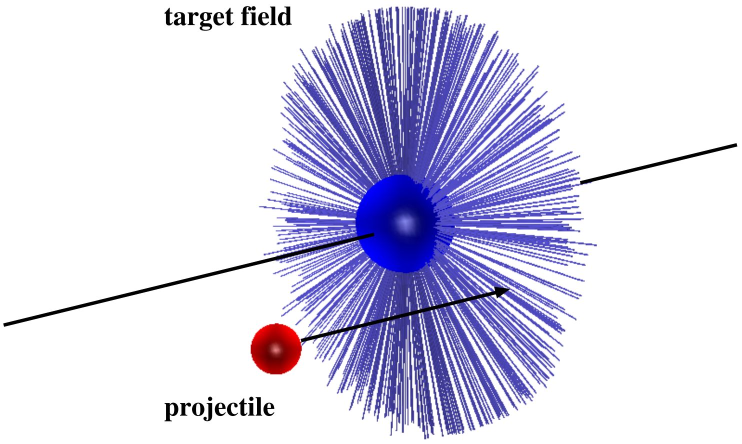

Figure 2.1.: A projectile (red) at relativistic energies incident on the target (blue). The distorted electric field of the target seen by the projectile is sketched.

kinematics the electric and magnetic fields parallel and perpendicular to the velocity of the projectile can be decomposed as [16]:

$$E_{\perp}(t) = \frac{Z_T e\gamma b}{(b^2+\gamma^2 v^2 t^2)^{3/2}}, \; B_{\perp}(t) = \beta E_{\perp}(t), \tag{2.1}$$

$$E_{\parallel}(t) = \frac{Z_T e\gamma v t}{(b^2+\gamma^2 v^2 t^2)^{3/2}}, \; B_{\parallel}(t) = 0, \tag{2.2}$$

where Z_T is the target charge number, e is the charge unit and γ is the relativistic Lorentz factor,

$$\gamma = \frac{1}{\sqrt{1-v/c}}. \tag{2.3}$$

The impact parameter b is the perpendicular distance between the projectile trajectory, which is approximated by a straight line, and the target nucleus. It can be calculated according to the parametrisation from Benesh *et al.* [17], based on experimental nucleon-nucleus and nucleon-nucleon reaction data at relativistic energies:

$$b_{min} = r_0(A_T^{1/3} + A_P^{1/3} - x(A_T^{-1/3} + A_P^{-1/3})). \tag{2.4}$$

Here, $A_T^{1/3}$ and $A_P^{1/3}$ are the mass numbers of the target and projectile, respectively. The parameters fitted to nuclear collision data and confined for Coulomb dissociation reactions are $r_0 = 1.34$ fm and $x = 0.75$, yielding $b = 10.9$ fm for ^{18}C impinging on a lead target. In figure 2.2, the components of the electric fields, equations (2.1) and (2.2), for a 426 AMeV ^{18}C beam on lead target are shown. As can be seen, the interaction time with the electromagnetic field is very short: $\Delta t \sim b/\gamma v \approx 10^{-23}$ s. Hence, the impact of

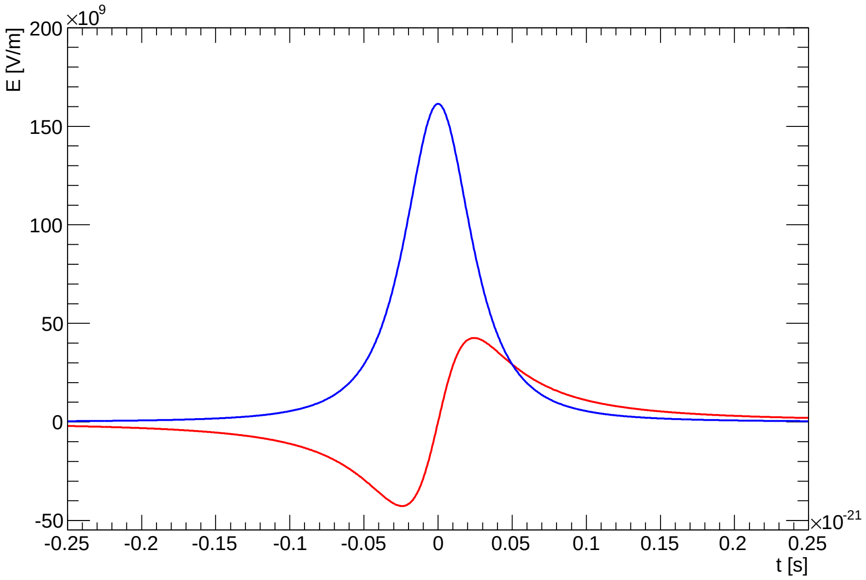

Figure 2.2.: Parallel (red line) and transverse (blue line) component of the electric field of the lead nucleus for 426 AMeV ^{18}C beam.

the transverse fields $E_\perp(t)$ and $B_\perp(t)$ can be interpreted as a pulse of plane-polarised radiation incident on the projectile.

The amount of energy incident per frequency interval can be expressed in classical electrodynamics as [16]:

$$\frac{\mathrm{d}I(\omega)}{\mathrm{d}\omega} = 2\pi \int_{b_{min}}^{\infty} \left(\frac{\mathrm{d}I_{\|}(\omega, b)}{\mathrm{d}\omega} + \frac{\mathrm{d}I_{\perp}(\omega, b)}{\mathrm{d}\omega} \right) b\, \mathrm{d}b, \tag{2.5}$$

where the minimum impact parameter b_{min} has to be chosen such, that beyond it the effect of the fields on the projectile equals an equivalent radiation pulse, according to the parameterisation of Benesh *et al.* [17]. The terms in the bracket denote the parallel and perpendicular frequency spectrum, obtained from a Fourier transform of the respective electric-field components. This introduces modified Bessel-functions $K_{0/1}(\xi_b)$ with the general $\xi_b = \omega b/\gamma v$ and the frequency spectra can be written like:

$$\frac{\mathrm{d}I_{\|}(\omega, b)}{\mathrm{d}\omega} = \frac{c}{2\pi} |E_\perp(\omega)|^2 = \frac{1}{\pi^2} \frac{Z_T^2 e^2}{c} \left(\frac{c}{v} \right)^2 \frac{1}{b^2} \xi_b^2 K_1^2(\xi_b), \tag{2.6}$$

$$\frac{\mathrm{d}I_{\perp}(\omega, b)}{\mathrm{d}\omega} = \frac{c}{2\pi} |E_\|(\omega)|^2 = \frac{1}{\pi^2} \frac{Z_T^2 e^2}{c} \left(\frac{c}{v} \right)^2 \frac{1}{b^2 \gamma^2} \xi_b^2 K_0^2(\xi_b). \tag{2.7}$$

In figure 2.3, the parallel and perpendicular frequency spectra for 426 AMeV ^{18}C beam, impinging on lead target, with $b_{min} = 10.9$ fm are shown. Since the frequency spectra decrease asymptotically, a maximum excitation energy cannot be extracted directly but is defined by the adiabacity parameter ξ_{adia}, which is the ratio of the collision time t_{coll} to the excitation time τ:

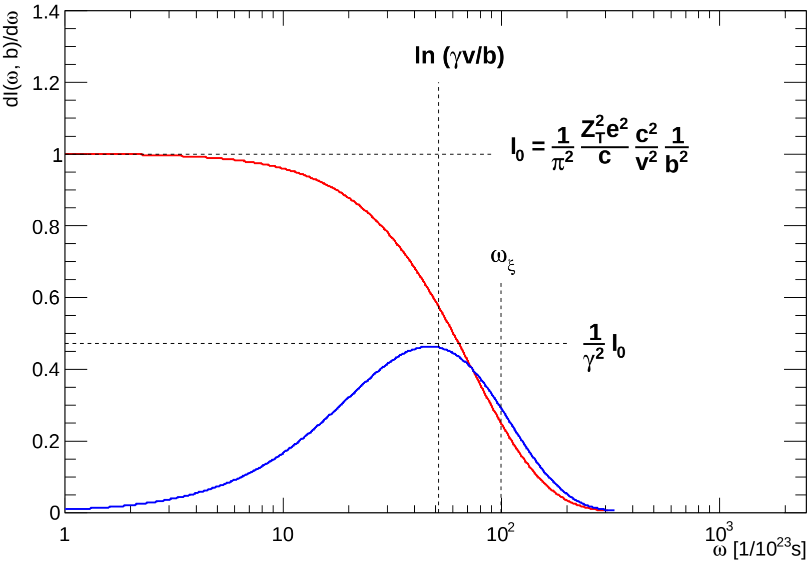

Figure 2.3.: Parallel (red) and perpendicular (blue) frequency spectrum $\frac{\mathrm{d}I(\omega,b)}{\mathrm{d}\omega}$ for 426 AMeV ^{18}C beam impinging on lead target. The adiabacity parameter in the frequency domain ω_ξ is also shown.

$$\xi_{adia} = \frac{t_{coll}}{\tau} = \frac{\epsilon b}{\hbar \gamma v}. \tag{2.8}$$

In formula (2.8), $\epsilon = \hbar\omega$ is the excitation energy. An excitation can just take place when ξ_{adia} is smaller than one. Otherwise the collision duration is too long and the interaction would be adiabatic. The frequency representation ω_ξ of the adiabacity parameter is also marked in the plot. The maximum excitation energy can be estimated from $\xi = 1$ and if $b = b_{min}$:

$$\epsilon_{max} = \frac{\hbar\gamma v}{b_{min}}. \tag{2.9}$$

For ^{18}C projectiles with $\beta = 0.727$ this yields $\epsilon_{max} = 19.2$ MeV.

Since its Fourier transformed harmonic components are interpreted as constituents of a virtual photon field, the electromagnetic field in the frequency interval $(\omega, \omega + \mathrm{d}\omega)$ can be expressed in terms of the number of virtual photons $N(\hbar\omega)$:

$$\frac{\mathrm{d}I(\omega)}{\mathrm{d}\omega}\mathrm{d}\omega = \hbar\omega N(\hbar\omega)\mathrm{d}\omega. \tag{2.10}$$

Given that the absorption of a virtual and a real photon are identical processes, the electromagnetic excitation (Coulomb excitation) cross section σ_C can be related to the photo-absorption cross section $\sigma_{\gamma n}$ like:

$$\sigma_C(\epsilon) = \int N(\epsilon)\sigma_{\gamma n}(\epsilon)\mathrm{d}\epsilon. \tag{2.11}$$

In the excitation process the multipolarity of the electromagnetic distribution of the projectile is changed, leaving it either in excited states or unbound states in the continuum beyond the particle emission threshold. These transitions are conducted by multipole transition operators, which couple the initial state configuration to the respective final state. Bertulani and Baur [18] deduced a representation of the total cross section σ_C with respect to the cross sections of single multipole modes $\sigma_{\gamma n}^{\pi\lambda}$ as:

$$\sigma_C(\epsilon) = \int \left(\sum_{\pi\lambda} \frac{1}{\epsilon} N_{\pi\lambda}(\epsilon)\sigma_{\gamma n}^{\pi\lambda}(\epsilon) \right) \mathrm{d}\epsilon. \tag{2.12}$$

Here, π and λ are the parity and angular momentum of the corresponding multipole operator. For the most prominent multipolarities the virtual photon numbers dispense with nuclear structure information and just expressing the electromagnetic reaction mechanism are:

$$N_{E1}(\epsilon) = \frac{2}{\pi} Z_T^2 e^2 \alpha \left(\frac{c}{v}\right)^2 \left(\xi K_0(\xi)K_1(\xi) - \frac{v^2\xi^2}{2c^2}\left(K_1^2(\xi) - K_0^2(\xi)\right) \right), \tag{2.13}$$

$$\begin{aligned} N_{E2}(\epsilon) = {} & \frac{2}{\pi} Z_T^2 e^4 \alpha \left(\frac{c}{v}\right)^4 \left(2\left(1 - \frac{v^2}{c^2}\right) K_1^2(\xi) + \xi \left(2 - \frac{v^2}{c^2}\right)^2 K_0(\xi)K_1(\xi) \right. \\ & \left. + \frac{v^4\xi^2}{2c^4}\left(K_0^2(\xi) - K_1^2(\xi)\right) \right), \end{aligned} \tag{2.14}$$

$$N_{M1}(\epsilon) = \frac{2}{\pi} Z_T^2 e^2 \alpha \left(\xi K_0(\xi)K_1(\xi) - \frac{\xi^2}{2}\left(K_1^2(\xi) - K_0^2(\xi)\right) \right), \tag{2.15}$$

where $\xi = \epsilon b/\hbar\gamma v$ is the adiabacity parameter. In figure 2.4, those virtual photon numbers for ^{18}C beam at 426 AMeV impinging on lead target are shown. The E2 contribution by far yields the highest photon numbers, while M1 excitations appear negligible. Note that the transition rate for a given nucleus strongly depends on the nuclear structure favoring certain multipole transitions. In principle, multiple multipole excitations can occur. However, it has been shown by means of experimental Coulomb excitation of the Giant Dipole Resonance that for excitation energies above 10 MeV this effect can be neglected [19] and the equivalent-photon theory [18] describes measured data correctly.

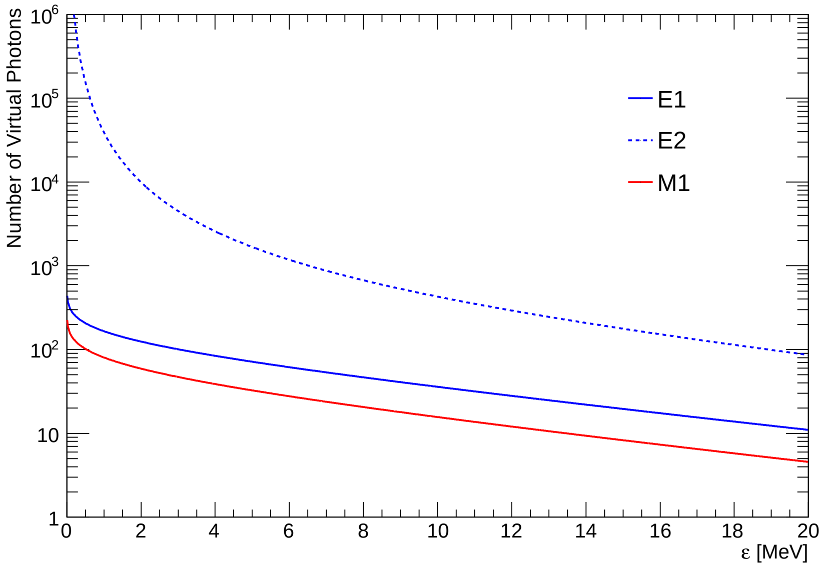

Figure 2.4.: Virtual photon numbers for ^{18}C beam at 426 AMeV impinging on lead target for the most prominent multipolarities.

2.2 Theoretical Calculation of Coulomb Dissociation Cross Sections

For the interpretation of experimental data the Coulomb-breakup cross sections were calculated from theory. In the calculations, which are depicted in the first section, basic nuclear structure features of the nuclei in the initial, final and scattering states are taken into account. Hence, when comparing to experimental data, nuclear structure information can be extracted. The relevant quantities, the experimental spectroscopic factor C^2S and the Asymptotic Normalisation Coefficient (ANC) are introduced in the last sections.

2.2.1 The CDXS+ Code

The calculations were performed with the FORTRAN program CDXS+ [20], which was run and maintained by S. Typel. The code was designed for breakup reactions of projectiles at intermediate and relativistic energies in heavy targets and provides various observables, that then can be compared to experimental data.

In the calculations at first the wave functions of the projectile and fragment, as well as scattering states in the continuum are defined. Therefor the projectile is decomposed into a system of the fragment and a valence neutron. A Woods-Saxon with radius $r = 1.25 \cdot A^{1/3}$ fm and diffuseness $a = 0.65$ fm serves as model potential for the description of the bound state. The single-particle energies of the neutrons in the Woods-Saxon were tuned for the reproduction of the experimental excited states and the separation energy of the projectile. As a consequence, in this simple model excited states and the Coulomb dissociation process are interpreted as single-particle transitions.

The transitions to the continuum states are conducted by multipole operators, that describe the change of the electromagnetic configuration of the system. The response of the electric multipole λ of the before mentioned fragment-neutron system is characterised by the effective charge [21]:

$$Z_{eff}^{(\lambda)} = Z_c \left(\frac{m_n}{m_c + m_n} \right)^{\lambda}, \tag{2.16}$$

where the indexed Z and m denote the charge and mass of the core c and valence neutron n, respectively. Higher multipolarities are strongly suppressed by $Z_{eff}^{(\lambda)}$, that becomes small due to the power of the mass ratio. Indeed, in the analysis presented here just the electric dipole transition $E1$ is important. It can be interpreted as a photon ($I^{\pi} = 1^{-}$) which conducts the bound states to the scattering states in the continuum. In this work, excitations of sd-shell neutrons from the $0d_{5/2}, 1s_{1/2}$ and $0d_{3/2}$ shells were taken into account (see figure 6.1). Due to positive parity of the sd-shell valence neutrons negative-parity continuum states are populated. They can also be accessed, when a negative-parity neutron is captured on the fragment. In this work, such neutrons from the $0p_{3/2}$, $0p_{1/2}$, $0f_{7/2}$ and $0f_{5/2}$ levels were considered. Excitations of protons were not taken into consideration.

The reduced matrix elements between the bound state and the scattering states were calculated from the Wigner-Eckert theorem. There, also higher electric multipole transitions and the magnetic dipole transition were taken into account. But in the calculations presented here, such transitions did not yield a significant contribution.

The calculations were made in so-called plane-wave and distorted-wave approximation. The approaches differ in the description of the potential of the scattering phase. For the latter approximation this potential was adapted to mime an additional interaction of the scattered particles–the so-called final interaction.

2.2.2 Experimental Spectroscopic Factors

According to Tostevin [22], the cross section $\sigma_{\text{th}}(I^{\pi})$ when populating the final state I^{π} of the fragment can be written as:

$$\sigma_{\text{th}}(\text{I}^{\pi}) = \sum_{j} C^2 S(I^{\pi}, nlj) \sigma_{\text{sp}}(S_n, nlj). \tag{2.17}$$

Therein, $\sigma_{\text{sp}}(S_n, nlj)$ denote the single particle cross sections, dependent on the neutron separation-energy S_n and the single particle quantum numbers (nlj). The spectroscopic factor $C^2 S$ reflects the weight of the according single particle cross section in the theoretical cross section and contains (model dependent) nuclear structure information.

The spectroscopic factors presented here were obtained experimentally by dividing the measured partial cross sections by the according theoretical single-particle cross sections: $C^2 S(I^{\pi}) = \sigma_{\text{exp}}/\sigma_{\text{sp}}$. In this way, shell model related information is bypassed and just single-particle properties of the excited nucleon are tested.

2.2.3 Asymptotic Normalisation Coefficients

Experimental spectroscopic factors reflect the integral of the valence-neutron wave function, because of normalisation. When using relative coordinates of the core-neutron system, just the radial part of the wave function is of interest due to rotational symmetry. The asymptotic behaviour of the radial wave function at large relative distances can be normalised to Whittaker functions by the Asymptotic Normalisation Coefficient. In this way, the dependence of the choice of the nuclear potential gets less important and the comparison of theoretical and experimental cross sections is solely related to the amplitude of the asymptotic radial wave function. In the Coulomb excitation the peripheral part of the radial wave function is tested [23] and the ANC provides a more unique measure on the spectroscopic information.

2.3 Neutron Capture Cross Sections

Photo-absorption cross sections $\sigma_{\gamma n}$ can be observed in the following reaction:

$$pr(\gamma,n)fr. \tag{2.18}$$

Here, *pr* and *fr* denote the projectile and fragment in the reaction. The neutron-capture cross sections $\sigma_{n\gamma}$ express the reaction probability of the time-reversed process:

$$fr(n,\gamma)pr. \tag{2.19}$$

In general, transitions from the initial state i to the final state f can be written in terms of the reaction cross section as [24]:

$$\mathrm{d}\sigma(i \to f) = \frac{2\pi}{\hbar}\frac{1}{v_i}\frac{1}{N_i}\sum_i\sum_j \left|T(i \to f)\right|^2 \delta(E_i - E_f), \tag{2.20}$$

where, besides the overall factor $2\pi/\hbar$, the second term is a flux factor related to the relative velocity of the interacting particles, and N_i is the number of initial states. The matrix elements T_{fi} are summed over all initial and final states and the δ-function assures energy conservation. Momentum conservation is fulfilled by the use of relative coordinates. Each particle can be characterised by its total angular momentum quantum number J with a $(2J+1)$-degeneracy M. When using relative coordinates and the Q-value for the reaction $A + a \to B + b$, follows:

$$\begin{aligned}\mathrm{d}\sigma(A + a \to B + b) = {} & \frac{2\pi}{\hbar}\frac{\mu_i}{p_i}\frac{1}{(2J_A+1)(2J_a+1)}\sum_{M_A M_a}\sum_{M_B M_b} \\ & \times \int \frac{\mathrm{d}^3 p_f}{(2\pi\hbar)^3}\left|T(J_A J_a \vec{p}_i \to J_B J_b \vec{p}_f)\right|^2 \delta(E_i - E_f - Q).\end{aligned} \tag{2.21}$$

Here, $\vec{p}_{i/f}$ denote the relative momenta of the states i/f and $\mu_i = m_A m_a/(m_A + m_a)$ is the reduced mass. Integrating along the momenta p_f yields:

$$\begin{aligned}\mathrm{d}\sigma(A + a \to B + b) = {} & \frac{2\pi}{\hbar}\frac{\mu_i}{p_i}\frac{1}{(2J_A+1)(2J_a+1)}\sum_{M_A M_a}\int\frac{\mathrm{d}\Omega_i}{4\pi} \\ & \times \sum_{M_B M_b}\int \mathrm{d}\Omega_f \frac{\mu_f p_f}{(2\pi\hbar)^3}\left|T(J_A J_a \vec{p}_i \to J_B J_b \vec{p}_f)\right|^2.\end{aligned} \tag{2.22}$$

Similarly, the cross section for the inverse reaction is:

$$\begin{aligned}\mathrm{d}\sigma(B + b \to A + a) = {} & \frac{2\pi}{\hbar}\frac{\mu_f}{p_f}\frac{1}{(2J_B+1)(2J_b+1)}\sum_{M_B M_b}\int\frac{\mathrm{d}\Omega_f}{4\pi} \\ & \times \sum_{M_A M_a}\int \mathrm{d}\Omega_i \frac{\mu_i p_i}{(2\pi\hbar)^3}\left|T(J_B J_b \vec{p}_f \to J_A J_a \vec{p}_i)\right|^2.\end{aligned} \tag{2.23}$$

Making use of,

$$\left|T(J_A J_a \vec{p}_i \to J_B J_b \vec{p}_f)\right|^2 = \left|T(J_B J_b \vec{p}_f \to J_A J_a \vec{p}_i)\right|^2, \tag{2.24}$$

leads to the detailed balance theorem for the total reaction cross sections:

$$\begin{aligned}(2J_A+1)(2J_a+1)p_i^2\cdot\sigma(A+a\rightarrow B+b)\\ =(2J_B+1)(2J_b+1)p_f^2\cdot\sigma(B+b\rightarrow A+a).\end{aligned} \tag{2.25}$$

Now the neutron-capture cross section for reaction (2.19) can be expressed in terms of the photo-absorption cross section (2.18) as:

$$\sigma_{n\gamma}^{\pi\lambda}(E_{rel})=\frac{2(2J_{pr}+1)}{(2J_{fr}+1)(2J_n+1)}\frac{p_\gamma^2}{p_f^2}\cdot\sigma_{\gamma n}^{\pi\lambda}(\epsilon), \tag{2.26}$$

depending on the relative energy E_{rel} of the fragment and neutron and taking also into account the multipolarity of the Coulomb excitation. The photon degeneracy is two. With $p_\gamma=\epsilon/c$, $p_f=2\mu E_{rel}$ and $\mu=m_{fr}m_n/(m_{fr}+m_n)$ at non-relativistic energies in the centre of mass system, the neutron-capture cross section can be calculated according to:

$$\sigma_{n\gamma}^{\pi\lambda}(E_{rel})=\frac{2(2J_{pr}+1)}{(2J_{fr}+1)(2J_n+1)}\frac{\epsilon^2}{c^2\cdot 2\mu E_{rel}}\cdot\sigma_{\gamma n}^{\pi\lambda}(\epsilon). \tag{2.27}$$

2.3.1 Reaction Rates

In the frame of this work the neutron-capture cross sections from equation (2.27) were obtained from Coulomb dissociation at laboratory conditions. They are adapted to the thermal neutron distribution of the according astrophysical site by the neutron capture rate:

$$\lambda\equiv N_{\mathrm{Av}}\langle\sigma v\rangle, \tag{2.28}$$

where N_{Av} is the Avogadro constant and v the neutron velocity. The expectation value can be written as:

$$\langle\sigma v\rangle=\int_0^\infty \mathrm{d}v\,\sigma(v)v\,\Phi(v), \tag{2.29}$$

and is determined by integration over the velocity distribution $\Phi(v)$. When the neutrons are considered a non-relativistic ideal gas in thermal equilibrium, the velocity distribution is the Maxwell-Boltzmann function:

$$\Phi(v)=4\pi\left(\frac{m}{2\pi k_{\mathrm{B}}T}\right)^{\frac{3}{2}}\cdot v^2\mathrm{e}^{-\frac{mv^2}{2k_{\mathrm{B}}T}}. \tag{2.30}$$

Here, m is the neutron mass, T the temperature and k_{B} the Boltzmann constant. The first term assures normalisation $\int\Phi(v)\mathrm{d}v=1$. From the substitution $v=\sqrt{2E/m}$ the energy dependent neutron distribution is derived:

$$\Phi(E)=\sqrt{\frac{8m}{\pi(k_{\mathrm{B}}T)^3}}\cdot E\,\mathrm{e}^{-\frac{E}{k_{\mathrm{B}}T}}. \tag{2.31}$$

Note that $\Phi(E)$ is not normalised. When the differential $\mathrm{d}v = \mathrm{d}E/\sqrt{2mE}$ is replaced in (2.29), the reaction rate at temperature T can be expressed as:

$$\lambda = N_\mathrm{A} \int_0^\infty \mathrm{d}E \sqrt{\frac{8}{\pi m (k_\mathrm{B} T)^3}} \cdot \sigma(E)\, E\, \mathrm{e}^{-\frac{E}{k_\mathrm{B} T}}. \tag{2.32}$$

In this work, temperature dependent thermonuclear reaction rates in $\mathrm{cm}^3/(\mathrm{mol}\cdot\mathrm{s})$ were calculated from equation (2.32) by integration of the cross sections (2.27) over the relative energy.

In an astrophysical plasma of temperature T the target states μ are thermally populated and the astrophysical cross section σ^* is given by [25]:

$$\sigma^*(E_{rel}) = \frac{\sum_\mu (2J_\mu + 1) \exp(-E_\mu^*/k_\mathrm{B} T) \cdot \sigma_\mu^{tot}(E_{rel})}{\sum_\mu (2J_\mu + 1) \exp(-E_\mu^*/k_\mathrm{B} T)}, \tag{2.33}$$

where the J_μ and E_μ^* are the spins and level energies, respectively, of the target states. The $\sigma_\mu^{tot}(E_{rel})$ denote the neutron capture cross sections from distinguished target states to all states of the final nucleus. These cross sections are weighted according to the thermal population of the initial states μ by the partition function. The spin terms assure that the detailed balance theorem is fulfilled for the calculation of photo-absorption cross sections from equation (2.33). Note that transitions to the ground state in $\sigma_\mu^{tot}(E_{rel})$ can be obtained from the measurement of the Coulomb dissociation of the final nucleus, while transitions to excited states have to be derived from theoretical calculations. Inserting equation (2.33) into (2.28) yields the stellar neutron capture rate:

$$\langle \sigma v \rangle^* = \langle \sigma^* v \rangle, \tag{2.34}$$

in $\mathrm{cm}^3/(\mathrm{mol}\cdot\mathrm{s})$ after multiplication with N_Av. Accordingly to expression (2.32) the stellar reaction rate can be calculated from:

$$N_\mathrm{Av} \langle \sigma v \rangle^* = N_\mathrm{A} \sqrt{\frac{8}{\pi m (k_\mathrm{B} T)^3}} \int_0^\infty \mathrm{d}E \frac{\sum_\mu (2J_\mu + 1) \exp(-E_\mu^*/k_\mathrm{B} T) \cdot \sigma_\mu^{tot}(E_{rel})}{\sum_\mu (2J_\mu + 1) \exp(-E_\mu^*/k_\mathrm{B} T)} \cdot E\, \mathrm{e}^{-\frac{E}{k_\mathrm{B} T}}, \tag{2.35}$$

integrating over the neutron energy E. In the frame of this work the stellar reaction rate was dominated by transitions from the ground state of $^{17}\mathrm{C}$ up to temperatures $T_9 \approx 5$ GK due to low level energies of the excited states of the target nucleus.

3 Experimental Setup

The Coulomb-dissociation experiment was part of an experimental campaign including almost all light exotic nuclei from the proton to the neutron drip line up to the neon isotopes. Such nuclei were provided by the GSI accelerator system and the FRagment Separator (FRS), which will be introduced briefly in the beginning. A detailed view on the experimental setup at the so-called Cave C follows, including the overall concept and the description of relevant detectors as well as the data acquisition.

3.1 GSI Accelerator Facility

In figure 3.1, the GSI facility is sketched and the relevant parts are labelled. The primary ^{40}Ar ion beam was generated by the ion source at the beginning of the UNIversal Linear ACcelerator (UNILAC). It accelerated the $^{40}\mathrm{Ar}^{11+}$ ions up to 11.5 AMeV before being injected into the SchwerIonenSynchrotron 18 (SIS18), which accelerated the ions up to 490 AMeV [27]. Subsequently to the ejection out of the SIS the ions have been directed onto the 4.01 g/cm^2 Be fragmentation target at the entrance of the FRS. A multitude of secondary nuclei entirely stripped off electrons and covering the proton- as well as the neutron-rich mass extreme was produced in the occurring fragmentation reactions. Due to comparably low rates expected for nuclei at the neutron drip-line a short spill length (0.5 s) acquired in fast ramping mode of the SIS18 magnets at a duty cycle of 0.4 Hz [27] was chosen.

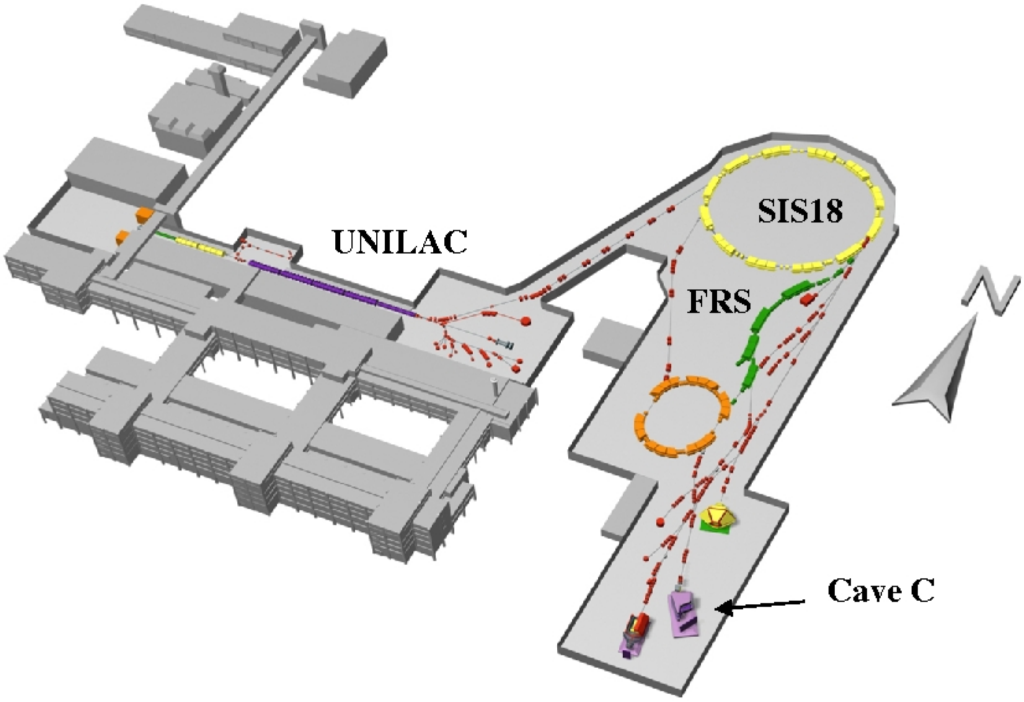

Figure 3.1.: GSI accelerator facility [26], comprising the UNILAC (purple), SIS18 (yellow), FRS (green) and the experimental hall Cave C.

The trajectory of a charged particle through a magnetic field is defined by:

$$B\rho = \frac{p}{Q} \propto \frac{A}{Z}\beta\gamma, \tag{3.1}$$

where B denotes the magnetic field, ρ the curvature of the trajectory, p the momentum and Q the charge of the particle. A and Z are the mass and charge number, respectively, β is the relativistic ion velocity and γ the associated Lorentz factor. The velocity is given by the energy of the primary beam and the geometry of the magnet puts limitations on the actual curvature ρ. Hence, the B-field must be tuned in order to select (fully ionised) species A/Z. Here, neutron-rich carbon isotopes with $A/Z \approx 3$ are of interest. Because of the FRS momentum acceptance of $\Delta p/p = 2\%$ [28], the secondary beam contained multiple ion species in addition to those with the adjusted A/Z value.

In figure 3.2, the FRS areas and dipole magnets (green) as well as quadrupole and sextupole magnets (yellow) are sketched. The fragmentation target is located at the so-called target area on the left side. In the $B\rho - \Delta E - B\rho$ method [28] the first dipole couple performs the A/Z selection and the beam is transversely spread in the S2 dispersive area according to the A/Z ratio of the ions. At S1 where the spatial beam profile is broadest slites may be inserted in order to reject the most extreme A/Z species. For the ions investigated here this was not necessary. The FRS is equipped with detectors for beam diagnostics. In particular, a 3 mm thick scintillator paddle was situated at S2 and position and time measurements have been performed. Due to high rates pile-up occurred and this data were not used in this analysis. It will be shown later that the separation of the incoming ions with respect to each other was still sufficient. Additionally, a degrader wedge can be inserted at S2 and ions cross material thicknesses dependent on the transverse position at S2. In this way, the beam can be purified, since unwanted nuclei will be bent off the beam line in the subsequent dipoles. No wedge was necessary, because the present experiment aimed for the investigation of a broad distribution of different ion species.

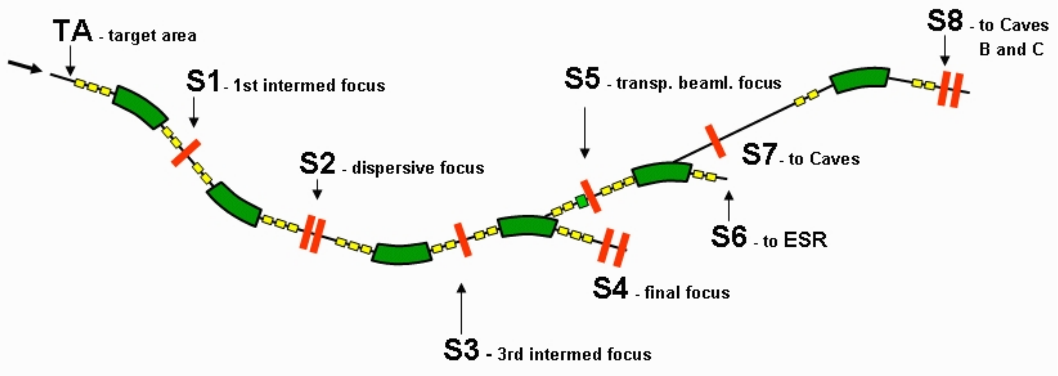

Figure 3.2.: FRS areas: Along the beam line the dipole magnets (green), quadrupole and sextupole magnets (yellow) are sketched [29].

In table 3.1, experimental rates per spill R and absolute numbers of ions I arriving at Cave C are summarised and compared to estimations from the proposal of the experiment [30]. Note that experimental rates were obtained from run 472 right after the setting of the magnets in the FRS was adjusted and data were extrapolated to the entire beam time. In the proposal a spill length of 1 s with a repetition cycle of 3 s was assumed. The initial ^{40}Ar intensity was taken to be 10^{10} ions/spill and compares to $6 \cdot 10^{10}$ ions/spill in the experiment. The fraction of requested and obtained ion intensity is given in the last column. Especially, light species were underproduced. Due to issues concerning the operation of the accelerator facility beam time was shortened significantly, but actually compensated by higher ^{40}Ar intensity. Hence these ratios represent a compromise.

The last FRS stage, *i.e.* the second dipole pair, compensates the dispersion at S2 focusing the beam to the achromatic focal plane S8, where position and time measurements were made with a 3 mm thick plastic scintillator paddle. Subsequently the nuclei were transported to the experimental hall by the ion optical system.

Ion	R [/Spill]		I		I_{exp}/I_{prop}
	Exp.	Prop.	Exp.	Prop.	
^{11}Be	4.6	636	$7.4 \cdot 10^5$	$1.7 \cdot 10^8$	$4 \cdot 10^{-3}$
^{12}Be	21	616	$3.3 \cdot 10^6$	$1.7 \cdot 10^8$	$2 \cdot 10^{-2}$
^{13}B	0.1	–	$1.6 \cdot 10^4$		
^{14}B	6.6	246	$1.1 \cdot 10^6$	$6.6 \cdot 10^7$	$2 \cdot 10^{-2}$
^{15}B	24	146	$3.9 \cdot 10^6$	$3.9 \cdot 10^7$	0.1
^{16}C	0.4	–	$6.8 \cdot 10^4$		
^{17}C	20	60	$3.3 \cdot 10^6$	$1.6 \cdot 10^7$	0.20
^{18}C	42	29	$6.6 \cdot 10^6$	$7.8 \cdot 10^6$	0.85
^{19}C	0.8	–	$1.3 \cdot 10^5$		
^{19}N	2.0	–	$3.2 \cdot 10^5$		
^{20}N	41	–	$6.5 \cdot 10^6$		
^{21}N	31	–	$5.0 \cdot 10^6$		
^{22}N	0.7	–	$1.1 \cdot 10^5$		
^{22}O	1.1	$3.0 \cdot 10^{-3}$	$1.6 \cdot 10^5$	806	208.6
^{23}O	6.3	3.4	$1.0 \cdot 10^6$	$9.1 \cdot 10^5$	1.1
^{24}O	2.4	1.2	$3.8 \cdot 10^6$	$3.2 \cdot 10^6$	1.2
^{25}F	0.2	0.01	$2.9 \cdot 10^4$	$2.6 \cdot 10^3$	11
^{26}F	3.3	0.9	$5.2 \cdot 10^5$	$2.4 \cdot 10^5$	2.2
^{27}F	1.2	0.3	$1.9 \cdot 10^5$	$8.1 \cdot 10^4$	2.4
^{28}Ne	0.03	–	$5.3 \cdot 10^3$		
^{29}Ne	0.5	0.3	$7.4 \cdot 10^4$	$8.1 \cdot 10^4$	0.9
^{30}Ne	0.2	–	$3.2 \cdot 10^4$		

Table 3.1.: Experimental rates per spill R and absolute numbers of ions I arriving at the experimental hall compared to numbers from the proposal [30] of the experiment.

3.2 R^3B-LAND Setup in Cave C

In the description of the Coulomb dissociation reaction-mechanism virtual photons that conduct transitions to continuum states are involved. Hence, for investigation kinematically complete measurements have to be performed. Therefor the projectile, fragment and neutrons were kinematically determined fully on an event-by-event basis, utilising the R^3B-LAND setup at Cave C. It can detect reaction products with velocities similar to the beam velocity [31] and light particles. Due to relativistic beam momenta the reaction products are strongly forward boosted and full acceptance measurements can be made with moderately sized detectors. Fragments are bent to the so-called fragment branch by A Large Acceptance Dipole Magnet (ALADiN) for particle identification.

The experimental setup suits multi-purpose, while this work concentrates on the investigation of electromagnetically induced reactions. The detection equipment comprises detectors of a few hundred micrometres thickness as well as those with volumes of several cubic metres. In figure 3.3, the relevant part of the detection system for the measurement of Coulomb dissociation is sketched. A more detailed description of the single detectors follows in the next section. Projectiles were tracked *via* Time-of-Flight (ToF) and energy loss (ΔE) measurements. While the former was performed between the FRS detector S8 and the POSition sensitive scintillator (POS), the Position sensitive Silicon PIN diode (PSP) was utilised for the latter. The Rechts-Oben-Links-Unten (ROLU) vetoed particles far off the optical axis. Two pairs of Double Sided Silicon Strip Detectors (DSSSD) directly in front and behind the target were used for the measurement of the scattering angle of the beam. The target chamber was entirely surrounded by the crystal-ball detector (XB), which is cut in the picture for illustration purpose, for the detection of prompt gammas. The beam line was evacuated up to ALADiN. In its magnetic field projectile-like fragments (red) were bent by around 15°. Along the fragment branch, position measurements for tracking purpose were carried out with two Großer FIber (GFI) detectors and the Time-of-Flight Wall (TFW). The latter additionally yielded ToF and ΔE measurements of fragments and unaffected beam particles. Neutrons (green) cross the magnetic field in a straight line and were determined in terms of time, position and energy-loss measurements in the Large Area Neutron Detector (LAND). In the right-handed coordinate system (x, y, z) z directs in beam direction, y points up and x to the right.

3.2.1 Detection Principles

When crossing the detector particles characteristically interact with the detector material. Therein, typical patterns and amounts of secondary particles are created, which are used to identify the initially incident particle. The energy loss per penetration depth x of heavy ions of charge Z due to excitation and ionisation of the atoms and molecules is described by the Bethe-Bloch formula [33]:

$$-\frac{\mathrm{d}E}{\mathrm{d}x} = \frac{4\pi Z^2 e^4}{m_e c^2 \beta^2} N z \left[\ln \frac{2 m_e c^2 \beta^2}{I} - \ln(1-\beta^2) - \beta^2 \right], \tag{3.2}$$

where e and m_e are the electron charge and mass, respectively, β is the ion velocity, N and z are the number density and atomic number of the crossed material. The mean ionisation potential of the absorber material is I. Without material constants (3.2) writes as:

$$-\frac{\mathrm{d}E}{\mathrm{d}x} \propto F(\beta) Z^2, \tag{3.3}$$

and the charge of the particle is accessible by an energy-loss measurement when its velocity is known. For the detection of charged particles scintillator and semiconductor detectors were used, which will be depicted in the following.

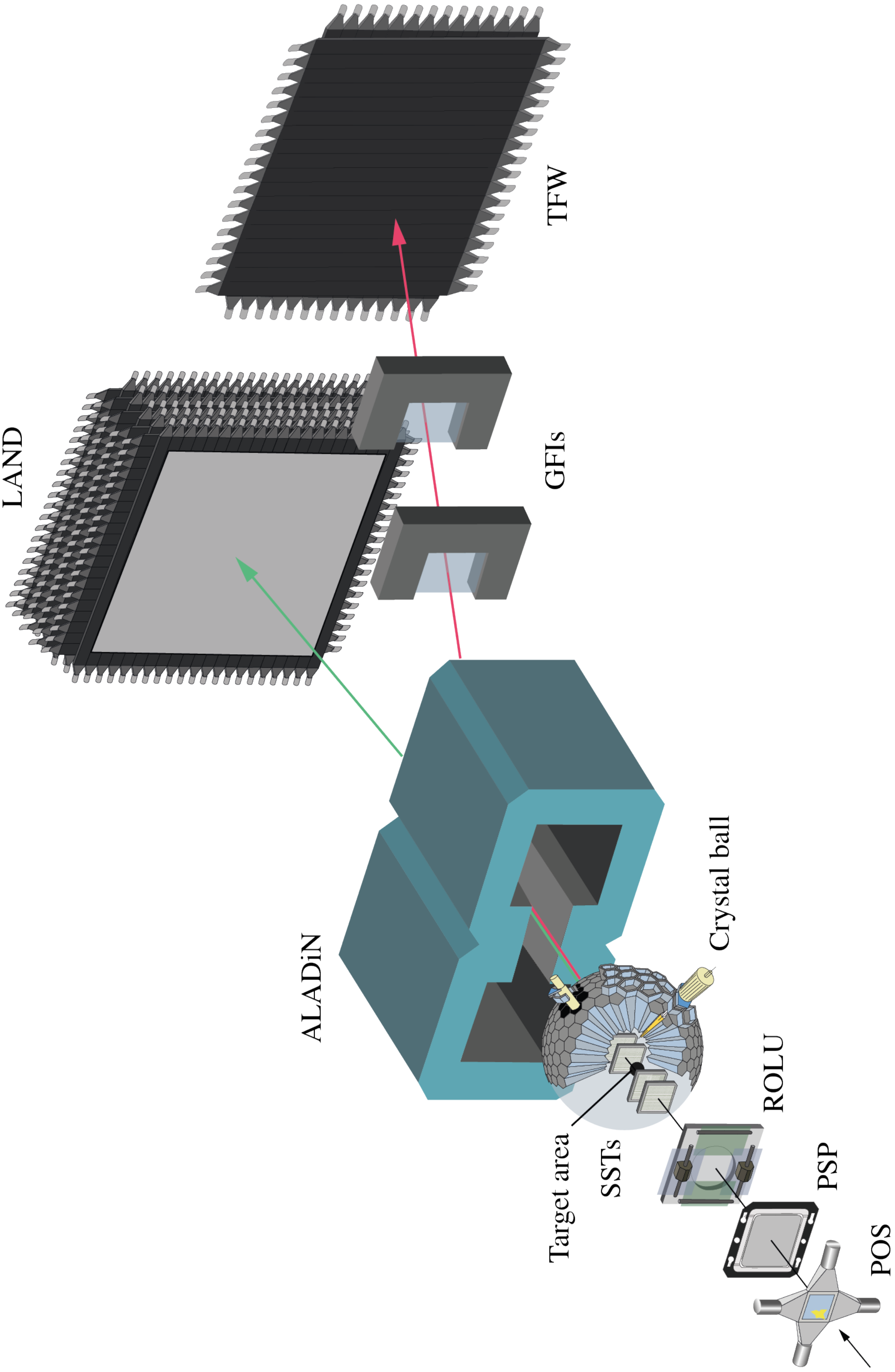

Figure 3.3.: R^3B-LAND setup at Cave C for the investigation of Coulomb dissociation. The detector description is in the text. Projectile tracks from the left as well as neutron (green) and fragment trajectories (red) are indicated. The picture was taken from [32].

Scintillation Detectors

As a charged particle passes through the scintillator it excites and ionises the atoms and molecules of the material. In the subsequent de-excitation process visible light is emitted, which is converted into a voltage *via* PhotoMultiplier Tubes (PMT). The scintillator response can be decomposed into two exponential referred as fast and slow component. The time integral is related to the deposit energy. In case of plastic detectors, the excitation process is of molecular kind resulting in de-excitation times of 2-3 ns and recommending them for timing issues. Here, plastic scintillators usually were used as paddles, which were connected to PMTs on both sides. The FRS and projectile timing detectors were composed of BC-420, and the bigger scintillators in Cave C were made of BC-408. The former plastic matter has a time-constant of 1.5 ns and allows for fast timing, while the latter is a general-purpose material*.

The time resolution Δt of scintillation detectors with horizontally- and vertically-crossed paddles is accessible by the difference:

$$t_{diff} = t_{hori} - t_{vert}, \tag{3.4}$$

where *e.g.* t_{hori} was obtained from the horizontal paddle. Error propagation yields:

$$\Delta t_{diff} = \sqrt{(\Delta t_{hori})^2 + (\Delta t_{vert})^2}. \tag{3.5}$$

Assuming similar uncertainties Δt in the crossed paddles for the time resolution follows:

$$\Delta t_{diff} = \sqrt{2}\Delta t. \tag{3.6}$$

In contrast, the excitation process of inorganic crystals like NaI (XB) takes place in an electron-band structure. Since inter-band states are involved in the de-excitation mechanism, typical decay times are in the order of 500 ns. On the other hand, the stopping power equation (3.2), is higher due to higher density and the material is suited for calorimetric measurements.

Semiconductor Detectors

In n-p junction a region with intrinsic space-charge (depletion zone) is created in semiconductors, since electrons and holes move along the electron-band structure leaving positive or negative charged dopants. Those form a potential and if ionising radiation liberates electron-hole pairs in the depletion zone, they are collected by the intrinsic electric field. According to the type of charge carriers, the n- and p-side electrodes are called cathode and anode, respectively. The charge collection efficiency and width of the depletion zone are enhanced when operating in reversed-bias junction, *i.e.* negative voltage to the p-side, since the corresponding charge carriers are pulled to the respective electrodes.

In Positive-Intrinsic-Negative (PIN) diodes high-resistivity material is inserted between the doped layers. They are operated reversed-bias in order to widen the active volume and reduce leakage current. In the PSP the intrinsic layer is made of 300 μm n-type high-resistivity silicon. On the p-side, connected to the anodes, boron ions are implemented [34] and a positive potential of a few hundred Volts was applied on the cathode. Because of the big active window, comparably high stopping power and enhanced charge-collection efficiency, the charge of crossing ionising radiation is obtained with comparably high resolution and the PSP was utilised for the identification of the projectile charge based on equation (3.3).

The semiconductor base of micro-strip detectors is similar to PIN diodes. In contrast, the electrode strips are connected to the substrate and each strip acts as a separate detector. The implantation pitch of the 300 μm thick DSSSD on the p-side is 27.5 μm, and on the n-side 104 μm. Indeed, position resolutions of around 15 μm were obtained (see section 5.6.3) and the detectors were used to obtain the scattering angle of the beam in the target.

---

[*] SAINT-GOBAIN product catalogue

3.2.2 Projectile Identification and Target Area

The projectile velocity was obtained from a long distance (≈ 56 m)[†] ToF measurement carried out between the plastic scintillators S8 and POS. The former was 22 × 10 × 0.3 cm^3 sized in width×height×thickness and located at F8 in the FRS. The time resolution cannot be derived from equation (3.6), since no vertical paddle is available. Therefore, it was extracted from run 408 where the beam x-position was limited by the ROLU detector to a spot size of 2 mm at the target area. The incoming particles can be tracked back on S8 due to ion optics, that just transports beam, and a limit on the time resolution $\sigma_t \leq 146$ ps of S8 was obtained.

The POS was a 5.5×5.5×0.1 cm^3 sized plastic detector located at the entrance of the experimental hall serving as reference detector. It was read out by one PMT per side quasi representing crossed paddles. From equation (3.6) a time resolution $\sigma_t = 70$ ps was calculated.

In front of the target the PSP[‡] was located. The cathode signal was utilised for energy-loss measurements and projectile charge Z identification according to the Bethe-Bloch formula (3.3). The relative charge resolution for light nuclei up to oxygen was $\sigma_Z/Z = 3\%$ yielding unambiguous charge assignment.

The target was sandwiched by two pairs of 7.2×4.1×0.3 cm^3 sized DSSSDs [35] for the measurement of the scattering angle of beam particles. Therefor x- and y-positions from the p- and n-side, respectively, of the detectors were used. As described in section 5.6.3, an intrinsic position resolution of $\sigma_{x/y} \approx 15\,\mu$m was obtained. The spacing of the detector pairs was 3 cm and the intrinsic angular resolution of $\sigma_\theta =$ 0.5 mrad was calculated for particle tracks around the target.

The target chamber was entirely surrounded by XB [36] consisting of 162 NaI crystals for the detection of prompt gammas. The detectors form conical prisms of 20 cm length which are housed in 600 μm thick aluminium shells. In table 5.1, a list of inactive or rejected crystals in this experiment is given. From a sequence of calibration runs with ^{22}Na and ^{60}Co sources, average relative energy resolutions of $(\Delta E/E)_{FWHM} = 12.2\%$ at 511 keV and $(\Delta E/E)_{FWHM} = 7.5\%$ at 1333 keV have been extracted. XB has not been used for timing.

3.2.3 Fragment Branch

Projectile-like particles are bent by around 15° to the fragment arm when they cross the magnetic field of ALADiN. A recent measurement yielded a maximum field $B_{max} = 1.7$ T at maximum solenoid current. The $\vec{B}$-field chamber is conical-like shaped and was filled with helium in the experiment presented here. For high acceptance detection of the reaction products [31] its opening windows on the front and rear side are sized 50×129 cm^2 and 60×198 cm^2, respectively, in width×height. Note that the acceptance on the front side was actually limited by the flange that connects the magnet to the beam line.

All detectors behind the magnet were operated in air. By means of the GFIs [37] x-position measurements were made. These detectors are composed of 475 vertically placed fibers with a square cross section of 1×1 mm^2 and cover an area of 50×50 cm^2. The fibers are fit to a Position-Sensitive Photo-Multiplier (PSPM) by a mechanical mask. From the centroid of the measured charge distribution on the PSPM the x-position is obtained. For carbon a position resolution $\Delta x_{FWHM} = 0.7 \pm 0.1$ mm was extracted [38]. Since two detectors were present, the position right behind ALADiN and the deflection angle from the magnetic field were derived.

For the fragment-charge determination timing and position measurements the TFW were utilised. The detector consists of 14×18 plastic scintillator paddles in horizontally- and vertically-crossed planes, respectively. The former paddles have dimensions of 197×10×0.5 cm^3 and the latter of 155×10×0.5 cm^3. The relative charge resolution for carbon $\sigma_Z/Z = 4\%$ yielded unambiguous fragment identification. The time resolution calculated from equation (3.6) was $\sigma_t = 156$ ps.

[†] see equation (4.3)

[‡] HAMAMATSU PSD S5378-02

Plane	1	2	6	7	9	10
Paddle	1, 20	19	6, 13	17	1, 12, 20	all

Table 3.2.: List of inactive paddles in LAND.

3.2.4 Neutron Detection

LAND was used for ToF and position measurements for the neutrons. The detector is composed of 10 layers of 20 so-called paddles. Each paddle is 10 cm thick and consists of ten $200\times10\times0.5$ cm^3 plastic scintillators, that are sandwiched with ten 0.5 cm thick iron sheets. The layers are arranged in crossed pattern and form a total detector volume of $2\times2\times1$ m^3 [39]. The iron sheets serve as passive converters in which charged particles are created in nuclear reactions with the incident neutrons. Subsequently, the secondaries deposit energy in the plastic detectors, which finally was detected. LAND was located around 12 m from the target in the direction of the incoming beam limiting the neutron angular acceptance to $a_n = \pm 80$ mrad.

In table 3.2, a list of inactive paddles in this experiment effecting the detector performance is given. The time resolution was obtained from gammas emitted in nuclear reactions in the target. They travel with velocity c and the width of the γ-peak in the velocity spectrum of LAND at a certain depth z defines the ToF uncertainty. From $t_n = s_n / v_n$ follows the ToF uncertainty using propagation of error:

$$\Delta t_n = \sqrt{\left(\frac{\Delta s_n}{c}\right)^2 + \left(\frac{s_n \cdot \Delta v_n}{c^2}\right)^2}. \tag{3.7}$$

The paddle width defines $\Delta s_n = 10$ cm resulting in $\Delta t_{FWHM} < 827$ ps or $\sigma_t < 350$ ps. Note that the value derived serves as an upper limit, since neutrons induce more light than gammas in the plastic scintillators.

3.2.5 Data Acquisition

The energy deposit in interactions of the nuclei with the detector material was converted into an voltage by the enclosed readout electronics. Subsequently, if exceeding an initial threshold and producing a trigger signal, it was converted into a logic signal and handed to the TRigger LOgic (TRLO). There, from the information of the single detectors the relevance of each event was reconstructed by means of a so-called trigger matrix. Such, it was classified into potential reactions and background events at first glance. Since not all detected events can be handled by the Data AcQuisition system (DAQ), the trigger rates were scaled down according to their priority (background less important). A trigger-decision signal was provided by the TRLO and eventually reduced event rates were finally stored by the DAQ on disk. In figure 3.4, the signal flow is illustrated and in the following the highlighted phrases will be explained in more detail.

Trigger Logics

Each detector which provided a time was also used to distribute a trigger signal, that is a logic signal related to the initial timing information. The trigger usually was generated by a GSI brand Constant Fraction Discriminator (CFD) of the CF 8000 [26] series. There, in order to suppress noise from electronics, input analog signals below a threshold are disregarded. The CFD is supposed to provide a constant time relation of the analog peak position and the logic output signal for similarly shaped signals.

Regarding compound detectors the final trigger was generated from several channels according to the requested multiplicity, *i.e.* the minimum number of channels with individual triggers. As an example,

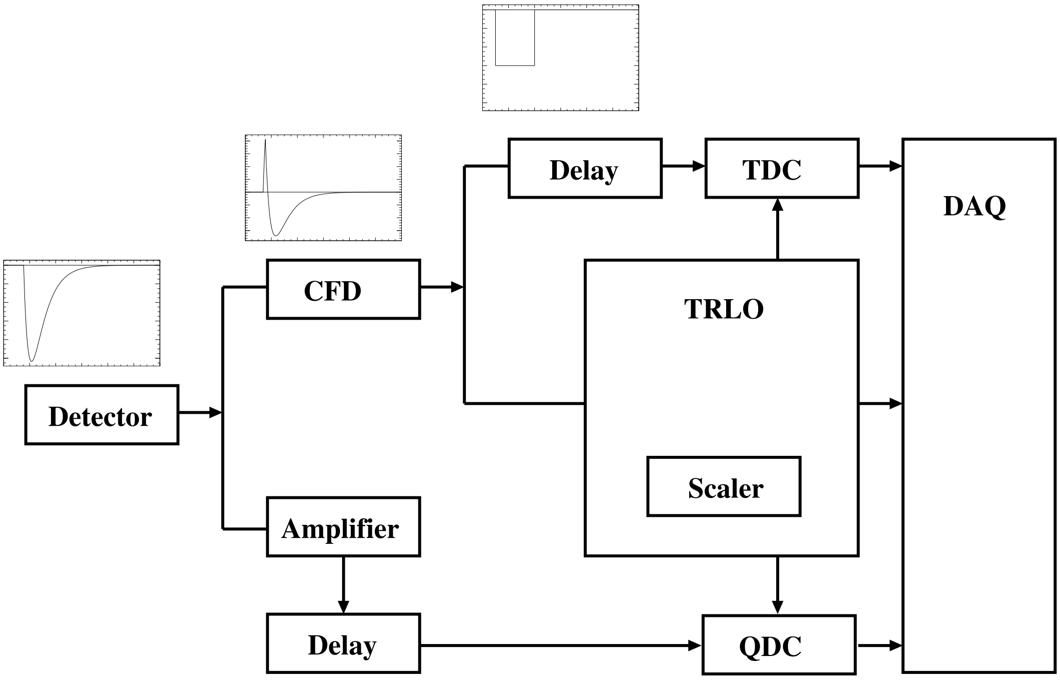

Figure 3.4.: Flow of the signal along the electronics chain. The upper and lower branches relate to the time and energy signal, respectively.

scintillator paddles were read out by PMTs on both sides and at least a multiplicity of two was requested in order to suppress background.

In case of Coulomb dissociation with neutron evaporation at least triggers from the POS (projectile), the TFW (fragment) and the LAND (neutron) were provided. Hence, combining the triggers of several detectors tentative reaction channels were tagged. The combinatorics was done by means of a trigger matrix, which is presented in table 3.3. In columns relevant input triggers to the VME Universal LOgic Module (VULOM), that did the TRLO, are given. Therefrom the output triggers shown in rows were generated while anti-coincident (first row) or coincident (second row) conditions were chosen. Each output trigger defined a bit (Tbit) of the so-called `Tpat` integer attributed to an event. Once finished this number was directly handed to the DAQ.

The POS trigger in anti-coincidence to ROLU (POS !ROLU) is also called the Good Beam trigger and indicates focused beam at the target position. The residual listed input triggers 3...11 were obtained from the named detectors, basically requesting suited multiplicities. Those were adapted to the actual detector performance, while high multiplicities were preferred in order to suppress background. The Spill On (A1) was distributed by the FRS monitor system, indicating beam at Cave C. The Early Pile-up trigger (A2) was exclusively generated from POS. Where, a time delay to the previous and next event was required. For the former, an event started a Time-to-Digital Converter (TDC), which was stopped by its delayed equivalent. In this way, simply the hardware delay was recorded and if the time deviated, the TDC was stopped by the (delayed) component of an earlier event. The latter was created when a TDC was started by a current event and stopped by the subsequent one. Finally, suited conditions based on both TDC times were adjusted. The Late-Trigger Kill signal (A3) was a pending trigger rejecting trigger decisions in a time window of 150 ns after the Good-Beam signal. In such a way extraordinarily late triggers were disregarded.

The triggers were aligned such that the widths of the signals overlay while Minimum Bias was always last in time. Hence, it served as the reference signal of the entire setup and all times and QDC gates of each event refered to the POS detector. In order to reduce the amount of potentially less important data and to minimise the DAQ dead time, triggers that didn't indicate a reaction were suppressed by scalers.

			Late-Trigger Kill	Early Pile-up	Spill On			XB Sum				TFW		LAND		POS !ROLU
Tbit	Name	VULOM slot														
		A4	A3	A2	A1	···	12	11	10	9	···	5	4	3	2	1
1	Min. Bias	0	0	0	0	···	0	0	0	0	···	0	0	0	0	0
		0	0	0	1	···	0	0	0	0	···	0	0	0	0	1
2	Fragment	0	0	1	0	···	0	0	0	0	···	0	0	0	0	0
		0	0	0	1	···	0	0	0	0	···	1	0	0	0	1
4	XB Sum	0	1	1	0	···	0	0	0	0	···	0	0	0	0	0
		0	0	0	1	···	0	1	0	0	···	1	0	0	0	1
8	Neutron	0	0	1	0	···	0	0	0	0	···	0	0	0	0	0
		0	0	0	1	···	0	0	0	0	···	1	0	1	0	1

Table 3.3.: Relevant part of the trigger matrix of the S393 experiment. The input and output triggers are listed in columns and rows, respectively.

Therefor the downscaling for Minimum Bias and Fragment events were set to 64 and 16, respectively, while reaction triggers like XB Sum or Neutron were not downscaled. Finally, gates for the charge-(Q)-to-Digital Converter (QDC) were distributed along with the master trigger to the TDCs by the TRLO.

Digitisation

The complete TRLO decision typically took around 500 ns defining the delays of the analog detector time and energy signal (see figure 3.4). Once the master trigger were distributed the electronics of all detector systems was directed to read contained data. In TDCs the time difference relative to the master trigger, that provided either the start or stop signal, was obtained. While time measurements in front of the target (S8, POS) were run in common-start mode, those TDCs behind the target (TFW, LAND) were operated in common-stop mode. The QDCs integrated the signal within the provided gate, which represents the energy-loss signal of the event.

A GSI brand Fastbus module served as DAQ hardware interface. Its dead time is 400 μs, which limited the maximum event rate to 2.5 kHz. The scalers of the TRLO were tuned accordingly. The DAQ itself was based on the GSI Multi Branch System (MBS) [40] that was adapted by H. Simon and H. Johansson to the requirements of the R^{3}B-LAND setup [41]. The MBS stores data packages of all involved detectors related to the event in List Mode Data (LMD) format files.

4 Detector Calibration

The binary data from the Data AcQuisition (DAQ) was recorded event-by-event in List Mode Data (LMD) format files. The present chapter provides an overview of the calibration routines of the `land02` framework, written by H. Johansson and maintained by R. Plag, and outlines how physically relevant quantities like positions on detectors, the ion charge, or the energy and momentum of particles were extracted from LMD files. The definition of physics events by means of the trigger matrix (table 3.3) is given in the last chapter. In addition to physics triggers, signals called `tcal` and `clock` were provided permanently in order to calibrate the detection system.

4.1 The `land02` Calibration Software

Within the calibration framework data is converted into a specified format by various embedded programs. There, several calibration steps are applied each requiring different calibration routines. The associated data levels are illustrated in the rectangle boxes in figure 4.1, while the calibration routines are shown in oval boxes. The reconstruction flow of binary data (top) to the complete calibration (bottom) of scintillator-based detectors like the TFW is exemplified. In general, times are given in nanoseconds (ns), positions in centimetres (cm) and energies in MeV. The involved data formats, additionally introducing the `TRACK` level, are briefly described in the following:

`RAW` data is not calibrated and given in units of channels of the readout electronics. For time measurements the TDC channels and for energy-loss measurements the QDC/ADC channels are accessible. The data level was used to check the status of a certain readout channel.

`TCAL` data of energy channels is corrected for their default-current offsets (pedestals), but are still given in arbitrary units. Times are given in units of ns. The parameters were calculated by the `clock` and `tcal` routines, respectively, from `RAW`-level data.

`SYNC` hronised data of detectors made of sub units is provided such that data of the individual components, for instance all photomutiplier tubes in the TFW, can be compared and combined. Time channels were attributed a common offset and energy channels were gain-matched.

`DHIT` denotes the detector-hit level. Positions, times and energy-loss information from individual detector components are combined and refer to detector-internal coordinates.

`HIT` s on detectors in the laboratory coordinates (x, y, z) are given. The geometry of the setup, *i.e.* the actual position of a specific detector in the experimental hall, still has to be defined at this level. Such detector positions were obtained from a photogrammetric measurement, which is described in detail in section B and a precise alignment of the in-beam DSSSDs, depicted and discussed in section 5.6.

`TRACK` level data were available for incoming particles and neutrons. Beyond calibration hits in various detectors were combined into trajectories. Neutron events in LAND were reconstructed by a so-called neutron volume algorithm [43] and the obtained angles and velocities were used in the further analysis. For incoming-particle identification the ion charge Z was deduced according to equation (3.3) and the mass-over-charge ratio A/Z from equation (3.1) with a specified $B\rho$ -value.

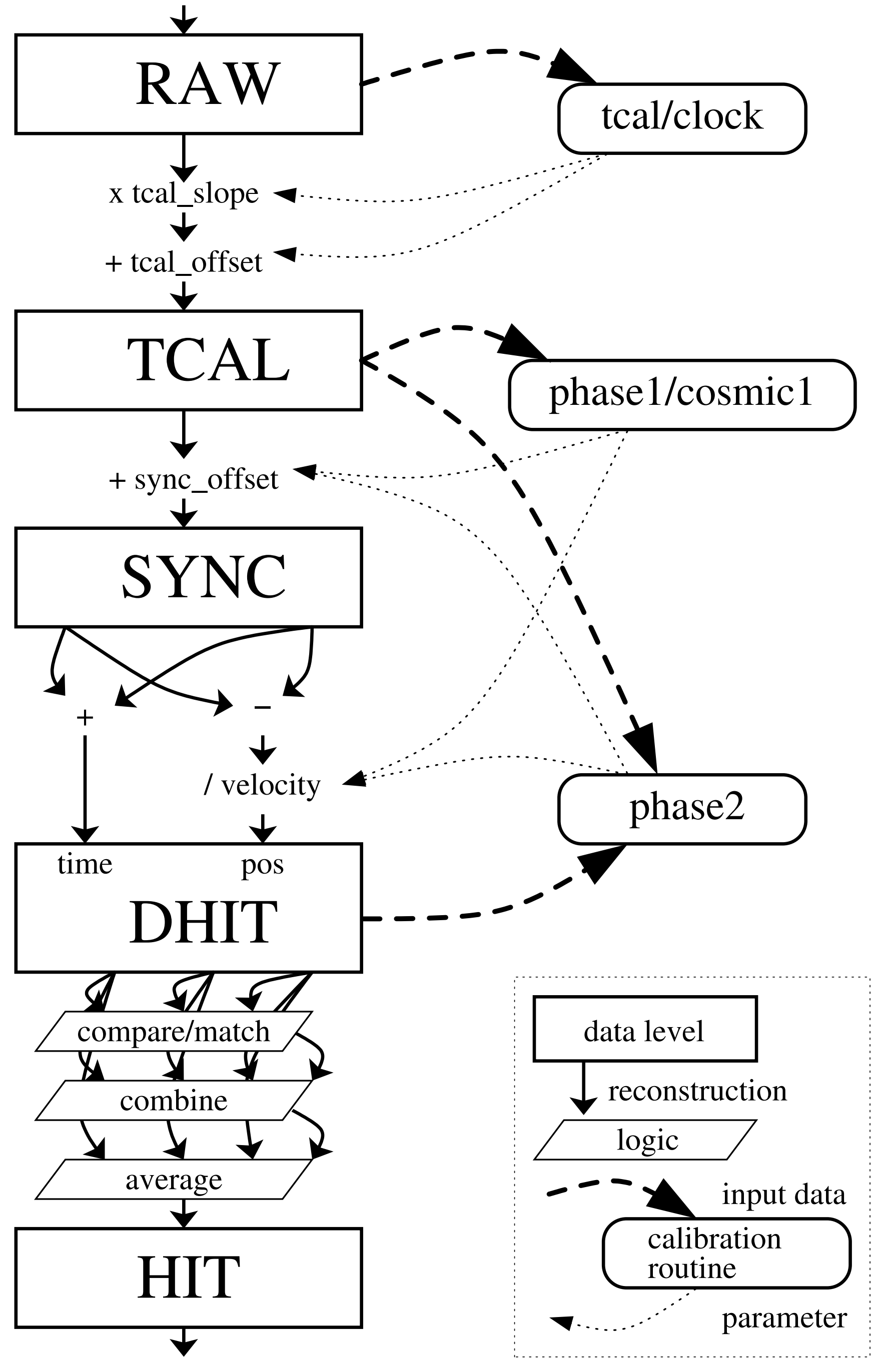

Figure 4.1.: Data reconstruction flow with `land02` from binary data (top) to the full calibration of the detector (bottom). Data calibration levels are shown in rectangles and the calibration routines in oval boxes. The scheme was taken from [42] and exemplifies the reconstruction of data from scintillator-based detectors like the TFW.

Projectiles and neutrons were determined by means of `TRACK` level data from `Land02`. For fragment identification a so-called `tracker` software described in detail in section 5.1.2 was utilised. It matches a prediction of the ion track through the magnetic field of ALADiN with measured detector positions behind the magnet and generates a fragment-mass spectrum. The gammas in XB from the de-excitation of the fragment were reconstructed with a so-called `addback` algorithm, which is depicted in section 5.4.1 and [44].

4.2 Incoming Particle Detectors

For projectile-velocity determination a long distance ToF measurement was carried out between the plastic scintillators S8 and POS. The ion charge was obtained from the cathode signal of the PSP. In the following the calibration steps for these detectors according to the scheme in figure 4.1 will be described in detail. All other calibration parameters were taken from the brain pool of the research group: many thanks to R. Thies, A. Movsesyan and C. Caesar.

4.2.1 Scintillator Detectors

The conversion of the TDC channels to `TCAL` level was carried out in a time dependent manner. Therefor approximately 100 min long blocks of recorded data were attributed a certain set of calibration parameters using the so-called `calscripts` routine, written by D. Rossi. In this way, fluctuations of the electronics response due to *e.g.* varying temperature were minimised. Furthermore, temporary misbehavior of readout channels was handled with this approach.

The time calibration signal consisting of a trigger and a start/stop of varying interval was distributed in this experiment by an electronics module called `TCalt`. Its signal was recorded along with the corresponding entries in the TDC channels by the DAQ. The `tcal` program in `Land02` approximates the correlation of the `tcalt` signals and the TDC channels with a straight line and returns the offset and slope. The case is exemplified for one photo multiplier of S8 in figure 4.2. The offset and slope express

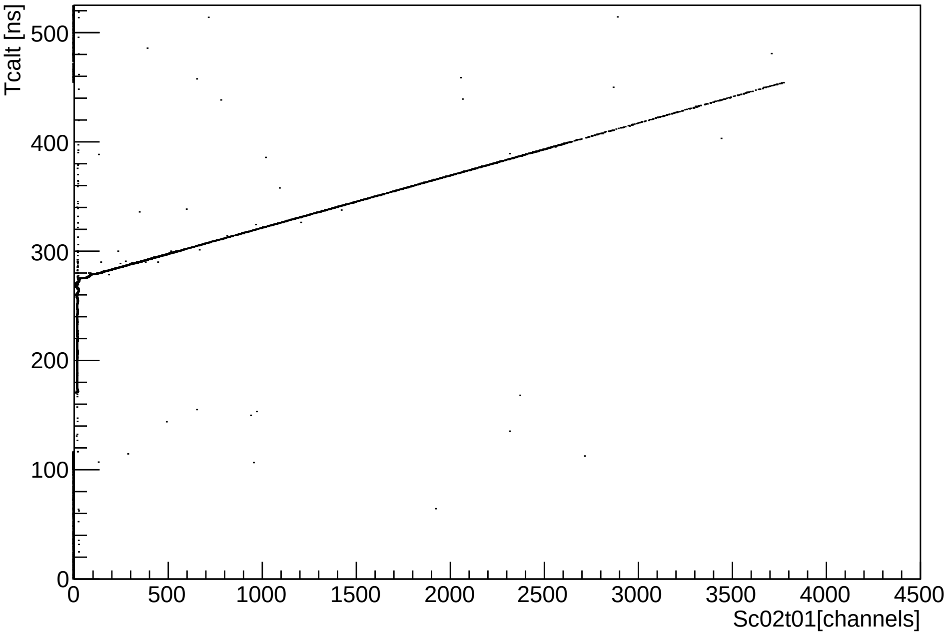

Figure 4.2.: Time calibration data of a TDC channel. The `Sc02t01` denotes a photo multiplier tube of S8.

the signal processing time of the electronics channel from the TDC to the DAQ and the TDC channel width, respectively. The values were inserted to the `TIME_CALIB` parameter.

For the calculation of `SYNC` level data two calibration runs with primary ^{40}Ar beam at different energies (run 340 with 474.5 AMeV, $\beta = 0.749$ and run 343 with 397 AMeV, $\beta = 0.713$) were taken. The linear interpolation of the correlation (Tof$\cdot\beta$) *vs.* β between S8 and POS yields slope and offset parameters m and n, respectively:

$$\mathrm{Tof} \cdot \beta = m \cdot \beta + n. \tag{4.1}$$

The slope m defines the time offset and was set in the `TIME_SYNC_OFFSET` of S8 in `Land02`. It is dependent on the signal processing time of the electronics chain until the TDCs, which basically includes the cable length to the Constant Fraction Discriminators (CFD) and these modules. The offset n in equation (4.1) can be used to calculate the distance between S8 and POS. An Extrapolation to $\beta = 0$ yields:

$$\mathrm{Tof} \cdot \beta = n = -185.5\ \mathrm{ns}. \tag{4.2}$$

Using $\beta = v/c$ with constant velocity $v = s/t$ and rearranging the terms results in:

$$s = -185.5\ \mathrm{ns} \cdot c = -55.6\ \mathrm{m}. \tag{4.3}$$

A negative value was obtained, because the ToF measurement referred to POS according to the trigger logic of the setup.

4.2.2 Semiconductor Detectors

The cathode signal of the PSP was utilised for incoming-charge identification. It was read out *via* an ADC and pedestal subtraction is not needed. For the conversion of ADC-channels to ion-charge units calibration runs with so-called $N = Z$ setting of the FRS were taken. There the transmission is optimised for nuclei with same proton and neutron numbers. Such, the energy-loss peaks can be attributed to charge states unambiguously, since ^{8}Be is unbound, that leaves a gap in the ADC spectrum. The case is illustrated for the PSP cathode called `Ps01_e05` in figure 4.3. Assuming linear response of the ADC an approximation by a straight line with offset and slope parameters was used to correlate the channel numbers of the energy-loss peak positions with ion charge numbers Z. Thereby the ion velocity was taken into consideration according to equation (3.3). The fit parameters were set the `ENERGY_ZERO_NOISE` and `ENERGY_DIFF_GAIN` values in `Land02`.

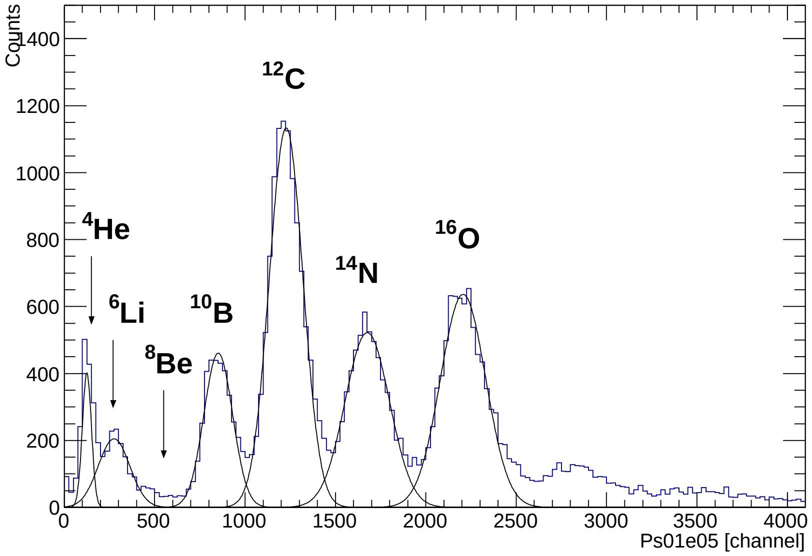

Figure 4.3.: Incoming ion charge identification in the ADC channel of the PSP cathode. The ^{8}Be state is unbound, which leaves a gap in the spectrum.

5 Data Analysis

Timing, position and energy-loss data of the calibrated detectors were utilised in a tracking routine in order to identify the reaction channel of interest, as described in the first section. Subsequently, the data normalisation and the handling of remaining background contributions are introduced. Employing Monte-Carlo simulations miming the prompt fragment de-excitation processes measured with XB exclusive cross sections can be obtained. The reconstruction of a ^{60}Co calibration source spectrum and the calculation of the integral efficiency uncertainty from such a simulation are described in the fourth section, where also the efficiency simulation for LAND is depicted. Furthermore, the reaction kinematics was reconstructed for the calculation of the energy-differential Coulomb-dissociation cross section based on the invariant-mass formalism in Section 5.5. Finally, an improved angular resolution in the target area when aligning the in-beam DSSSDs is presented.

5.1 Selection of the Reaction Channel

The secondary beam arriving at Cave C contained various isotopes besides the species of interest. The nuclei were characterised by specific $B\rho$ values from the FRS and separated using ToF and ΔE measurements, as described in the first section. Convenient conditions on the detected quantities (cuts) were chosen to select the reaction channel of interest. The beam particles undergo reactions in the secondary target at Cave C as well as in any material along its trajectory in the experimental setup. In addition to the background subtraction described in Section 5.3, cuts on the neutron velocity were applied in order to suppress background from LAND as illustrated in the last section.

5.1.1 Incoming Channel

For a given FRS setting the A/Z-ratio of the incoming particles was obtained from the magnetic rigidity $B\rho$ of the central beam-trajectory according to formula (3.1). Therefor the velocity was deduced from a ToF measurement between S8 and POS. The PSP provided the charge Z of the nuclei. In figure 5.1, the elliptical cut applied to select ^{18}C is presented in the two-dimensional plot Z *versus* A/Z. The ^{18}C projectiles can be distinguished clearly from the rest.

Note that in the course of the experiment events with delayed times in S8 were observed. In that case the nuclei likely impinged on or close to a blind spot on S8 yielding too little scintillation light in the paddle in order to produce signals in both photo multipliers. Hence, the delayed time may have been induced by a subsequent particle while the proper signal was running through the signal processing branch. The effect can be illustrated in the correlation plot of both S8 times and reflects in bands along the A/Z-axis in the incoming-particle identification plot, shown in figure 5.2 and 5.3, respectively. Events with valid times are indicated by the green ellipse and those with just one proper signal are covered by the adjacent red zones. The major axis of the ellipse reflects the momentum spread of the projectiles while the minor axis is related to the transmission time of the scintillation light in S8. The latter is small compared to the fluctuations due to the missing time, which consequently was ignored for events with just one valid time. In such cases the S8 time was calculated from one time. This introduces an additional ToF uncertainty of less than one percent, but recovers around 25% of ^{18}C projectiles.

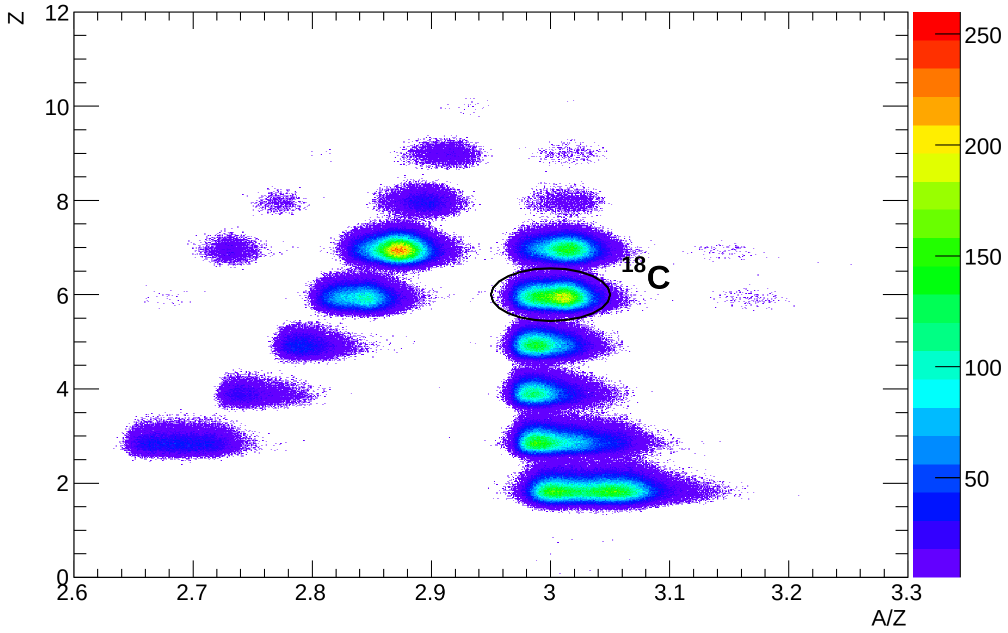

Figure 5.1.: Projectile identification plot, where ^{18}C is selected.

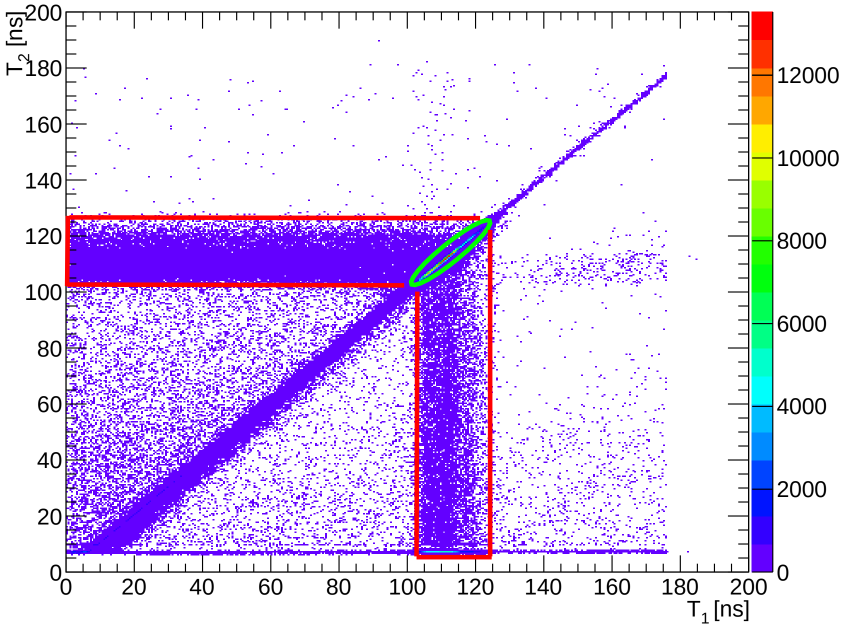

Figure 5.2.: Correlation of the S8 times.

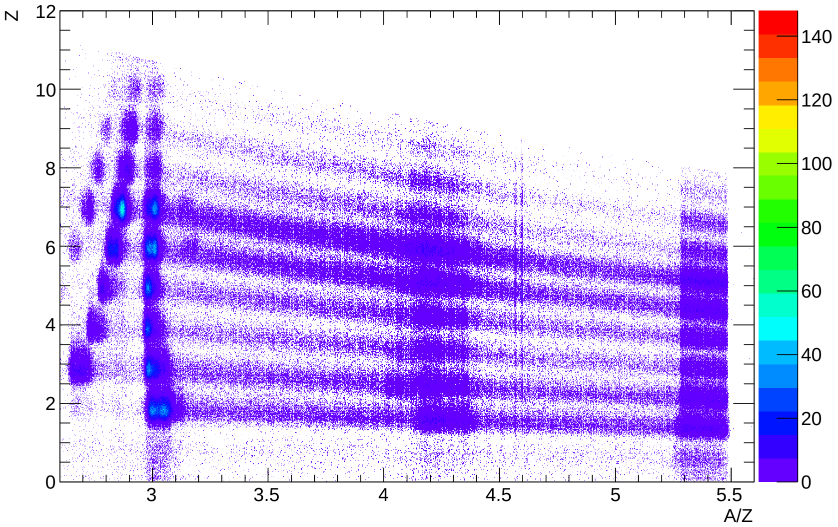

Figure 5.3.: Effect of missing or invalid S8 times on the incoming identification plot, appearing in bands.

5.1.2 Outgoing Channel

Due to the relativistic energies of the projectiles ($\beta \approx 0.73$) the reaction products are strongly forward boosted. The experimental setup is designed to detect projectile-like fragments in terms of mass, charge and velocity, and light particles at the same time. The selection of the reaction channel strongly relies on the tracking of the fragments by means of position and time measurements as well as the charge determination before and after ALADiN. For the neutron identification simply a LAND trigger indicating a coincident neutron event was sufficient.

Fragment-Mass Determination

The description of the passage of charged particles through a dipole field relies on the balance of the centripetal and Lorentz forces:

$$B\rho \propto \frac{A}{Z}\beta\gamma. \tag{5.1}$$

The trajectory, *i.e.* the curvature ρ, can be deduced from position measurements before the dipole magnet in the DSSSDs behind the target, and behind ALADiN utilising the GFI and the TFW. The ToF measurement was obtained using the POS and TFW detectors and the charge Z was provided by the TFW.

The situation is sketched in figure 5.4. In the field free regions the fragment trajectory is assumed to be straight, while it is replaced by a piece wise linear-curve inside the magnet. The position in front of ALADiN and the angle with respect to the z-axis are obtained from the DSSSDs behind the target. Based on a field map, *i.e.* the measured magnetic field, the Lorentz force is calculated at each step (step length $\mathcal{O}$(cm)) along the track in ALADiN for assumed A/Z and β values. In this way, a curvature results and crossing points with the detectors behind ALADiN are obtained. In an iterative procedure the β is varied starting from the projectile β in order to match the measured ToF. At the same time the fragment mass A is tuned to overlay the calculated trajectory with the position measurements after ALADiN.

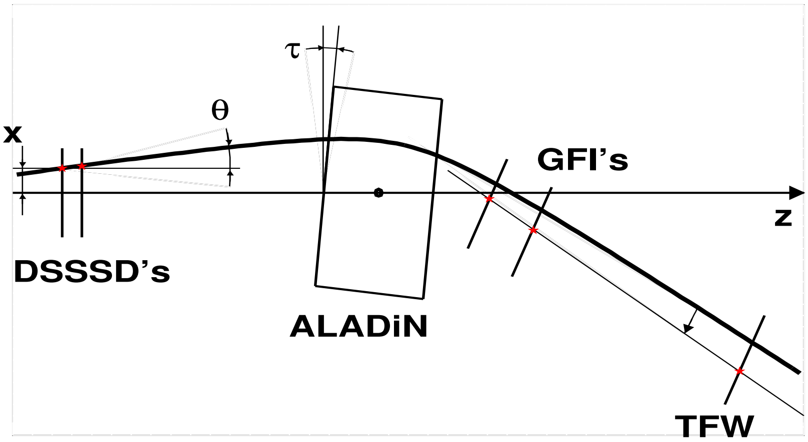

Figure 5.4.: Trajectory of a charged fragment in the experimental setup. In the tracking the mass A and velocity β are varied to fit the calculated trajectory to the position measurements (red) before and after ALADiN.

Fortunately a tracker software written and maintained by R. Plag was available [45] calculating the fragment mass as depicted afore. Therefor the relevant detector positions as well as the angle τ of ALADiN with respect to the x-axis obtained from the photogrammetric measurement (see section B) were utilised. The usage of the tracker requires a calibration procedure where the adaption of the measured to the calculated ToF is most important. Therefore, the flight path and the energy loss along the trajectory needed to be taken into account. Subsequently, the detectors before and behind ALADiN were aligned to minimise the respective residuals with respect to a straight line. Note that the position corrections applied are covered by the uncertainty of the corresponding position from the photogrammetric measurement.

In figure 5.5, fragments with charge $Z = 6$ from the tracker for ^{18}C projectiles on lead target in coincidence with a neutron trigger are shown. The peaks are correlated to non-reacted beam and several neutron removal channels. They are cleanly separated and for ^{18}C the relative mass resolution is around 1.1% for an empty-target run. The tracker calibration was performed relative to the trajectory of non-reacted particles for incoming ^{18}C projectiles. Hence, the mass resolution may vary strongly for incoming nuclei with different mass or velocity. Thus, a separate calibration may be required in such cases. When the detector positions from the photogrammetric measurement are utilised fragments in the mass range ^{18}C to ^{12}Be with constant A/Z-ratio have been tracked with comparable relative mass resolution using the same calibration. Along the isotopic chain, ^{17}C with 2.5% lower velocity with respect to the calibration nucleus, and ^{15}C, bent by a changed magnetic field, have been tracked with similar mass resolution.

5.1.3 Neutron Background

The fragment tracking detectors behind ALADiN were located rather close to LAND. This caused considerable background from reactions of fragments after passing the dipole field when reaction products were scattered into LAND. Thus, in figure 5.5, even though a neutron was required, ^{18}C fragments still appear in the mass spectrum of ^{18}C projectiles.

If the created particles reach LAND while the electronics gate is open, they are identified as neutrons. Since they travel along a longer distance when being scattered into LAND, they appear significantly slower. This is illustrated in figure 5.6 for ^{18}C impinging on lead target. The effect is strongest for ^{18}C fragments, *i.e.* non-reacted beam, and decreases gradually with increasing neutron-removal number. Ac-

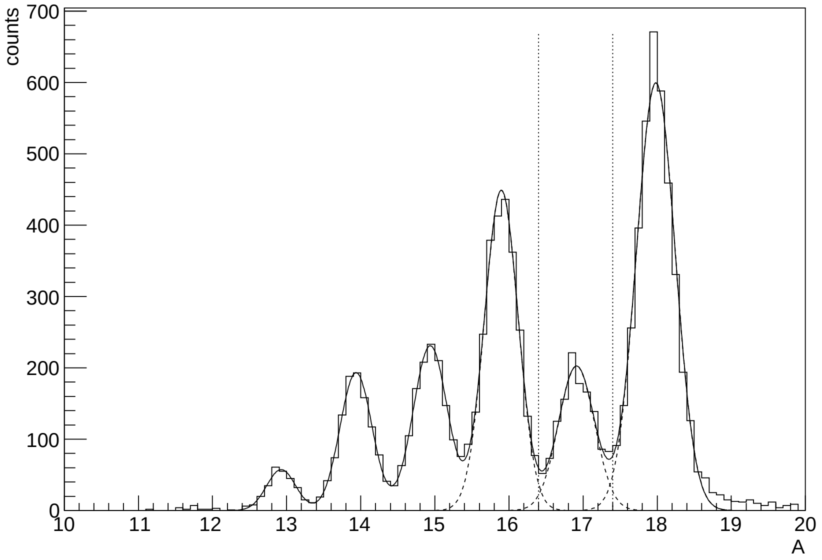

Figure 5.5.: Neutron removal channels, identified *via* the tracked fragment mass for ^{18}C projectiles impinging on lead target in coincidence with a neutron trigger. Also indicated is the gate on the one-neutron removal channel.

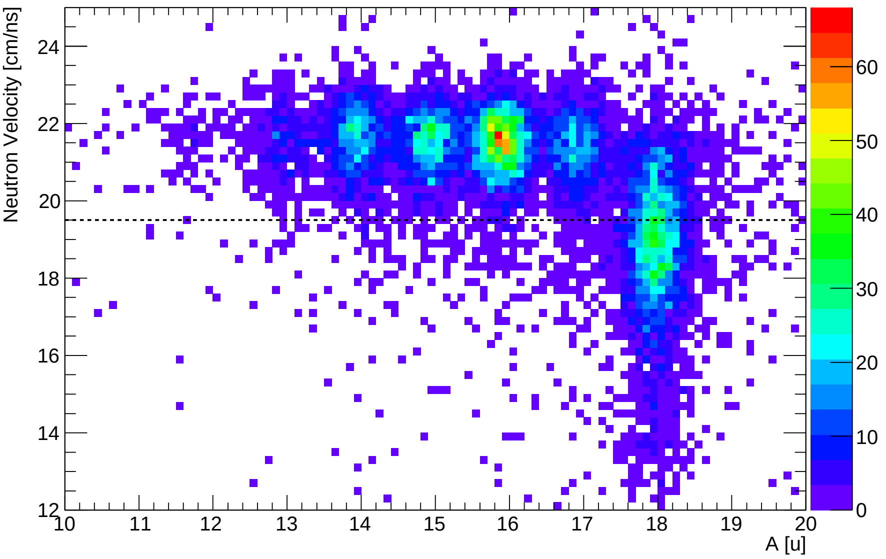

Figure 5.6.: Neutron velocity versus the reconstructed fragment mass for the $^{18}\mathrm{C}(\gamma,\mathrm{n})^{17}$C reaction channel. The dashed line represents the neutron velocity cut.

cording to formula (3.1) for fragments of similar charge and velocity the relation $\rho \propto A$ for the curvature ρ and mass number A holds and lighter fragments are deflected stronger off the LAND direction.

For a 426 AMeV beam a lower neutron-velocity cut at $v_n = 19.5$ cm/ns translates into an upper neutron energy of around 10 MeV in the rest frame of the beam in case the neutrons were emitted backwards with respect to the beam direction and in the projectile rest-frame. In the theoretical description of ^{18}C Coulomb breakup [20], neutrons with kinetic energies up to 15 MeV are generated. Hence, the neutron velocity cut effects the high-energy tail of neutrons emitted in backward direction, but this fraction is negligible.

5.2 Data Normalisation

The reaction probability p relates the number of reactions N_r to the total number of projectiles N_p:

$$p = \frac{N_r}{N_p}, \tag{5.2}$$

while the acceptance a_{det} and efficiency ϵ_{det} of the detectors, the cut efficiency of the reaction channel ϵ_{cut} as well as the dead time of the Data AcQuisition system (DAQ) ϵ_{daq} have to be taken into consideration. When the incoming particles are treated in the same way like the reacted ones in terms of efficiencies and cuts and the mentioned corrections are considered, equation (5.2) turns into:

$$p = \frac{a^r_{det} \cdot \epsilon^r_{det} \cdot \epsilon^r_{cut} \cdot \epsilon^r_{daq} \cdot N_r}{a^{ur}_{det} \cdot \epsilon^{ur}_{det} \cdot \epsilon^{ur}_{cut} \cdot \epsilon^{ur}_{daq} \cdot N_{ur}}, \tag{5.3}$$

and the data normalisation in the denominator in equation (5.2) can be obtained from the number of tracked fragments. Here, the subscript ur denotes unreacted particles.

The intrinsic efficiency and geometrical acceptance of the detectors along the fragment branch cancel out, if the projectiles and fragments interact similarly with matter along their trajectory and if the spacial beam profile of fragments and not-effected particles are well covered by the tracking detectors. The latter was guaranteed from the layout of the experimental setup. The intrinsic detection efficiency depends on the reaction probability of crossing radiation and the number of charge carriers, *i.e.* the amount of scintillation light created therein. It is similar for reacted and non-reacted beam, since the effective nuclear-matter radii reflecting the total interaction probability, of ^{17}C and ^{18}C have been extracted in [46] and were found to differ by only 3.5%. Note that for the detectors of reaction products like gammas or neutrons efficiency corrections gained from simulations have to be applied. The corrections are described for the XB detector and LAND in Section 5.4.1 and 5.4.5, respectively.

When a fixed cut is applied to data the selected fraction may deviate for different reaction channels. The characteristics of the respective reactions can slightly modify a spectrum, *e.g.* caused by the validity range of calibrations. Therefore, each spectrum was approximated separately by a Gaussian distribution and the cuts were set with respect to a fixed fraction of the fit function. In this way, the cut efficiencies ϵ_{cut} of unreacted and reacted beam are similar and cancel in equation (5.3), too.

The dead time of the DAQ once an event was accepted by the trigger logic was limited by the Fastbus module, that served as hardware interface, to 400 μs (see Section (3.2.5)). Since the trigger logic was referred to POS, which defined the master gate, each entry in all other detectors (which was recorded by the DAQ) can be related to a POS entry. Thus, the according efficiency ϵ_{daq} is identical for fragments N_r and not-affected particles N_{ur}.

The detector with the slowest response defines the minimum time-span between subsequent events, otherwise pile-up occurs. Since not all the events are passed to the DAQ, this delay can be shorter than the dead time of the DAQ. In the experiment presented here the time constraints were given by the PSP, which typically creates signal lengths in the range of a few microseconds. The pile-up cuts were set by means of the `tprev` and `tnext` time conditions of the event, generated from POS times with Good-Beam trigger (see Section (3.2.5)). The latter time condition was created by a TDC, which was started by the current event and stopped by the subsequent POS signal. For `tprev` the POS signal started a TDC which was stopped by its delayed equivalent. Such, simply the adjusted hardware delay was recorded and if the time deviates, the TDC was stopped by the (delayed) component of the previous event. In this analysis time delays of `tprev` $\approx 5\,\mu$s and `tnext` $> 10\,\mu$s were required in order to reject pile-up.

The number of unreacted fragments N_{ur} was finally obtained from the fragment charge distribution on the TFW, which is shown in figure 5.7 for different target runs. The approximated multiple Gaussian curves adjusted to each target reproduce data precisely for carbon fragments at $Z \approx 6$. The case is illustrated for lead target data by the red data points. For data normalisation a 3σ region around the carbon charge was chosen taking into consideration the downscaling of the TFW trigger. The individual fits fully overlay there.

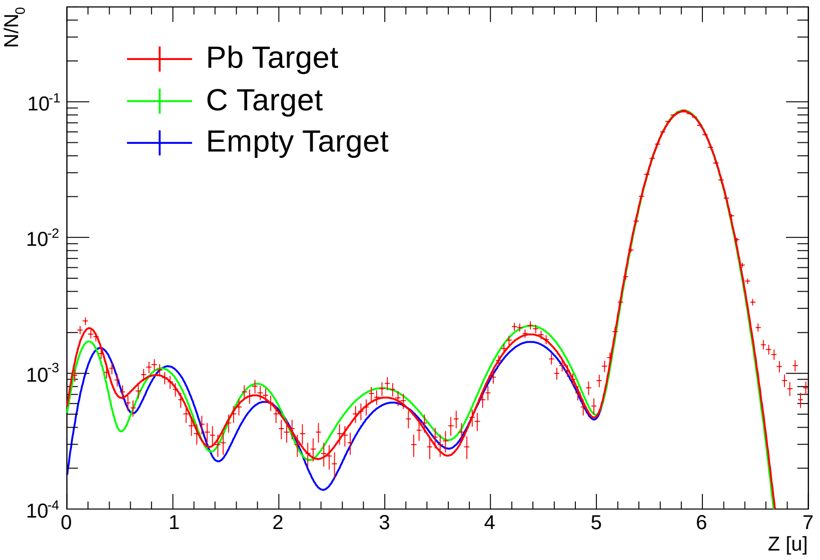

Figure 5.7.: Fragment charge distribution on the TFW. For data normalisation a region of $\pm 3\sigma$ around the charge of carbon was chosen.

5.3 Background Subtraction

The Coulomb dissociation (CD) reaction channels were defined by means of the neutron removal channels in the fragment mass spectrum in coincidence with neutrons in LAND. There is still contamination with events from different reaction mechanisms, which cannot be distinguished visually. Those contributions stem from nuclear interactions of the beam in the target and non-specific reactions along the particle trajectory. The latter can be estimated from data taken without a target, so-called empty-target (Mt) runs. Then the beam positions on the tracking detectors of the fragments differ slightly, since no multiple scattering in the target material occurs. The target runs additionally have to be corrected for reactions like fission in the target, resulting *e.g.* in symmetric fragment masses. Such contributions cannot be detected by the setup, since they are not in the mass domain of the projectiles. The procedure is described in Section 5.3.1.

The virtual-photon flux in relativistic electromagnetic collisions scales with Z_T^2, which denotes the charge of the target, according to equations (2.13) to (2.15). Hence, electromagnetic excitations are suppressed for carbon target (C) as compared to lead target (Pb). Palit *et al.* [47] moreover demonstrated for breakup of ^{11}Be on lead and carbon target that carbon-target data practically contains exclusively reaction products from nuclear breakup. Those in general comprise diffractive dissociation and inelastic breakup reactions while for the latter the probability to detect a neutron in LAND was found to be negligible [48], since such neutrons will not appear in the projectile rapidity-domain.

The cross section σ is calculated by relating the interaction probability p to the number of targets N:

$$\sigma = p \cdot N. \tag{5.4}$$

For a certain target run N_T is written as:

$$N_T = \frac{M_{mol}(T)}{d_T \cdot N_A}, \tag{5.5}$$

where $M_{mol}(T)$ is the molar mass of the target material, d_T is the target thickness in g/cm^3 and N_A is the Avogadro number (T=$Pb/C/Mt$). Because the background contributions from reactions along the particle track stem from diverse processes, it is impossible to define a reasonable cross section. Hence, it must be subtracted on the interaction probability level and the Coulomb-dissociation interaction probability can be expressed as:

$$p_{CD} = (p_{Pb} - p_{Mt}) - (p_C - p_{Mt}) \cdot \left(\alpha_{Pb} \frac{N_C}{N_{Pb}} \right). \tag{5.6}$$

Where the fraction N_C/N_{Pb} relates the number of target nuclei and α_{Pb} is a scaling factor according to the nuclear size related to the subtraction of the nuclear contribution. The nuclear-interaction cross section correlates with the radii of the interacting nuclei. Since measured with carbon, it has to be rescaled for lead target. There are various semi-empirical models available to obtain the scaling, dependent on the mass region of the projectile [49]. In this work α_{Pb} was derived from experimental data. In figure 5.8, the Coulomb-dissociation interaction probability according to equation (5.6) for ^{18}C projectiles is shown. The region limited by the dotted lines comprises the fragment charges $Z = 2 \ldots 5$ from the TFW and indicates reactions with proton removal. Since for ^{18}C the proton separation energy is 26 MeV [3] and the maximum excitation energy from Coulomb excitation equation (2.9) in this experiment is $\epsilon_{max} = 19.2$ MeV, those channels have exclusively been populated *via* nuclear reactions. Therefore, the integral over the mentioned neutron-evaporation channels in figure 5.8 was minimised tuning the nuclear scaling in equation (5.6). Finally, $\alpha_{Pb} = 1.65$ was found which compares to the value $\alpha_{Pb} = 1.38$ derived from the parametrisation for the nuclear contribution in cross section measured using heavy targets [49]. The deviation can be traced back to the uncertainties of both approaches. However, in this analysis the former value was utilised, since it was extracted at the actual experimental conditions.

Normalised empty-target data are subtracted twice; from both target runs. This overestimates the statistical uncertainty derived from equation (5.6) when both subtractions are treated like independent measurements. Hence, it is useful to rearrange the Coulomb-dissociation interaction probability:

$$p_{CD} = p_{Pb} - p_C \cdot \alpha_{Pb} \frac{N_C}{N_{Pb}} - p_{Mt} \cdot \left(1 - \alpha_{Pb} \frac{N_C}{N_{Pb}} \right). \tag{5.7}$$

With equation (5.4) the Coulomb-dissociation cross section can finally be expressed as:

$$\sigma_{CD} = p_{Pb} \cdot N_{Pb} - p_C \cdot \alpha_{Pb} N_C - p_{Mt} \cdot (N_{Pb} - \alpha_{Pb} N_C). \tag{5.8}$$

In this way, integral cross sections can be calculated from the fragment-mass spectrum. In this work the expression was also used to drive excitation-energy spectra for the Coulomb-dissociation reaction channel.

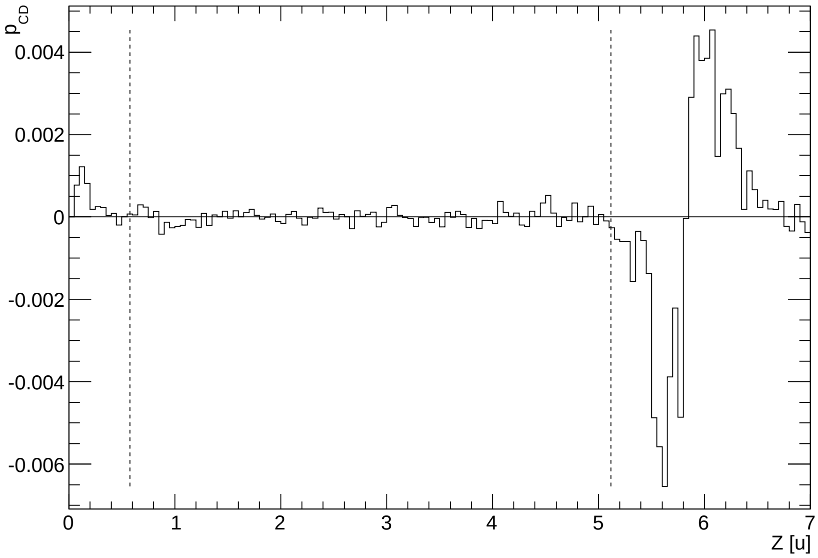

Figure 5.8.: Fragment-charge spectrum obtained from equation (5.6) for the calculation of the nuclear-scaling factor α_{Pb}. The dotted lines indicate the region where the integral of the subtracted spectra was minimised.

5.3.1 Scaling of Target Runs

In the target various types of interactions take place with reaction products that are not in the mass or velocity acceptance of the setup. Hence, such events cannot be detected. The effect reveals in the fragment-mass spectra of the target runs when empty-target data are subtracted.

In figure 5.5, the fragment mass for incoming ^{18}C impinging on lead target is shown. The distribution at the projectile mass arises from neutron background (see Section (5.1.3)) and is not related to target issues. Since the fragment hit-positions on the tracking detectors are roughly similar for different target runs, the probability distributions for unreacted beam at $A = 18$ should be comparable and cancel in the subtraction of empty-target data. The situation is illustrated for incoming ^{18}C in lead-target runs in figure 5.9. To correct for reactions in the target, the interval indicated by the dashed lines in the subtracted fragment-mass distribution was minimised. The limits of just 2σ around the $A = 18$ peak obtained from an approximation of the fragment-mass spectrum with a Gaussian were chosen to avoid overlap with the first neutron-evaporation channel and were set symmetrically around the mass of the projectile. In fact, lead-target (2145 mg/cm^2) and carbon-target (935 mg/cm2) data have to be enhanced by 5.2% and 5.3%, respectively, in order to balance the subtraction around the projectile mass at $A = 18$.

Apparently too much empty-target data were subtracted, or in turn data got lost in the according target runs. Ozawa *et al.* [50] have measured the reaction cross section of ^{18}C on a carbon target at 80 AMeV by means of the transmission method [51], which quantifies non-specific absorption in the target. An extrapolation to higher energies employing experimental data at 950 AMeV and utilising the Glauber method [51] was performed as well. Therefrom, a reaction cross section of around 1000 mb for ^{18}C on carbon at 500 AMeV can be estimated, which translates into a rescaling by 5.8% for the carbon-target run. This differs from the applied value, since in the transmission method inelastic scattering was explicitly considered while a non-specific analysis was carried out in the frame of this work.

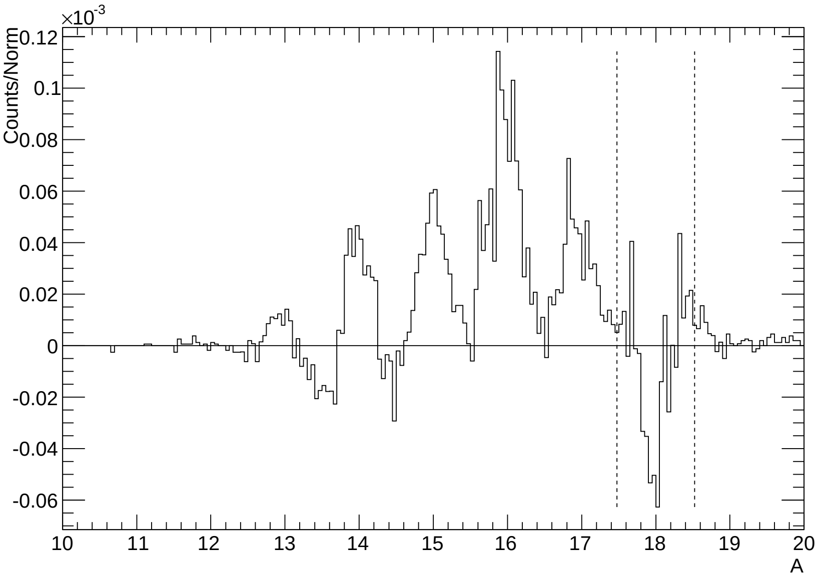

Figure 5.9.: Re-scaling of the lead-target run for incoming ^{18}C. The interval there the fragment-mass distribution was minimised is indicated by the dashed lines.

5.4 Efficiency Calibration of Detectors for Reaction Products

Neutrons and gammas from Coulomb-dissociation reactions are detected in LAND and XB, respectively. These detectors are comparably complex and composed of various sub-elements. Incident particles can take part in manifold sequent interactions with the detector material, that leave typical patterns in terms of energy depositions, positions and timing. Therefore, reconstruction algorithms have to be employed to obtain explicit information on the intrinsically incident particles. The detector performance, amongst others, depends on the physics case (*e.g.* number of incident particles), properties of the detector elements (*e.g.* electronics thresholds, resolution) and the characteristics of the particle interaction with the detector material. Additionally to the efficiency of the reconstruction algorithm, the cut efficiency and geometrical acceptance have to be considered.

The efficiency corrections were found by means of dedicated simulations for the detectors. In the following, the reproduction of a ^{60}Co Source run with XB and the calculation of integral XB-efficiency uncertainties of the simulations is described. The last section is devoted to the efficiency correction for LAND.

5.4.1 Crystal Ball Simulations of a ^{60}Co Calibration Source

The simulations were carried out with the `R3BRoot` simulation and analysis framework. It is based on the FairRoot library and specific parts of the R^{3}B-LAND experimental setup are implemented. This includes detector geometry and materials, magnetic field-maps, detector hit-registration, a dedicated physics list for low-energy neutron- and γ-interactions and nuclear-fragment transport, and dedicated event generators [52].

The `Geant3` material, physics and data-handling classes have been employed for the simulation of XB events. All XB crystals installed in the S393 experiment as well as the aluminium wrapping, the target wheel, each DSSSD plus holding structure, readout boards and housing, and the target ground-plate were implemented. The standard physics processes were used. In figure 5.10, a typical event with

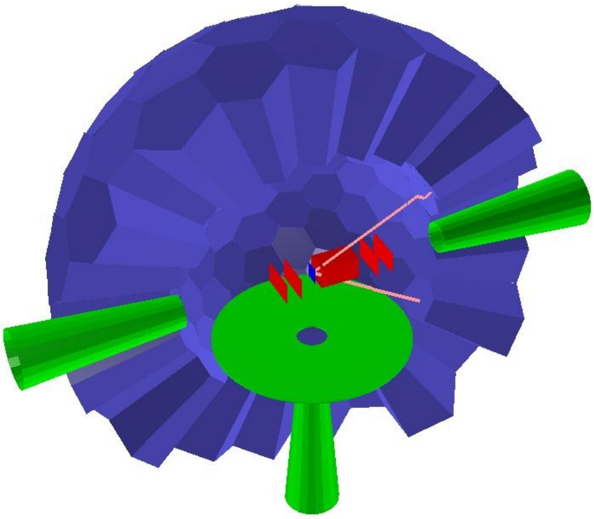

Figure 5.10.: Simulated particle-tracks (pink) of gammas in XB in the implemented detector geometry: the crystals (blue), DSSSDs (red) and basic holding/housing structure (green) are shown.

coincident gammas from the decay of ^{60}Co is shown; the particle tracks are indicated in pink. Each point of the piecewise linear-curve represents an interaction with material.

The beta decay of ^{60}Co:

$$^{60}\mathrm{Co} \rightarrow ^{60}\mathrm{Ni} + e^{-} + \bar{\nu}_e, \tag{5.9}$$

leaves the daughter nucleus in the 4^{+} state at 2.51 MeV in 99.9% of the cases as illustrated in figure 5.11. These transitions exclusively cascade to the ground state *via* the first exited state and two coincident gammas with energies $E(\gamma_1) = 1.333$ MeV and $E(\gamma_2) = 1.173$ MeV are emitted [53]. In the work presented here the KE565 ^{60}Co source from the RISING group was utilised. From a sequence of previous

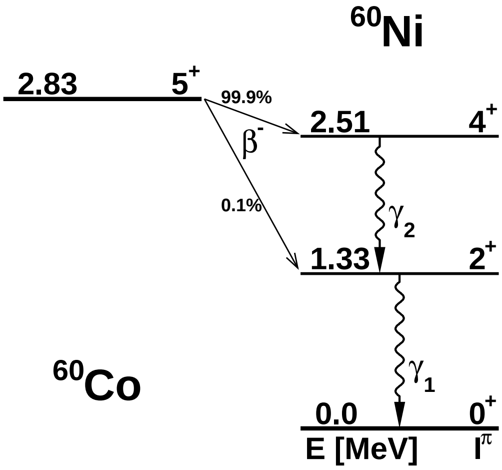

Figure 5.11.: Term schema of ^{60}Ni related to the beta decay of ^{60}Co [53]. The excitation energies and the Q-value refer to the ground state of ^{60}Ni.

	Crystal Number									
Permanently	77	81	82	103						
Source Run	7	20	21	49	52	56	63	70	71	78
	80	89	91	92	94	100	101	120	136	151

Table 5.1.: Crystals that were excluded from the analysis of the ^{60}Co source run.

measurements an activity of 135 kBq at the time of usage was extracted. Hence, pile-up events from the source can be neglected.

The source was placed at the centre of XB in the target position and the calibration run 644 was recorded with air-vented target area while the crystals were run at experimental conditions in the closed configuration with respect to the target chamber. A time-dependent energy calibration, convenient for data taken with beam (Doppler broadening), was utilised in the first place. But since the two γ-energies are close with respect to the energy resolution of the NaI-crystals, an energy recalibration for the source run was finally carried out. Still, 20 crystals showed insufficient separation of the γ-peaks and, hence, were excluded from the analysis in addition to those that were permanently skipped (see table 5.1). Since the simulations were run at exactly the same conditions, this does not effect the calculation of the integral XB-efficiency uncertainties.

Each detector threshold has been extracted by M. Holl from carbon projectiles on carbon target with XB-Sum trigger. There, comparably high energy entries in XB from nuclear reactions are expected due to high transition energies of the excited states of the fragment. Then low-energy entries have been approximated by a Gaussian and the threshold was set well beyond the distribution. In this way, additionally to the correction of the pedestals from electronics background from the crystal and (low-energy) target-material excitations were taken into consideration. Events with entries higher than the end-point energy of the relevant ^{60}Ni de-excitation spectrum at $E = 2.6$ MeV, when accounting for the detector resolution, were also disallowed.

The photopeak efficiency ϵ is the number of gammas, that deposit their entire energy in a detector N_{full} divided by the number of incident gammas N_{inci}:

$$\epsilon = \frac{N_{full}}{N_{inci}}. \tag{5.10}$$

It is dependent on the geometry and intrinsic detector efficiency, and material along the path of the γ from the source to the detector. In the coincidence approach the photo peak efficiency can be obtained when at least two subsequent gammas are emitted from the calibration source. They are defined in the energy spectrum *via* entries in a fixed region around the corresponding full-energy peak $E(\gamma)$. While one γ serves as the trigger and defines N_{inci} the other is requested and N_{full} is obtained. In this way, the efficiency per detector for the transition energies can be determined. In the case of the ^{60}Co source this yields for the energy $E(\gamma_1)$:

$$\epsilon(E(\gamma_1)) = \frac{N_{full}(E(\gamma_1))}{N_{inci}(E(\gamma_2))}, \tag{5.11}$$

and *vice versa* for $E(\gamma_2)$. For the calculation of the intrinsic photo peak efficiency the solid angle covered by the crystal with respect to the entire solid angle has to be taken into account. This introduces the additional factor:

$$\epsilon_{geom} = \frac{4\pi/162}{4\pi} = \frac{1}{162}. \tag{5.12}$$

In [54] the intrinsic efficiency per crystal in the coincidence approach utilising a ^{60}Co source was extracted. From an approximation with a Gaussian average efficiencies of the distribution of crystals $\epsilon(1.333\ \text{MeV}) = (51 \pm 1)\%$ and $\epsilon(1.173\ \text{MeV}) = (55 \pm 1)\%$, both with $\sigma \approx 11\%$, were attained and the energy dependent efficiencies were be calculated from equation (5.11). Entries in the lower energy interval can stem from both transitions. Additionally, a random coincidence can indicate a higher transition. While when gating on the higher energy just the higher transition is allowed independently of coincidences. Thus, $\epsilon(1.173\ \text{MeV})$ is higher than $\epsilon(1.333\ \text{MeV})$. However, in that analysis just crystal 78 in addition to those permanently disregarded was excluded.

The momentum component in beam direction of gammas emitted from beam particles is Lorentz boosted according to the (relativistic) energy of the beam. Hence, in order to obtain the de-excitation energy of the fragment a Doppler correction dependent on the angle of the gamma against the beam direction has to be applied. In case the gamma energy was spread groups of crystals (clusters) with energy and time entries are recorded. Therefore, the crystal that the gamma initially hit has to be reconstructed utilising the so-called `addback` algorithm [44] while also adjacent energy entries are summed up. The procedure is accompanied by a Doppler broadening of typically 100 keV at beam energies of 500 AMeV due to the solid angle of the crystals surface facing the target. In the reproduction of the ^{60}Co source run by means of simulated data the cluster performance of the `addback` was tested and spectra from reconstructed clusters were analysed, although no Lorentz boost occurred.

Experimental background in the source run mainly arises from the decay chains of primordial nuclei, the decays of ^{40}K and ^{137}Cs, and secondary cosmic rays. From the latter just muons are of interest, because of their high production rate and penetration strength [55]. For the background estimation a run without calibration source was taken, in the following referred to as cosmic run. Note that for data taken with beam, which has to fulfil a complex trigger decision the background component as described above is irrelevant.

In figure 5.12, the decomposition of a single-cluster energy spectrum from the ^{60}Co run into a simula-

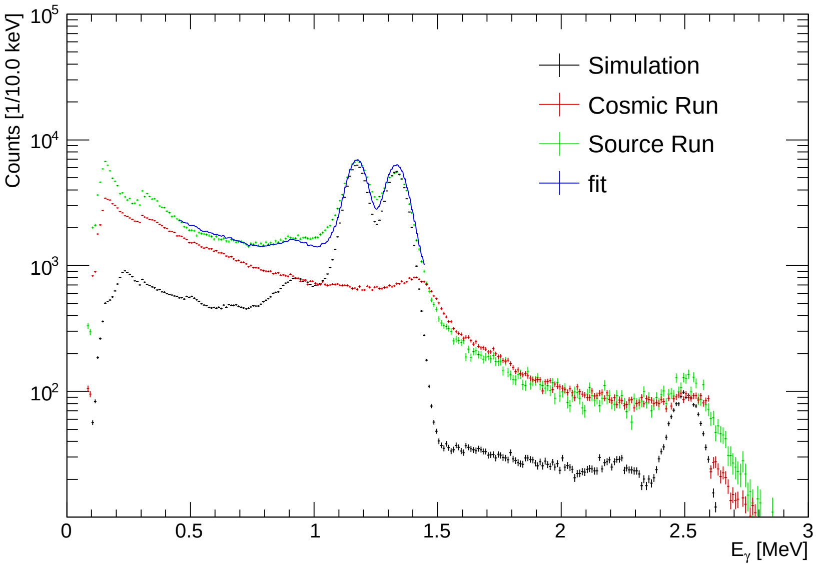

Figure 5.12.: Composition of a ^{60}Co source run from a simulation and a cosmic run. The fit was performed in a wide range around the full energy depositions of the emitted gammas as indicated.

tion and a cosmic run is shown. In addition, the region where the spectra have been adapted is indicated by the fit function. It shows good overall agreement and particularly reproduces the full-energy peaks sufficiently precisely. The energy entries of the simulations have been randomised according to the respective detector resolution. Those have been extracted from the series of calibration runs with ^{22}Na and ^{60}Co sources taken in the course of the entire experiment. No time drift of the detector resolutions was observed.

The source run (*src*) can be decomposed into the bare simulation of the ^{60}Co decay and background events. The photopeak efficiency ϵ^{src} according to equation (5.10) can hence be expressed as:

$$\epsilon^{src} = \frac{N_{full}^{src}}{N_{inci}^{src}} = \frac{N_{full}^{sim} + N_{full}^{bk}}{N_{inci}^{sim} + N_{inci}^{bk}}, \tag{5.13}$$

calculated from simulated and background data, denoted with *sim* and *bk* respectively. By means of the difference:

$$\Delta\epsilon = \frac{N_{full}^{src}}{N_{inci}^{src}} - \frac{N_{full}^{sim} + N_{full}^{bk}}{N_{inci}^{sim} + N_{inci}^{bk}}, \tag{5.14}$$

the systematic uncertainty of the efficiencies from the simulations can be estimated.

In figure 5.13, coincident single-cluster energies from the ^{60}Co source run are shown. Transitions around $E(\gamma_2) = 1.173$ MeV were utilised to define N_{inci} and the scaling of the simulation and background events for coincident entries around $E(\gamma_1) = 1.333$ MeV by means of a fit. The proximity of the γ transition-energies in the ^{60}Co beta-decay with respect to the XB energy resolution requires a careful definition of the energy intervals around the respective full-energy depositions. In this work intervals of

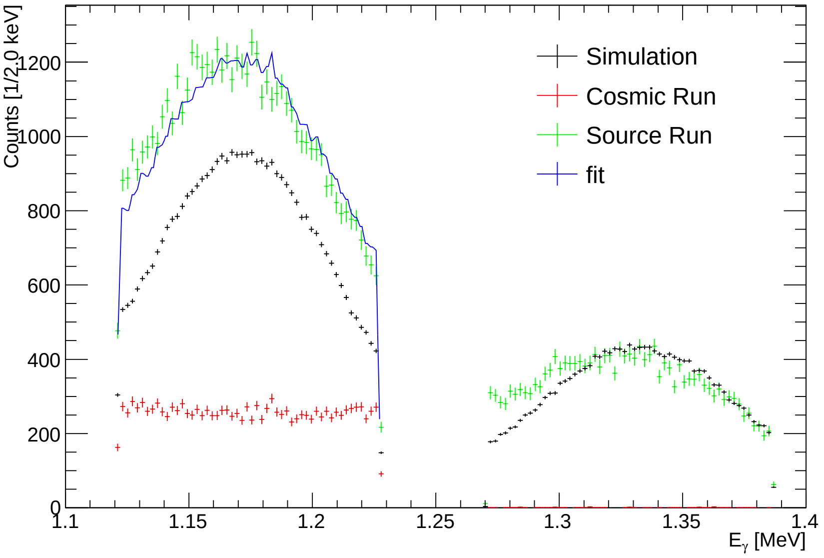

Figure 5.13.: Coincident gammas from the ^{60}Co source where N_{inci} was obtained from the lower transition energy of 1.173 MeV. The fit of the source run with the simulation and cosmic run yields their scaling for coincident entries around $E(\gamma_1) = 1.333$ MeV.

1σ inferred from a Gaussian fit around the peak were chosen in order to void overlap. Furthermore, exactly one event per energy interval was required in order to suppress random coincidences. Despite this, no multiplicity cut on energy clusters has been used. Finally, the systematic uncertainty of the integral efficiencies of $\Delta\epsilon(1.173\,\mathrm{MeV}) = 1.3\%$ and $\Delta\epsilon(1.333\,\mathrm{MeV}) = 4.3\%$ in the simulations was derived.

When gating on 1.333 MeV the fit systematically underestimates the source run, which was taken in a closed configuration of XB with respect to the target chamber. This information is missing for cosmic runs, which possibly were taken in open XB configuration. Hence, background radiation in the source run may not be represented reliably by the cosmic run. The ^{40}K decay is a significant background component and its characteristic decay radiation of 1.461 MeV exceeds to the gate on 1.333 MeV energies as can be seen in figure 5.12. When the ^{40}K background component is not defined reliably in this energy region the observed systematic deviation may result.

5.4.2 Response Function for De-excitation Spectra of Fragments

In Coulomb breakup events with gamma emission occur when excited states of the fragment are populated. The de-excitation gammas were simulated in XB, based on the level scheme of the fragment. From the simulated detector response f_j accounting for experimental background f_{bk} a response function:

$$f_{resp} = \sum^{tr} c_j f_j + c_{bk} f_{bk}, \tag{5.15}$$

was constructed and fit to experimental data. The sum runs over all transitions *tr* and the c_j and c_{bk} denote the respective fit parameters. The experimental background contribution was derived from the XB response to unreacted beam, that has been identified in the fragment mass spectrum, figure 5.5. Background is attributed to Bremsstrahlung of beam particles crossing the target. The fraction of simulated de-excitations in XB is named branching br_i in this work:

$$br_i = \frac{c_i f_i}{\sum^{tr} c_j f_j + c_{bk} f_{bk}}. \tag{5.16}$$

When the Coulomb-dissociation interaction probability p_{CD}, equation (5.7), is known for events with XB trigger the probability for transitions to excited states i can be corrected by the XB efficiency ϵ_i according to:

$$p^i_{CD} = (br_i \cdot p_{CD})/\epsilon_i. \tag{5.17}$$

The efficiency ϵ_i is the ratio of observed transitions and the number of simulated events. In this work 50,000 gammas were initiated in the simulations. From the reconstruction of the ^{60}Co source run by means of simulations the integrated uncertainty of the simulated XB efficiency was estimated to be $\Delta\epsilon = 5\%$.

5.4.3 XB Response to the De-excitation of ^{16}C Fragments

The detector response to characteristic gammas emitted in the de-excitation of the excited states of the fragment was obtained from simulations with `R3BROOT`. The level scheme of ^{16}C is presented in figure 6.1. In the response function, equation (5.15), transitions from the first excited state to the ground state $2^+ \to 0^+$ as well as cascades [56] from higher states $(0^+) \to 2^+ \to 0^+$ and $4^+ \to 2^+ \to 0^+$ were taken into account. In the latter cascade the states around 4 MeV are summarised while the former accounts for a level at 3.02 MeV [56]. The gammas were initialised at the target z-position while (x, y)

were adapted to the measured transverse beam profile. Therefor positions distributions from DSSSD 2 were used to define a Gaussian and a smoothed-box distribution in x- and y-direction, respectively. The gammas have been initiated isotropically, but the longitudinal momentum component with respect to the z-direction was Doppler boosted. Hence, they appear as if emitted at beam velocity in the rest frame of the projectile. Therefor the central value of the incoming particle distribution $\beta = 0.747$ obtained from a fit by a Gaussian was used.

For the analysis presented here 158 detectors were utilised (see table 5.1). The subsequent treatment of the energy depositions in the single crystals in the simulations was carried out fully analogously to the considerations concerning the ^{60}Co source-run reconstruction described in detail in Section 5.4.1. This comprises the convolution of the energy entries with individual detector resolutions, the use of individual detector thresholds and the application of the cluster and Doppler-correction algorithm `addback`.

The efficiencies of the transitions refer to the entire simulated spectrum. They are namely $\epsilon(2^+) = 0.87$ for the direct transition and higher for the cascades $\epsilon(0^+) = 0.98$ and $\epsilon(4^+) = 0.98$. In the latter case two gammas are involved, which significantly increases the detection probability of the de-excitation process in XB.

For experimental data entries above the separation energy of the fragment taking into account the Doppler boost were disregarded. In case of ^{16}C with $S_n = 4.25$ MeV that's $S_n \cdot \sqrt{1+\beta}/\sqrt{1-\beta} \approx 10$ MeV for gammas in forward direction. Furthermore, time conditions were required in order to suppress background in XB from massive particles.

5.4.4 XB Response to the De-excitation of ^{17}C Fragments

By analogy with the analysis of ^{17}C Coulomb dissociation a response function, formula (5.15), was constructed for ^{17}C fragments. The level scheme of ^{17}C in shown in figure 6.4 and transitions $1/2^+ \rightarrow 3/2^+$ (gs.) and $5/2^+ \rightarrow 3/2^+$ (gs.) were simulated in `R3BRoot`. Again, gammas were emitted at the target position while accounting for the transverse beam-profile. The momentum component in beam direction was boosted according to the average velocity of the ^{18}C projectiles $\beta = 0.727$. Energy entries in the XB detectors were convoluted with the respective detector resolution, taking the corresponding threshold into consideration and the cluster and Doppler-correction algorithm `addback` was applied.

Regarding experimental data energy entries above 1.65 MeV were discarded, since they cannot be emitted in the de-excitation of the ^{17}C fragment. The threshold was calculated from the Doppler shift of the neutron separation-energy of ^{17}C for fragments in forward direction to $S_n \cdot \sqrt{1+\beta}/\sqrt{1-\beta}$. Furthermore, time conditions were required in order to suppress background in XB from massive particles.

In this analysis exclusively energy entries in forward direction, *i.e.* with polar angle $\theta \leq 90°$, were used for background reduction in XB. For this purpose, crystals of XB were attributed so-called rings, which are listed in table A.1, each covering around 13° at a certain polar angle. As can be seen the efficiencies are reduced by 6% and 12% for $1/2^+$ and $5/2^+$ transitions, respectively, when gating on the forward direction. However, this was taken into account in the respective efficiency corrections.

When energy entries in backward direction are discarded events beyond 0.5 MeV in the XB energy spectrum were effectively suppressed. In this energy region solely the tail of the atomic background, which has crucial influence on the spectrum around the peaks from de-excitation gammas, contributes. For comparison the single and sum-energy spectra from all XB crystals are shown in figure A.5 and figure A.6, respectively.

5.4.5 LAND Efficiency Correction

For the definition of the Coulomb-dissociation reaction channel the detection of the neutron is essential. The LAND efficiency ϵ_{LAND} was obtained from simulations utilising the `LAND event generator` (LEG) fully carried out by D. Rossi. Based on the software ϵ_{LAND} dependent on the kinetic energy of the neutron T_n can be written as [57]:

$$\epsilon_{LAND}(T_n) = \epsilon_{nom}(T_n) \cdot \epsilon_{det}(T_n) \cdot a_{det}(T_n), \tag{5.18}$$

where $\epsilon_{nom}(T_n)$ is the nominal LAND efficiency, which was measured in a calibration experiment [58]. The term $\epsilon_{det}(T_n)$ accounts for the actual detector performance, that takes into account inactive paddles (see table 3.2). The acceptance $a_{det}(T_n)$ covers the fraction of neutrons that pass LAND dependent on their momentum relative to the normal direction on the neutron detector.

The LAND efficiency for ^{18}C at 426 AMeV is presented in figure 5.14 with respect to the relative energy

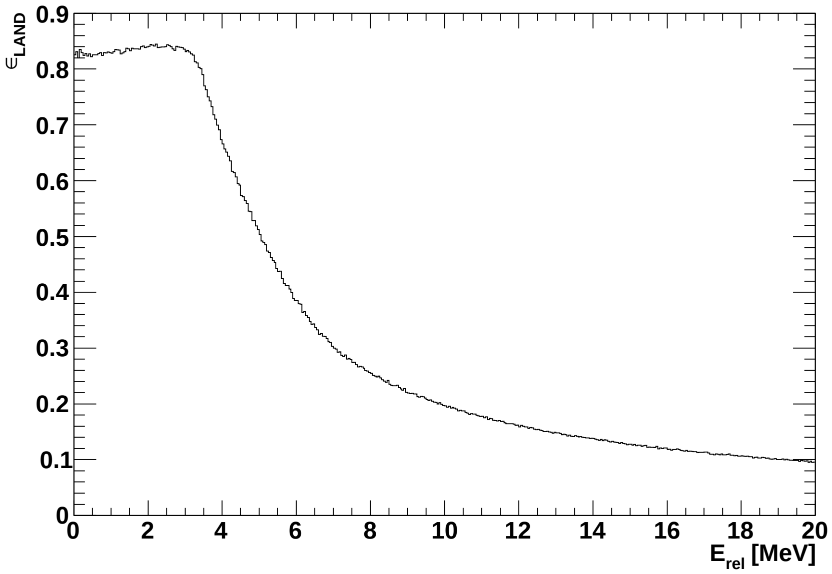

Figure 5.14.: LAND efficiency with respect to the relative energy in the neutron-fragment system. Data was provided by D. Rossi.

E_{rel} in the neutron-fragment system. The momenta of the neutron n and the fragment fr write as:

$$\vec{p}_n = \vec{p}_{fr}. \tag{5.19}$$

E_{rel} relates to the neutron kinetic energy as:

$$E_{rel} = T_n + T_{fr} = T_n \cdot \frac{m_n}{\mu_{(n,fr)}}. \tag{5.20}$$

Here, $T = mv^2/2$ and momentum conservation (5.19) was used for the deduction of the second relation. The reduced mass of the neutron-fragment system is $\mu_{(n,fr)} = m_n m_{fr}/(m_n + m_{fr})$. In figure 5.14 the one-neutron removal channel is shown. In the LEG simulations up to three neutrons have been reconstructed in the neutron volume-algorithm [43]. The plateau of the efficiency distribution up to $E \approx 3$ MeV is dominated by ϵ_{nom} with minor modifications caused by ϵ_{det}. With increasing neutron energy an increasing number of neutrons pass LAND, which limits the acceptance of the neutron detector and reflects in an approximately exponential decline of the LAND efficiency.

5.5 Invariant Mass

For the calculation of the energy-differential Coulomb-dissociation cross section according to equation (2.12) the energy ϵ transferred by the virtual photon is required. Since ϵ is not accessible directly, it has to be reconstructed from ToF, position and energy-loss measurements with the experimental setup. From the complete kinematic determination of all particles of the reaction the invariant mass S of each event was derived. S is preserved in the Lorentz transformation between the laboratory system (*lab*) and the rest frame of the ion (*cms*) and links measured quantities in the *lab* to the excitation energy ϵ in the *cms*. In special relativity the invariant mass can be expressed by means of the four-momentum $P^{\mu} = (E, \vec{p})$:

$$S = \eta_{\mu\nu} P^{\mu} P^{\nu} = E^2 - \vec{p}^{\,2}. \tag{5.21}$$

Here, $\eta_{\mu\nu} = \mathrm{diag}(1, -1, -1, -1)$ is the Minkowski metric and for the speed of light $c = 1$ holds. The invariant masses S_{cms} and S_{lab} can then be written as:

$$S_{cms}^2 = (m_{proj} + \epsilon - E_{\gamma})^2, \tag{5.22}$$

$$S_{lab}^2 = \left(\sum_f E_f \right)^2 - \left(\sum_f \vec{p}_f \right)^2, \tag{5.23}$$

where the sums run over all outgoing particles f. The excitation energy is ϵ and E_{γ} denotes the level energy of the final state of the fragment identified by the gamma-energy in the XB spectrum. Note that in (5.22) the recoil from the virtual photon is neglected, since the excitation energies in the equivalent-photon field are small compared to the projectile mass m_{proj}. Utilising $m^2 = E^2 - \vec{p}^{\,2}$, $E = \gamma m$ and $\vec{p} = \gamma \vec{\beta} m$, (5.22) and (5.23) can be rearranged for the case that the excited system decays into a fragment (*fr*) and a neutron (n):

$$\epsilon = \sqrt{m_{fr}^2 + m_n^2 + 2E_{fr}E_n \cdot (1 - \beta_{fr}\beta_n \cos(fr, n))} + E_{\gamma} - m_{proj}. \tag{5.24}$$

Where, $\cos(fr, n)$ is the angle between the fragment and neutron momenta. Making use of $\epsilon = E_{rel} + E_{\gamma} + S_n$ and $m_{proj} + S_n = m_{fr} + m_n$, S_n being the neutron separation energy of the projectile, the relative energy of the fragment and neutron is:

$$E_{rel} = \sqrt{m_{fr}^2 + m_n^2 + 2E_{fr}E_n \cdot (1 - \beta_{fr}\beta_n \cos(fr, n))} + m_{fr} - m_n. \tag{5.25}$$

Hence, the reconstruction of the relative energy relies on the unambiguous identification of all outgoing particles and the measurement of their momenta and rest masses.

5.6 DSSSD Alignment

In the S393 experimental campaign two pairs of DSSSDs were placed in front and behind the reaction target for the determination of the incoming and outgoing angle (see Fig 5.15) in order to derive the scattering angle of the fragment. Besides the internal resolution of the detectors the alignment with respect to each other, *i.e.* the conversion of internal positions (u, v, w) to Cartesian coordinates (x, y, z), has an influence on the angular resolution. In the following the alignment procedure will be illustrated. The general routine is explained in the first section and afterwards the fit routine is described in detail. Finally the results are discussed.

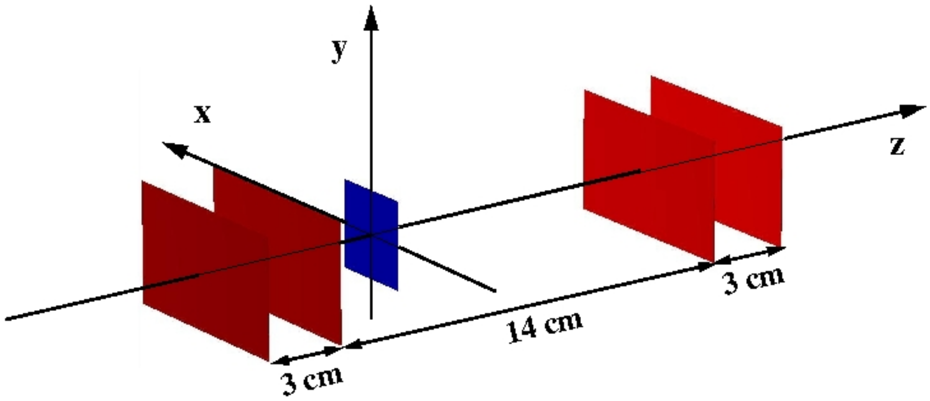

Figure 5.15.: Four in-beam DSSSD (red), grouped around the target (blue).

5.6.1 Alignment Routine

There are various ways to align tracking detectors. Most simple, for primary beam that is assumed to follow the optical axis most precisely the incoming angle is set to zero with suited detector offsets (x, y). Or simply residue with respect to a straight-line fit are interpreted as alignment offsets. However, these methods require that the systematical uncertainties are similar for different incoming angles and cancel out when angles are subtracted, which may not be necessarily fulfilled. Hence, these approaches provide local solutions suited for particle tracks close to those used for calibration. In case of deviations the angular resolution will get worse. And in the very end the extracted physical quantity is dependent on the angle of the incoming beam, *i.e.* beam characteristics. This understanding motivates a more complex approach, which includes a rotational degree of freedom and is subdivided as follows:

1. Determination of the detector positions using the photogrammetric method,
2. Three-parameter (x, y, γ) fit to an empty-target run for a suited subsystem of three detectors,
3. Alignment of the remaining detector.

A pre-alignment that turned out to be essential was done analysing photographs as described in chapter B. The target and tracking detectors were mounted on a copper ground plate in a compact configuration, which was fixed in the target chamber. For this moderately sized system a separate position measurement was performed. Therefor the (handy) construction was conveniently placed aside its position in the experiment. This setting was less limited in angular acceptance of the camera and a photo shooting with higher focal length was carried out. The obtained detector positions were implemented to the model of the entire experimental setup by means of four markers that form a rectangle. Those served as an interface, because they were accessible visually in the existing model and the (presently discribed) measurement with higher precision. For the position measurement in the target area an accuracy of 400 μm was obtained, far better than for the rest of the experimental setup.

Subsequently, simple straight-line fits for subsets of three detectors were performed. In table 5.2, the resulting residue are shown. They are smallest, if detector one, *i.e.* the first in the beam line, is omitted. Especially in y-direction the detectors then are well aligned, because the residue are smaller than the expected internal detector resolution in the order of 10 μm [59].

When in addition to offsets on (x, y) the rotation γ along the beam axis is treated as a fit parameter as described in the next section the residue on average get even smaller (see table 5.4). Note that the result was obtained without any prerequisite to a detector in x- or y-direction and is hence valid for any incoming angle. Finally, the detector positions omitting the first detector were corrected for the obtained fit residue. From this alignment a projection on the first detector was used to align this one as well.

	Residuum (μm)							
	x-direction				y-direction			
DSSSD	1	2	3	4	1	2	3	4
	–	-5.2	33.4	-28.1	–	0.0	0.3	-0.1
	-7.8	–	57.5	-49.7	0.4	–	-2.6	2.3
	-134.6	155.4	–	-21.2	14.4	-16.7	–	2.3
	-125.5	148.9	-23.5	–	13.8	-16.3	2.6	–

Table 5.2.: Residue of hit positions with respect to a simple straight-line fit using three detectors, where the skipped detector is indicated by " – ". The x- and y-direction are perpendicular to the z beam-direction.

5.6.2 Three-Parameter Fit of an Empty-Target Run

So far exclusively translational shifts in (x, y) of the detectors perpendicular to the beam z-direction were considered. The longitudinal offset is measured to be smaller than 400 μm by the photogrammetric method. Taking the distances between the tracking detectors into account this results in a per mill effect for an angular measurement and can be neglected.

In the following rotations of the detectors along the Cartesian axes will be discussed. Their influence can be illustrated when residue with respect to a straight-line fit are plotted *versus* hit positions on the detector, as presented in figure 5.16 for DSSSD 2 using internal coordinates (u, v, w). In the upper and middle panel the residue with respect to the u- and v-direction are plotted versus the positions in the same direction. The offsets Δu and Δv can be identified. A rotational offset of the detectors along the y- and x-axis, respectively, would reflect in a position dependency of the distributions. Despite fluctuations dominated by electronics effects no such trend can be found. Note that one half of DSSSD 1 was non-functional and effected particle tracks have been excluded from this analysis. In the lower panel the fit residue are plotted versus the orthogonal direction revealing the necessity for a correction of rotations along the beam axis. A clear trend of the residue distribution with respect to the hit position can be seen. These correction parameters were finally obtained in a two-dimensional variational iterative algorithm. Therefor the alignment procedure described in [60] has been adapted to the requirements of the presented experimental setup. Subsequently, major steps and the specification for the DSSSDs will be depicted.

A 3D straight line, *i.e.* particle track j, as parametrised in the `LAND02` (x, y, z)-coordinate system is:

$$x_j = a_{1j} + a_{3j} z, \tag{5.26}$$

$$y_j = a_{2j} + a_{4j} z, \tag{5.27}$$

where a_{kj} are the parameters of the line. Let the local detector system be denoted by (u, v, w). When the u-axis makes an angle γ with the x-axis the residue of detector i with respect to a straight line can be written as:

$$\epsilon_{ij} = u_i - \cos\gamma_i (a_{1j} + a_{3j} z_i) - \sin\gamma_i (a_{2j} + a_{4j} z_i). \tag{5.28}$$

Where, u_i are measured coordinates. The residue get smallest for proper shifts:

$$u_i \to u_i + \Delta u_i, \tag{5.29}$$

$$\gamma_i \to \gamma_i + \Delta\gamma_i, \tag{5.30}$$

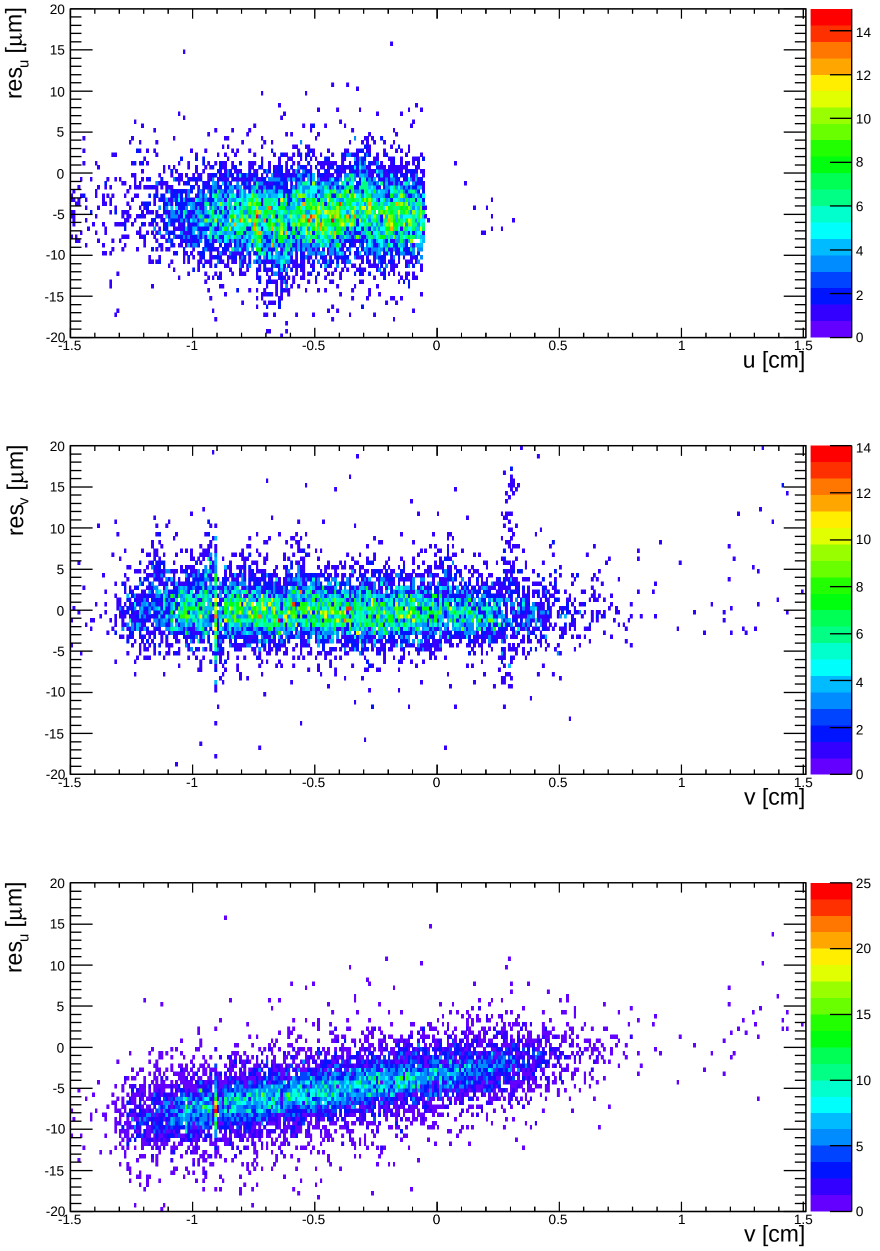

Figure 5.16.: Residue with respect to a straight-line fit versus the directions perpendicular to the beam axis. The internal coordinates (u, v) correspond to Cartesian coordinates (x, y) rotated by an angle γ around the beam z-axis.

which were calculated using the grand χ^2 expressed for all detectors i and tracks j:

$$\chi^2 = \sum_{i=1}^{4} \sum_{j=1}^{M} \omega_i \epsilon_{ij}^2. \tag{5.31}$$

Here, the ω_i are the weights of the detectors in the straight-line fit. Because the detectors are supposed to have similar position resolution, similar weights were attributed. For the presented alignment a linear least squares minimisation was utilised in order to obtain the residue ϵ_{ij} with respect to a straight line. The χ^2 function then is to be minimised iterative by the Newton method, that provides solutions for nonlinear equations. Then the problem separates in terms of detectors and the solutions can be expressed dealing with 2×2 matrices [60]:

$$\begin{pmatrix} \delta\Delta\gamma_i \\ \delta\Delta u_i \end{pmatrix} = \left[\sum_{j=1}^{M} \begin{pmatrix} \frac{\partial\epsilon_{ij}}{\partial\gamma_i}\frac{\partial\epsilon_{ij}}{\partial\gamma_i} & \frac{\partial\epsilon_{ij}}{\partial\gamma_i}\frac{\partial\epsilon_{ij}}{\partial u_i} \\ \frac{\partial\epsilon_{ij}}{\partial\gamma_i}\frac{\partial\epsilon_{ij}}{\partial u_i} & \frac{\partial\epsilon_{ij}}{\partial u_i}\frac{\partial\epsilon_{ij}}{\partial u_i} \end{pmatrix} \right]^{-1} \sum_{j=1}^{M} \begin{pmatrix} \epsilon_{ij}\frac{\partial\epsilon_{ij}}{\partial\gamma_i} \\ \epsilon_{ij}\frac{\partial\epsilon_{ij}}{\partial u_i} \end{pmatrix}. \tag{5.32}$$

The derivatives involved are:

$$\frac{\partial\epsilon_{ij}}{\partial\gamma_i} = \sin\gamma_i(a_{1j} + a_{3j}z_i) - \cos\gamma_i(a_{2j} + a_{4j}z_i), \tag{5.33}$$

$$\frac{\partial\epsilon_{ij}}{\partial u_i} = 1. \tag{5.34}$$

The corrections have to be subtracted. Afterwards, the minimisation starting from the calculation of the residue has to be repeated. However, for the presented alignment already one iteration was sufficient utilising 10000 particle tracks in the empty target run 454 with exactly one hit per detector. Therefor incoming carbon was used, since the DSSSD energy-loss calibration was performed for $Z = 6$.

The performance of the fitting routine is illustrated by means of the u-direction in the second detector in figure 5.17, before (left) and after (right) the first iteration. As can be seen an offset and a rotation

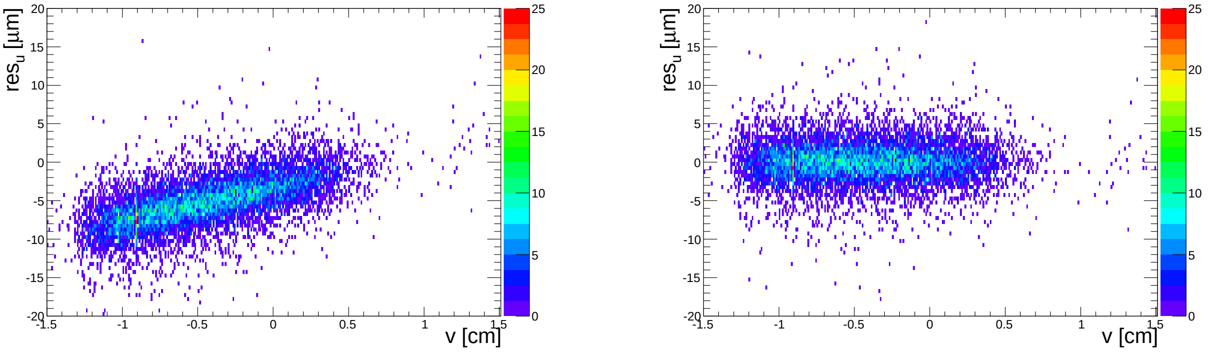

Figure 5.17.: Alignment of DSSSD 2 including the rotation along the beam axis in the fit. Data before alignment (left) is shifted and rotated (right).

obtained from equation (5.32) were applied. The residue, *i.e.* the projections on the y-axis in the plots, are shown in figure 5.18 before (solid line) and after (dashed line) the alignment. Those were

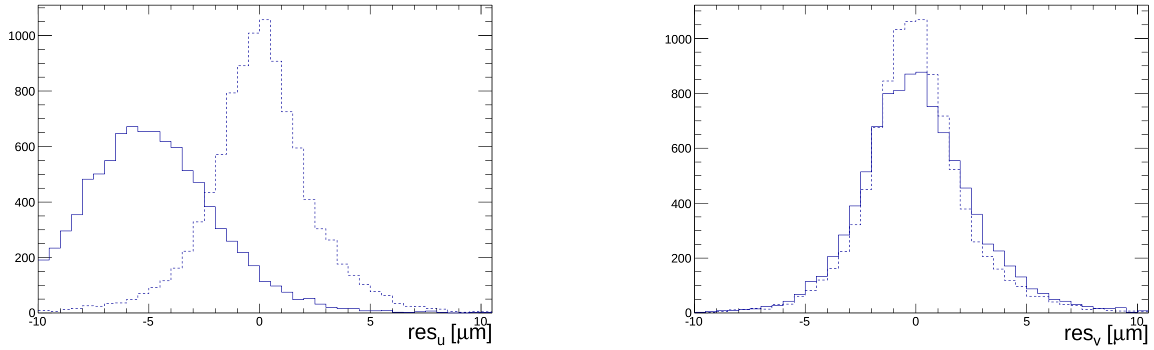

Figure 5.18.: Residue of DSSSD 2 with respect to a straight-line fit before (solid line) and after (dashed line) the alignment.

	Improvement							
	u-direction				v-direction			
DSSSD	1	2	3	4	1	2	3	4
	26%	30%	32%	28%	18%	17%	20%	17%

Table 5.3.: Residue with respect to a straight-line fit. The distributions were approximated by Gaussian and the improvement refers to the widths of the Gaussian before and after the detector alignment.

	Residuum (μm)							
	u-direction				v-direction			
DSSSD	1	2	3	4	1	2	3	4
Step 1	–	-3.3	18.0	-14.8	–	-2.0	12.9	-10.9
Step 2	-336.3	0.0	-0.2	0.2	62.6	-0.1	0.6	-0.5

Table 5.4.: Residue of the hit positions with respect to a straight-line fit. In step 1 the first DSSSD is omitted. It is aligned in step 2 while the other detectors hit-positions (u, v) were kept fix. The residue add up.

	Offset (μm)			
DSSSD	1	2	3	4
	x-direction			
Photos	224.4	-260.7	555.9	1284.3
Fit	336.4	3.3	-17.8	14.6
Abs	-112.252	-64.144	193.653	241.935
	y-direction			
Photos	326.2	141.0	-875.2	-606.6
Fit	-62.5	2.1	-13.4	11.4
Abs	-775.011	-442.863	1337.014	1670.365
	Rotation (mrad)			
	z-axis			
Fit	4.9	-0.4	2.4	-2.0

Table 5.5.: Offsets for the DSSSD alignment from the analysis of photogrammetric data (Photos), the fitting routine (Fit) and the alignment with respect to LAND (Abs). The offsets have to be added to (x, y) and afterwards detectors are to be rotated (right-handed system) into (u, v).

approximated by Gaussian whose σ's improve by 25% on average. The values for all detectors are listed in table 5.3.

As has been pointed out before residue of the three-detector fit get smallest, if DSSSD 1 is omitted. Hence, a two-step fit procedure was accomplished for the three-parameter fit. In table 5.4, the calculated corrections, which add up, are listed for both steps. For the alignment of the first detector the weights of the others were set extraordinarily high resulting in negligible corrections for those.

5.6.3 Results and Discussion

Solving equation (5.32) provides a rotational offset $\Delta\gamma$ and position offsets Δu or Δv. Hence, the alignment has to be performed separately for the u- and v-direction. The resulting γ offsets agree within $\Delta\gamma = 0.2$ mrad. In table 5.5, all offsets are summarised. The uncertainty of the alignment routine is considered to be dominated by the internal position resolution of the DSSSDs of around 10 μm [59].

Alignment with Respect to LAND

When the DSSSD are aligned relative to each other they can be directed towards LAND with neutrons emitted in Coulomb-breakup reactions. Since the target position and the centre of LAND are known to sufficiently precisely follow the ion-optical axis in (x, y), this procedure is referred absolute alignment. Neutrons from Coulomb breakup are evaporated isotropically in the rest frame of the projectile. Hence, their position distribution is directly linked to the incoming-beam direction and the deviation of the projection of the incoming beam on LAND from the neutron position-distribution, presented figure 5.19, yields the alignment parameters. On the left and right side in the picture the x- and y-position distributions, respectively, are shown. The neutron and projectile distributions have been extracted from incoming ^{18}C projectiles in a lead-target run and accordingly in an empty-target run. Coulomb-breakup events were characterised according to the procedure in Section 5.1.2 while the conditions as for the DSSSD fit procedure (Section 5.6.2) were applied for the projection of the projectile direction performed with DSSSD 2 and 3. Note that the projectile direction was extrapolated to the first plane while neutrons along the entire depth of LAND were allowed. The mean values of the distributions, summarised in

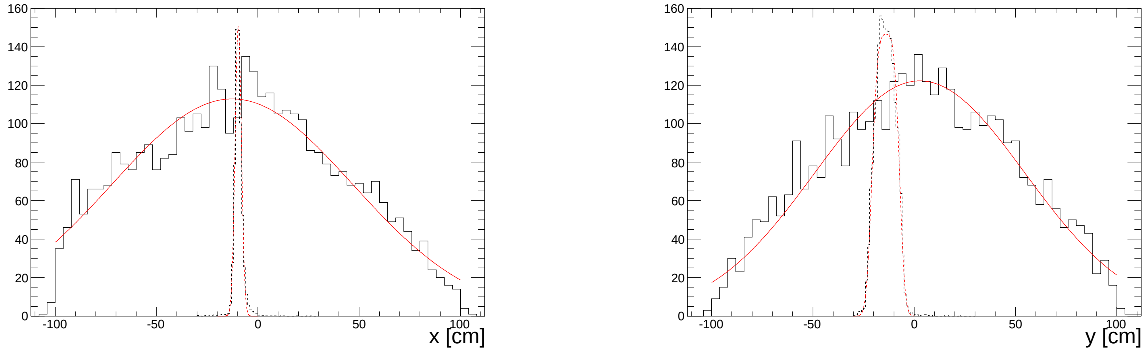

Figure 5.19.: Position distributions of neutrons (black solid line) and projections on ^{18}C projectiles (black dashed line) on LAND. The according fits are shown in red.

table 5.6, were derived from fits with a Gaussian (x-direction) or a smooth-box function (y-direction).

Mean Position [cm]			
x-direction		y-direction	
n	$proj$	n	$proj$
-1 ± 1	-9.67 ± 0.07	3 ± 1	-14 ± 4

Table 5.6.: Mean values of the position distributions of neutrons and ^{18}C projectile projections on LAND. Data were extracted from the fit functions in figure 5.19.

Significant deviations were found revealing a miss-alignment of the entire system of the DSSSDs, *i.e.* the target ground plate, with respect to the incoming optical axis. Probably the target chamber fitting very rigid mechanical constraints between the upstream beam line and the ALADiN adapter was slightly distorted, already. An offset is rather unlikely, since the position of the target and LAND are sufficiently precisely known. Thus, the correction was carried out by means of rotations in (x, y) reflecting in offsets as given in table 5.5 for each tracking detector.

Multiple Coulomb Scattering

The scattering angle at the target is the difference of the incoming and outgoing angle $\theta_{sca} = \theta_{1/2} - \theta_{3/4}$ obtained from position measurements in DSSSD 1/2 and DSSSD 3/4, respectively. In case no reaction was detected by the experimental setup the distribution θ_{sca} is defined by the intrinsic position resolution of the tracking detectors and multiple Coulomb scattering (straggling) in material. In figure 5.20, a particle trajectory through the tracking system (blue) and the target (red) is sketched. Due to straggling a piecewise linear-curve results. As can be seen for the outgoing angle holds:

$$\theta_{3/4} = \theta_{1/2} + \theta_{str}^{(2)} + \theta_{str}^{(tar)} + \theta_{str}^{(3)}, \tag{5.35}$$

where the straggling (*str*) of DSSSD 2 and 3, and the target (*tar*) have to be taken into account. The scattering angle can then be written as:

$$\theta_{sca} = \theta_{str}^{(2)} + \theta_{str}^{(tar)} + \theta_{str}^{(3)}. \tag{5.36}$$

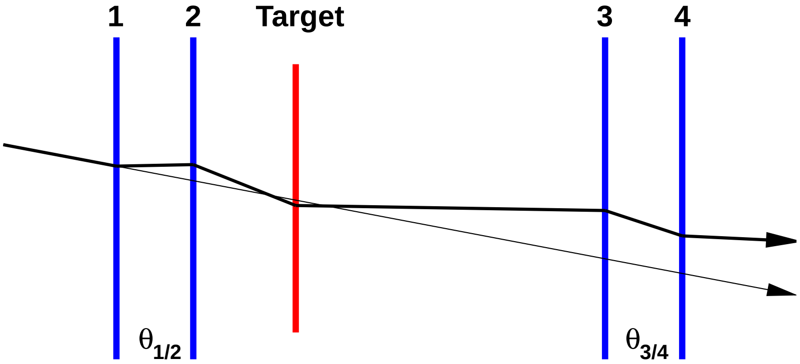

Figure 5.20.: The DSSSDs are illustrated in blue. The incoming ($\theta_{1/2}$) and outgoing angle ($\theta_{3/4}$) of a particle track (thick line) around the target (red) are also shown.

The uncertainty of the measurement is:

$$\sigma_{sca}^2 = \left(\sigma_{str}^{(2)}\right)^2 + \left(\sigma_{str}^{(tar)}\right)^2 + \left(\sigma_{str}^{(3)}\right)^2. \tag{5.37}$$

Therefore, the straggling in the target can be calculated when the scattering-angle uncertainty of an empty-target run (mt) is subtracted:

$$\sigma_{str}^{(tar)} = \sqrt{\sigma_{sca}^2(tar) - \sigma_{sca}^2(mt)}. \tag{5.38}$$

In table 5.7, the straggling in terms of σ for 426 AMeV ^{18}C beam on Pb-, C- and CH$_2$-target, and for 461 AMeV ^{14}C beam on Ti-target are summarised. Since the tracking detectors provide positions in both directions, experimental values in (x, y)-direction are given. The positions at the target was chosen such that the beam doesn't hit the target frame. The data of the DSSSDs have been treated as described in Section 5.6.2 for unambiguous track identification. The theoretical values were obtained from the ATIMA simulation package [62]. Note that the straggling in the DSSSDs for the projectiles under discussion is around 0.2 mrad [63]. This value was provided by S. Paschalis and was exaggerated in figure 5.20 for demonstration purpose.

	$\sigma_{str}^{(tar)}$ [mrad]			
target [mg/cm^2]	Pb [2145]	C [935]	CH$_2$ [922]	Ti [394]
x	3.72 ± 0.07	0.99 ± 0.11	0.83 ± 0.13	1.18 ± 0.06
y	3.70 ± 0.06	0.90 ± 0.08	0.86 ± 0.09	1.13 ± 0.05
ATIMA	3.81	0.97	0.97	1.23

Table 5.7.: Experimental values in (x, y)-direction for the straggling $\sigma_{str}^{(tar)}$ compared to theoretical calculations (ATIMA) with an uncertainty of 10% [61].

Intrinsic Position Resolution

The scattering angle in a DSSSD can be calculated as:

$$\theta_{sca} = \theta_{2/3} - \theta_{1/2}, \tag{5.39}$$

utilising positions from just three DSSSDs in an empty-target run. In this case the straggling in the sandwiched detector is directly obtained, since:

$$\theta_{2/3} = \theta_{1/2} + \theta_{str}^{(2)}. \tag{5.40}$$

Equation (5.39) can then rewritten employing basic geometrical considerations:

$$\theta_{sca} = \tan\frac{x_3 - x_2}{z_3 - z_2} - \tan\frac{x_2 - x_1}{z_2 - z_1} \approx \frac{x_3 - x_2}{z_3 - z_2} - \frac{x_2 - x_1}{z_2 - z_1}, \tag{5.41}$$

and accordingly for the y-direction. The approximation of the tangent is justified by the acceptance of the beam line of ±10 mrad for incoming angles. The scattering angle expresses the straggling distribution, which is measured with a given position resolution. The uncertainty of the scattering angle is calculated from propagation of errors with a common intrinsic position-resolution $\sigma_x = \sigma_x^{(1)} = \sigma_x^{(2)} = \sigma_x^{(3)}$ as:

$$\sigma_{sca} = \sigma_x \cdot \sqrt{\left(\frac{1}{z_2 - z_1}\right)^2 + \left(\frac{1}{z_2 - z_1} - \frac{1}{z_3 - z_2}\right)^2 + \left(\frac{1}{z_3 - z_2}\right)^2}. \tag{5.42}$$

From equation (5.40) follows that no additional material is allowed between the detectors. Hence, there are two combinations in order to calculate θ_{sca} with four DSSSDs each time skipping one of the outmost DSSSDs. In table 5.8, the intrinsic position resolution for the (x, y)-direction calculated according to equation (5.42) with $\sigma_{str} = 0.2$ mrad [63] is listed. In addition, the results from a calibration experiment with 1.5 AGeV ^{12}C beam [59] are given. The values obtained in this analysis are worse, which may be caused by non-functional strips of the DSSSDs, deficits in the readout or the position calibration or the cluster finding procedure (see Section 3.2).

	$\sigma[\mu\text{m}]$		
DSSSD	1/2/3	2/3/4	[59]
x	16.2 ± 0.4	14.3 ± 0.3	14
y	14.6 ± 0.2	12.3 ± 0.3	8

Table 5.8.: Intrinsic position resolution of the DSSSDs from experimental data in comparison to Alpat *et al.* [59].

6 Results

Within the carbon chain various neutron halos have been identified [64, 65]. Also ^{17}C triggered such interest and was found to be a “hindered halo” in a d-wave ground state configuration [66]. In the experimental campaign presented here substantial amount of ^{17}C was contained in the incoming secondary beam. Hence, the analysis of Coulomb dissociation of ^{18}C was calibrated by comparison of ^{17}C results to an earlier publication of Coulomb breakup of ^{17}C by Pramanik *et al.* [12] done at comparable beam energy and utilising basically the same experimental equipment.

6.1 Coulomb Dissociation of ^{17}C

In the following the de-excitation γ-spectrum of the fragment and deduced integral partial cross sections as well as differential cross sections will be presented. The latter are furthermore compared to theoretical calculations in an independent-particle model [20]. Finally, experimental spectroscopic factors are extracted and compared to results from a knockout experiment by Maddalena *et al.* [67] and the Coulomb-dissociation experiment by Pramanik *et al.* [12] with ^{17}C nuclei.

6.1.1 Nuclear Structure

The neutron separation-energy of ^{17}C is 0.73 MeV and the half life was measured to be around 200 ms [68]. The level scheme is shown in figure 6.4 [69] identifying low-lying $5/2^+$ (0.33 MeV) and $1/2^+$ (0.22 MeV) excited states and the $3/2^+$ ground state. Extensive experimental spectroscopic information was obtained from the investigation of single-neutron knockout of ^{17}C on a ^{9}Be target at a beam energy of around 60 AMeV by Maddalena *et al.* [67]. That exclusive measurement was based on the level scheme of ^{16}C fragments sketched in figure 6.1. The single-detector Doppler corrected γ-ray spectrum

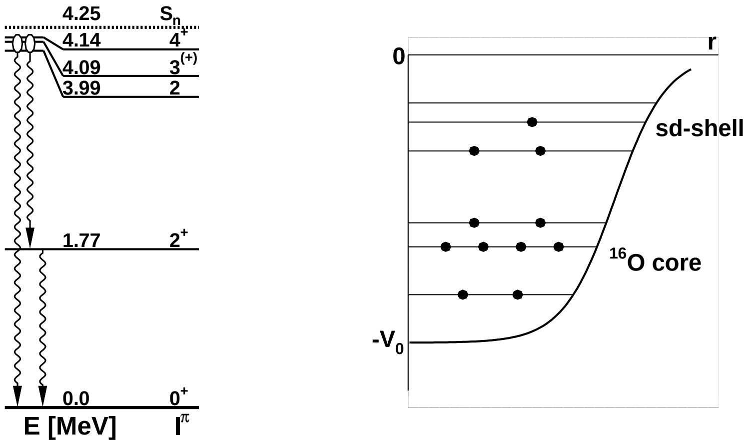

Figure 6.1.: (Left) Level scheme of ^{16}C [70] as used for the analysis in [67]. (Right) Neutron population of ^{17}C in a naive shell-model. The sd-shell comprises the $0d_{5/2}$, $1s_{1/2}$ and $0d_{3/2}$ levels.

exhibits a lower sensitivity to high-lying states. Those likely decay *via* a cascade through the first excited state of ^{16}C, which therefore appears very prominent in the spectrum. Since a larger number of excited states was found [56] and also added to evaluated data [68], in the analysis presented here a tentatively 0^+ excited state of ^{16}C at 3.02 MeV was also taken into consideration.

A deformation of ^{17}C was found in systematic studies of the entire carbon chain based on Relativistic Mean-Field (RMF) [71] and Shell Model (SM) calculations [72]. Maddalena *et al.* employed SM calculations for nuclear-structure studies particularly considering pairing and deformation effects [73, 74]. It was concluded that the ^{17}C ground state sd-shell occupation is dominated by a 32% $(0d_{5/2})^3$ and 31% $(0d_{5/2})^2(1s_{1/2})^1$ neutron configuration. The RMF calculation [71] yields 40% for the latter. Other contributions are not directly comparable, since the splitting of the Nilsson orbitals is not given in [67]. In that analysis in particular a fit of partial-wave contributions to the exclusive longitudinal momentum distributions was performed. It resulted in 8% s- and 92% d-wave for the states around 4 MeV, 26% s- and 74% d-wave for the first excited state and pure d-wave contributions for the ground state. In addition, Pramanik *et al.* identified $^{16}\mathrm{C}(2^+) \otimes \nu_{s,d}$ as the dominant ground-state configuration of ^{17}C.

6.1.2 Integral Cross Sections

The one-neutron removal channel was identified as described in Section 5.1, background components were subtracted (see Section 5.3) and the LAND efficiency correction was carried out according to Section 5.4.5. The obtained integral total Coulomb-dissociation cross section of the one-neutron evaporation channel is given in table 6.1 in comparison to the results from Pramanik *et al.* [12]. They are in agreement when a comparable uncertainty is assumed for the earlier publication, which did not specify the error of the total cross section.

Exclusive cross sections were derived utilising the γ-detector and in figure 6.2 the experimental γ-sum spectrum is presented. The response function is described in detail in Section 5.4.3 and contains simulations of fragment de-excitations and a background contribution. The latter is dominating the spectrum below 1 MeV and was extracted from the response of the γ-detector when non-reacted fragments were chosen in the fragment-mass spectrum. This component of the spectrum is attributed to Bremsstrahlung in the target. The response function reproduces the main features of the experimental spectrum revealing the fragment's excited states. The efficiency ϵ_i for the detection of certain de-excitation gammas were taken from Section 5.4.3 and partial cross sections were derived from equation (5.17). They are listed in table 6.1 along with the branching ratios, *i.e.* the portion of a certain transition, and compared to Pramanik *et al.* [12]. The cross sections show overall agreement while the present analysis tends to bigger contributions from excited states. Most of the reactions populate the first excited 2^+ state and both experiments are consistent with the scenario that the ground state is not populated at all. This

	Cross Section [mb]		Branching Ratio [%]	
	This Work	Comparison [12]	This Work	Comparison [12]
total	118 ± 15	96		
$I^\pi(E$ [MeV])				
0^+ (0.0)	6^{+19}_{-6}	9^{+15}_{-9}	5^{+16}_{-5}	9^{+16}_{-9}
2^+ (1.77)	70 ± 7	62 ± 7	60 ± 10	65 ± 7
(0^+) (3.0)	21 ± 3		18 ± 4	
4^+ (≈ 4.0)	21 ± 3	25 ± 7	18 ± 4	26 ± 7

Table 6.1.: Total and partial integral cross sections in comparison to the analysis of Pramanik *et al.* [12]. The Branching Ratio is given, too. It was calculated from the cross sections also for the earlier publication.

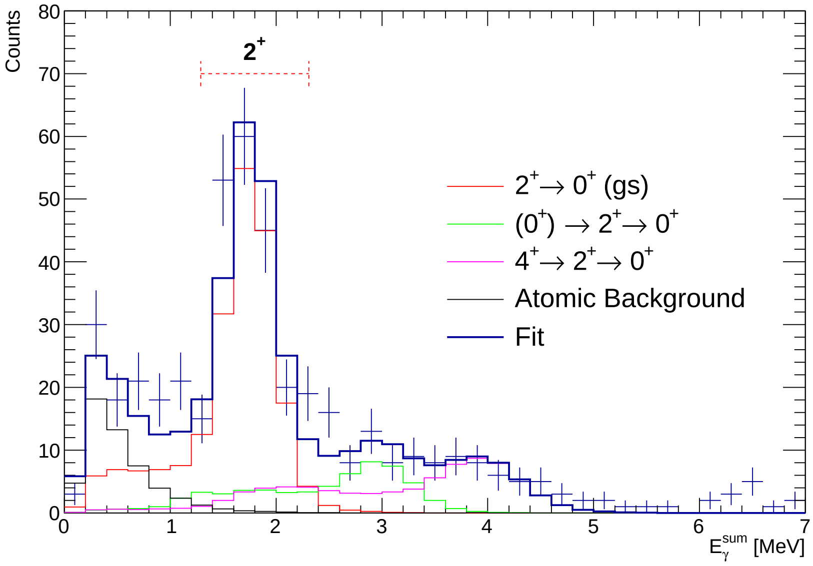

Figure 6.2.: Fit of the response function composed of simulations of de-excitations of excited states in ^{16}C to the γ-spectrum for ^{17}C at 470 AMeV impinging on lead target. Additionally, atomic background from the target extracted from non-reacted beam is used for the description of the spectrum below 1 MeV. The gate required to identify transitions $^{17}\text{C} \rightarrow ^{16}\text{C}(2^+)$+n is indicated.

suggests a neutron configuration of ^{17}C where a valence nucleon is coupled to the first excited state of ^{16}C (see relation (6.1)).

6.1.3 Differential Cross Section for ^{17}C→ ^{16}C(2$^+$)+n

Transitions to the first excited 2^+ state were identified in the γ-sum spectrum in figure 6.2 by means of the indicated gate around $E_\gamma^{\mathrm{sum}} = 1.77$ MeV. Since energy entries may also stem from the de-excitation of higher-lying states, an additional systematic uncertainty of around 15% is introduced. It adds up to the binned statistical error of all events identified as ^{17}C→ ^{16}C(2$^+$)+n transitions. Therefore, it was attributed to the theoretical calculations. The efficiency corrected excitation-energy spectrum is shown in figure 6.3. A fit to theoretical Coulomb-dissociation cross sections from calculations in distorted-wave approximation was performed. The theoretical calculations are based on the CDXS+ code [20] depicted in Section 2.2.1.

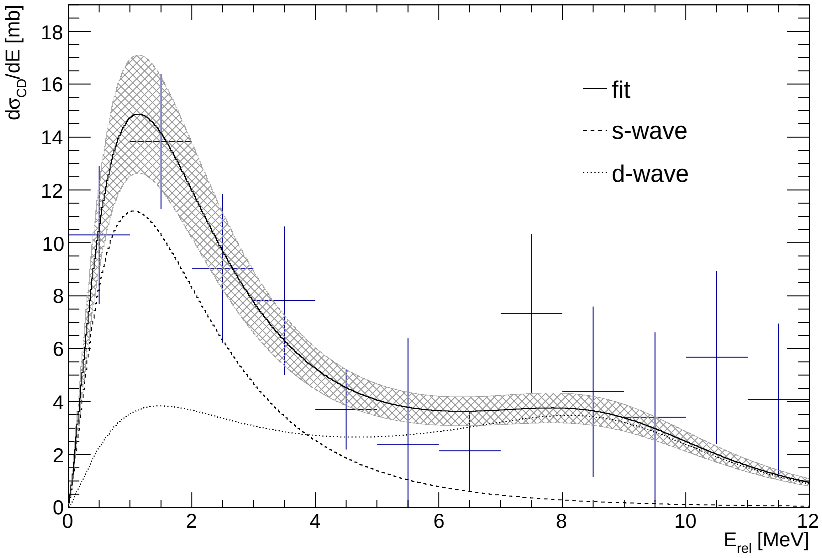

Figure 6.3.: Differential Coulomb-breakup cross section with respect to the relative energy E_{rel} in coincidence with the 1.77 MeV de-excitation γ. A fit to theoretical calculations in distorted-wave approximation with contributions from sd-shell neutrons was carried out.

Experimental half lives of bound states in ^{17}C are not available and no isomeric states are known or indicated by theory. Hence, it is reasonable to assume those half lives in the range of picoseconds and the ^{17}C beam is taken in the $3/2^+$ ground state. It was decomposed into a ^{16}C core and a valence neutron in the theoretical calculations. The spins of the core j_c and the neutron j_n can couple like $|j_c - j_n| \ldots |j_c + j_n|$ to the spin of the ^{17}C projectile. According to table 6.1 most of the Coulomb-dissociation reactions populate the first excited state and the ground state may not be populated at all. When the sd-shell is taken as the valence space (see figure 6.1) and just the first excited state of ^{16}C is used ^{17}C can be decomposed as:

$$^{17}\mathrm{C}(3/2^+) \longleftrightarrow \left(^{16}\mathrm{C}(2^+) \otimes \nu 0d_{5/2}\right) \oplus \left(^{16}\mathrm{C}(2^+) \otimes \nu 1s_{1/2}\right) \oplus \left(^{16}\mathrm{C}(2^+) \otimes \nu 0d_{3/2}\right). \tag{6.1}$$

In this picture, the Coulomb breakup of ^{17}C takes place *via* emission of s- or d-shell neutrons. Those have positive parity and populate the negative parity $J = 3/2^-$, $1/2^-$ and $5/2^-$ levels in the continuum assuming an electric dipole transition $E1$ (see Section 2.2.1). These states can be populated by neutron capture on $0p_{3/2}$, $0p_{1/2}$, $0f_{7/2}$ and $0f_{5/2}$ levels of the fragment, amongst higher lying states. Interactions of proton states were not taken into consideration.

As can be seen in figure 6.3 the theoretical calculations describe experimental data very well as a composition of s- and d-wave neutron excitations. The width of the main peak is reproduced and the small bump at around 8 MeV results from final-state interactions in the excitation of d-wave neutrons. The weights of the fit yield (47 ± 11)% s-wave and (52 ± 17)% d-wave contribution. The Coulomb-breakup experiment [12] obtained (38 ± 22)% s-wave and (62 ± 23)% d-wave contribution. When similar uncertainties are assumed this is also in agreement with the analysis performed by Maddalena *et al.* [67], which obtained 26% s-wave and 74% d-wave contribution.

The experimental cross sections σ_{exp} for Coulomb dissociation of s- and d-wave neutrons were calculated from the fraction in the fit function in figure 6.3. Dividing the results by the respective theoretical single-particle cross sections σ_{sp} from the independent-particle model [20] the experimental spectroscopic factors C^2S were obtained. The results from single-neutron knockout of ^{17}C and the Coulomb-breakup experiments are summarised in table 6.2. They show overall agreement. Note that the present analysis tends to smaller spectroscopic factors of the d-wave contribution than the knockout experiment. This may reveal a lower sensitivity of the experimental technique to the corresponding neutron wave-functions.

E [MeV]	I^π	l	σ_{sp} [mb]	σ_{exp} [mb]	C^2S		
					This Work	Knockout [67]	Coulex [12]
Distorted-Wave Approximation							
1.77	2^+	0	158	32 ± 8	0.20 ± 0.05	0.21 ± 0.09	0.26 ± 0.14
		2	52	35 ± 12	0.67 ± 0.23	1.19 ± 0.30	1.60 ± 0.60
Plane-Wave Approximation							
1.77	2^+	0	166	35 ± 12	0.21 ± 0.07		0.23 ± 0.08
		2	49	26 ± 16	0.53 ± 0.33		0.60 ± 0.40

Table 6.2.: Single-particle cross sections σ_{sp} [20] and experimental spectroscopic factors C^2S for s- and d-wave contributions to the $^{17}\text{C} \rightarrow {}^{16}\text{C}(2^+) + \text{n}$ reaction in comparison to results from single-neutron knockout by Maddalena [67] and Coulomb dissociation by Pramanik [12].

6.2 Coulomb Dissociation of ^{18}C

Experimental spectroscopic factors C^2S of one-neutron removal reactions of ^{18}C are available from a publication by Kondo *et al.* [75]. In that experiment ^{18}C beam at 81 AMeV was directed onto a liquid hydrogen target and exclusive cross sections were extracted. These C^2S are compared to those from the present analysis of Coulomb dissociation of ^{18}C. Here, partial cross sections were derived from the γ-detector energy spectrum. Theoretical calculations [20] are compared to experimental energy-differential exclusive Coulomb-dissociation spectra. Subsequently, photoabsorption cross sections are calculated and neutron-capture cross sections are presented. Finally, reaction rates are shown.

6.2.1 Nuclear Structure

The neutron separation-energy of ^{18}C is 4.18 MeV and the half life was measured to be 92 ms [76]. Information about the level scheme is still ambiguous depending on the experimental approach [75, 77]. In figure 6.4, the spin-parity assignments to excited states from γ-ray spectroscopy [77] are summarised, which are in perfect agreement with shell-model calculations along the entire carbon chain [72]. However, Kondo *et al.* [75] propose the configuration of the sd-shell neutrons of ^{18}C as $(\nu 0d_{5/2})^4$ or $(\nu 0d_{5/2})^2(\nu 1s_{1/2})^2$, which supports that most neutron-removal reactions populate excited states.

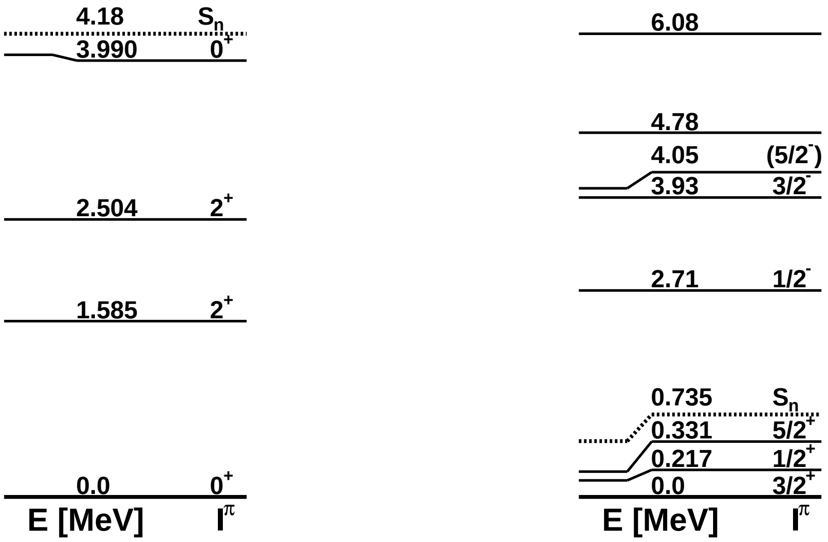

Figure 6.4.: Level schemes of (Left) ^{18}C [77] and (Right) ^{17}C [69].

6.2.2 Coulomb-Dissociation Cross Sections

The ^{18}C nucleus was considered as a composition of a ^{17}C core and a valence sd-shell neutron in this analysis. Due to spin coupling described in detail for the ^{17}C case the ground state of the projectile can be written as:

$$^{18}\mathrm{C}(0^+) \longleftrightarrow \left(^{17}\mathrm{C}(3/2^+) \otimes \nu 0d_{3/2}\right) \oplus \left(^{17}\mathrm{C}(1/2^+) \otimes \nu 1s_{1/2}\right) \oplus \left(^{17}\mathrm{C}(5/2^+) \otimes \nu 0d_{5/2}\right). \tag{6.2}$$

In this picture the $3/2^+$ ground state of ^{17}C and the excited states were used. Proton wave-functions were not taken into account. As a conclusion from (6.2) each fragment state can unambiguously be assigned to a neutron wave-function from the sd-shell. Hence, single-particle cross sections from theoretical calculations are directly linked to exclusive experimental cross sections and experimental spectroscopic factors were extracted straight from the γ-detector spectrum. The total Coulomb-dissociation cross section was derived analogously to the approach for the ^{17}C case and is listed in table 6.3 along with the partial cross sections.

Partial Cross Sections

Exclusive cross sections were derived utilising the γ-detector. In figure 6.5, the fit to the γ-spectrum for

E [MeV]	I^{π}	l	σ_{sp} [mb]	σ_{exp} [mb]			C^2S		
					stat.	sys.		stat.	sys.
0.0	$3/2^+$	2	27	32 ±	13 ±	5	1.18 ±	0.48 ±	0.19
0.22	$1/2^+$	0	75	40 ±	8 ±	5	0.52 ±	0.11 ±	0.07
0.33	$5/2^+$	2	25	43 ±	6 ±	1	1.74 ±	0.24 ±	0.04
total				115 ±	8				

Table 6.3.: Experimental cross sections (σ_{exp}) and single-particle (σ_{sp}) cross sections [20] in plane-wave approximation as well as the experimental spectroscopic factors C^2S for Coulomb dissociation of ^{18}C. Statistical and systematical uncertainties are shown.

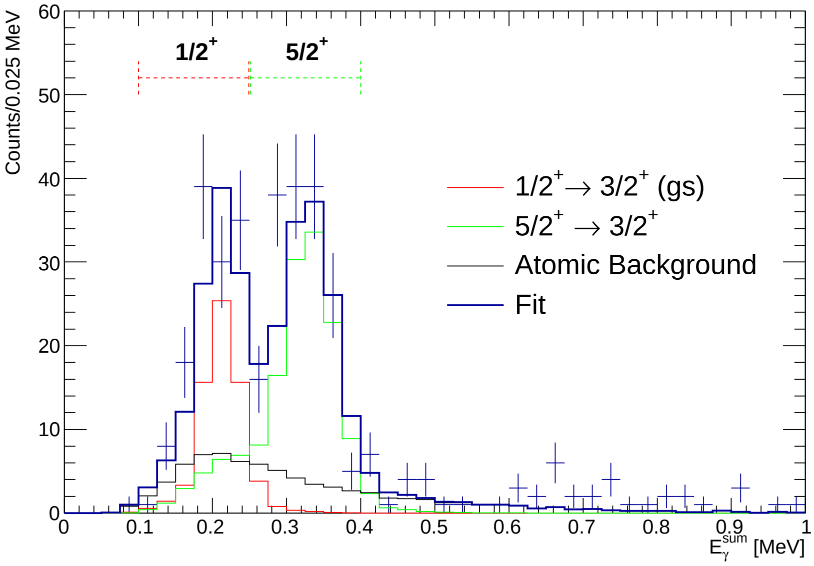

Figure 6.5.: Fit of response function with de-excitations from the $1/2^+$ and $5/2^+$ levels in ^{17}C to the γ spectrum for ^{18}C at 426 AMeV impinging on lead target. Additionally, atomic background was taken into account. The gates for the identification of excited states in ^{17}C are indicated.

^{18}C at 426 AMeV impinging on lead target is presented. The response function (thick line) reproduces experimental data as de-excitations from the $1/2^+$ and $5/2^+$ excited states of ^{17}C on top of atomic background. The latter was extracted from events that indicate non-reacted particles in the fragment-mass spectrum fully analogous to the analysis of ^{17}C Coulex. The fits to lead-target, carbon-target and empty-target runs are presented in figure A.1 to figure A.3 in the appendix. The background cannot be subtracted according to equation (5.8) in a bin-wise manner. The contributions are of different origin such that the shape of the atomic background differs strongly for the runs. Therefore, each spectrum was evaluated separately and afterwards the extracted rates were subtracted as described in Section 5.3.

For the calculation of exclusive cross sections the efficiencies of the γ-detector $\epsilon_{1/2^+} = 0.37$ and $\epsilon_{5/2^+} = 0.60$ from the simulations were used. They are comparably low because of absorption and the proximity of the level energies and the γ-detector thresholds. The latter reveal in the low energy cut-off of the atomic background, which commonly is described by an exponential, in figure 6.5. Here, the cut-off is smooth due to detector-dependent energy thresholds and the Doppler energy-correction. In table A.2, the dependency of the efficiencies from the detector thresholds is illustrated. Comparably small fluctuations result in relevant changes of the ϵ_i. Hence, systematic uncertainties were calculated for variations of the thresholds within the bin width (±25 keV) of the γ-detector spectrum. Therefor the thresholds in the simulations were varied and data was implemented to the response function, which subsequently was fit to experimental data. In table 6.3, the resulting systematic uncertainties are listed along with the statistical fluctuations.

Transitions to the $1/2^+$ and $5/2^+$ excited states in ^{17}C were separated by means of gates on the energy deposited in the γ-detector as indicated in figure 6.5. The integral partial cross sections were calculated fully similar to the case of ^{17}C (see Section 6.1) and the values are summarised in table 6.3. Single-particle cross sections σ_{sp} from the theoretical description with an independent-particle model [20] and the resulting experimental spectroscopic factors are also listed. The partial cross sections are roughly similar for all final states. From relation (6.2) can be concluded that the transition probability *via* Coulomb dissociation of ^{18}C is about the same for all neutron states in the sd-shell.

Energy Differential Cross Sections

Exclusive relative energy spectra were calculated from formula (5.25). In figure 6.6, differential spectra with respect to the relative energy for transitions to the ground state in ^{17}C as well as the first and second excited state are presented. Also shown are theoretical calculations (see section 2.2.1 for details) in plane-wave approximation. These curves were normalised to the experimental spectroscopic factors from table 6.3. An uncertainty due to unambiguous state assignment in the γ-detector spectrum was attributed as systematic error, which is illustrated in bands. The ground state ($3/2^+$) is shown in the upmost panel, the middle and lower panel are the first ($1/2^+$) and second excited state ($5/2^+$), respectively. The theoretical calculations of the Coulomb-dissociation cross sections in plane-wave approximation describe the features of the experimental spectra. Such, they account for the comparably broad distributions of excitations of d-wave neutrons and the peak in the excitation spectrum of s-wave neutrons in the middle panel is reproduced.

6.2.3 Neutron-Capture Cross Sections

The Coulomb-dissociation cross sections were converted into exclusive photo-absorption cross sections with equation (2.12). In figure 2.4, the number of equivalent photons for the most prominent multipole transitions are shown. The spectrum is dominated by $E2$ transitions while in the calculations presented now contributions besides the $E1$ component were neglected. In the response of electric multipoles to transitions to the continuum (see Section 2.2.1) the effective charge $Z^{(\lambda)}_{eff}$ suppresses higher multipolarities. Furthermore, theoretical calculations [20] yielded zero contribution of $M1$ transitions.

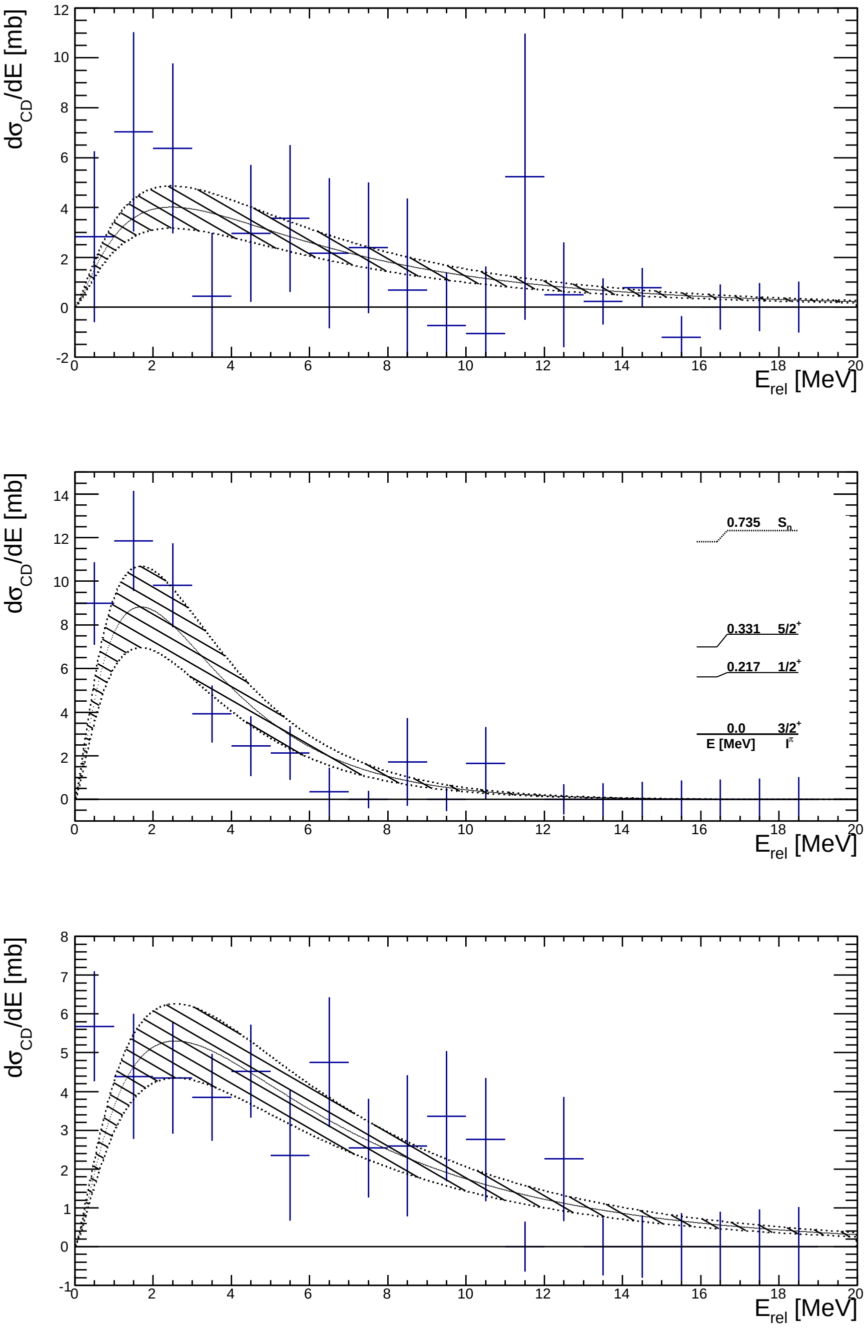

Figure 6.6.: Exclusive differential Coulomb-dissociation cross sections with respect to the relative energy for (up most panel) transitions to the ground state, (middle panel) first excited state and (lower panel) second excited state. Theoretical calculations in plane-wave approximation [20] are also given. The inset shows the relevant part of the level scheme of ^{17}C [69].

The photo-absorption cross sections $\sigma_{\gamma n}$ quantify the probability of γ-absorption with subsequent neutron emission. The $\sigma_{n\gamma}$ exclusive energy differential neutron-capture cross sections were obtained from the detailed-balance theorem equation (2.27). Due to the ground-state spin-parity configuration of ^{18}C, exactly one neutron wave-function can couple to a ^{17}C core state as follows from relation (6.2). Hence, when gating on the $1/2^+$, the $5/2^+$ state or the $3/2^+$ ground state in ^{17}C the detailed-balance theorem is unambiguously fulfilled, since just one neutron state per ^{17}C configuration can be captured.

The experimental energy differential neutron-capture cross sections with respect to the relative energy E_{rel} are shown in figure 6.7. In the astrophysical site of a core-collapse supernova temperatures in the range $T = 1\ldots3\cdot10^9$ K occur [6]. With $T_n = k_B T$ in thermodynamical equilibrium, k_B being the Boltzmann constant, typical kinetic energies $T_n \approx 0.2$ MeV of the neutrons result and just the first energy bin of experimental data is of interest. The correlation of T_n and relative energy E_{rel} is given in equation (5.20).

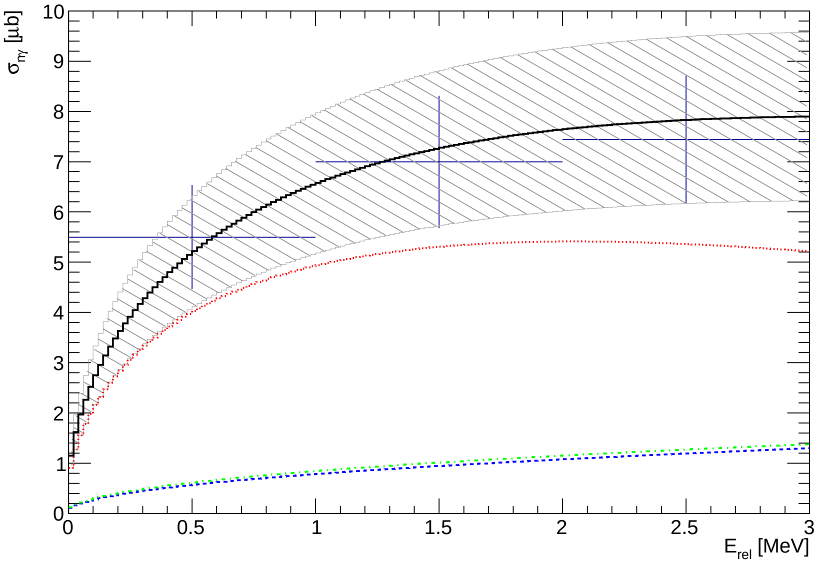

Figure 6.7.: Inclusive experimental neutron-capture cross sections on ^{17}C and exclusive theoretical calculations, which were provided by S. Typel [20]. Therefor capture to $\nu 0d_{3/2}$-state (red dashed line), $\nu 1s_{1/2}$-state (green dotted line) and $\nu 0d_{5/2}$-state (blue dash-dotted line) were taken into account. The solid line is the sum of the theoretical cross sections.

The calculations of the experimental neutron-capture cross sections were performed separately for the exclusive captures to the $\nu 0d_{3/2}$, $\nu 1s_{1/2}$ and $\nu 0d_{5/2}$ states on the $3/2^+$, $1/2^+$ and $5/2^+$ levels in ^{17}C, respectively, and the results were combined afterwards to the inclusive cross section. The theoretical calculations [20] for the capture to the $\nu 0d_{3/2}$-state (red dashed line), the $\nu 1s_{1/2}$-state (green dotted line) and the $\nu 0d_{5/2}$ state (blue dash-dotted line) were scaled accordingly to the experimental spectroscopic factors from table 6.3 and are also given in figure 6.7. The sum (black solid line) was attributed an uncertainty reflected in the band due to unambiguous state assignment in the γ-spectrum. The scaled theoretical neutron-capture cross section describe the experimental data points in the presented energy range very well. At higher energies deviations, which can be attributed to high-energy resonances in the Coulomb-dissociation reactions, occur. Such resonances were not analysed further, because the statistics at higher relative energies is poor (compare figure 6.6) and this energy region is irrelevant for the investigations of neutron capture for the r-process.

Thermonuclear Reaction Rates

The energy-differential cross sections for neutron capture in the ground state as well as the first and second excited state of ^{17}C in figure 6.7 were used to calculate reaction-rates with formula (2.32). In this procedure the scaled theoretical curves were used, because the binning of experimental data appears disadvantageous. The temperature dependent rate for neutron capture on ^{17}C to the ground state of ^{18}C is presented in figure 6.8 in the temperature range $T_9 = 0.01 \ldots 10$ GK, where 1 GK corresponds to $E_{rel} \approx 100$ keV. The reaction rates for exclusive neutron captures to the ground and excited states of ^{17}C can be found in figure A.7 to figure A.9. The scaled theoretical curves were fit by the parametrisation used by Sasaqui *et al.* [9] for comparison with that publication:

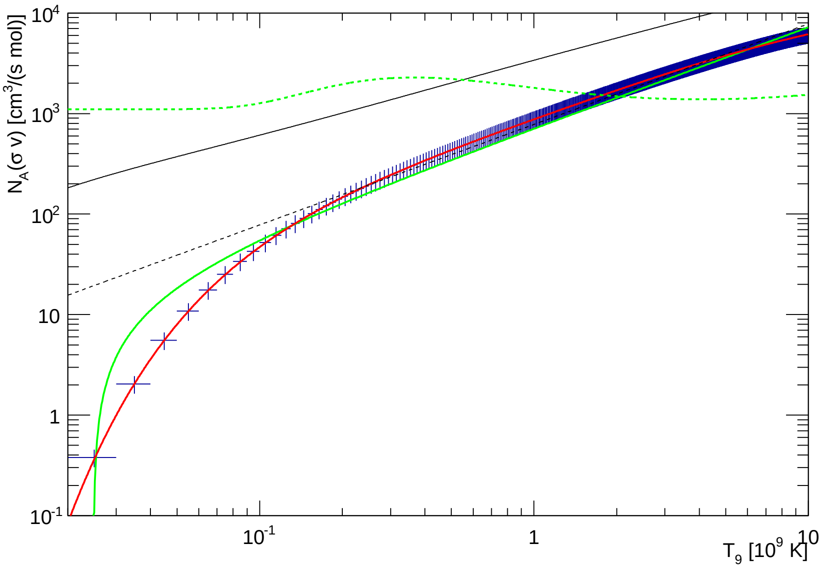

Figure 6.8.: Stellar reaction-rates for neutron capture on ^{17}C to the ground state of ^{18}C. The fits with the parametrisation used by Sasaqui *et al.* [9] and those suggested by Rauscher and Thielemann [25] are indicated in green and red, respectively. The green solid line represents the fit to experimental data while the dashed line illustrates the Hauser-Feshbach calculation in [9]. For comparison, rates for the ^{14}C$(n,\gamma)^{15}$C reaction are presented by the black lines. In that case the results from Reifarth *et al.* [11] and [9] are illustrated with the solid and dashed line, respectively.

$$N_A\langle\sigma v\rangle = a + b \cdot T_9 + c \cdot T_9^{-3/2} \exp(-d/T_9). \tag{6.3}$$

Here, N_A is the Avogadro constant and $\langle\sigma v\rangle$ is the expectation value of the exclusive neutron-capture cross sections for neutrons in thermodynamic equilibrium (see Section 2.3.1 for details) at the astrophysical site. Function (6.3) was fit to the scaled theoretical data (green curve) and the fit parameters for reactions rates in cm^3/(s·mol) are listed in table 6.4, along with the values from a Hauser-Feshbach calculation in [9]. Additionally, a fit with the parametrisation proposed by Rauscher and Thielemann [25]:

$$N_{\mathrm{A}}\langle\sigma v\rangle = \exp\left(a + b\cdot T_9^{-1} + c\cdot T_9^{-1/3} + d\cdot T_9^{1/3} + e\cdot T_9 + f\cdot T_9^{5/3} + g\cdot\ln(T_9)\right), \tag{6.4}$$

was considered. The corresponding reaction-rate curve is marked in red in the illustration and the parameters are listed in table 6.5.

In figure 6.8, the reaction rate of neutron capture on ^{17}C used by Sasaqui *et al.* [9] from a calculation utilising the Hauser-Feshbach model is represented by the dashed green line. It is significantly different from the present result, which also reflects in enormously differing fit parameters in table 6.4. The discrepancy may be tracked back to the statistical model in the theoretical calculations. It was already mentioned in that publication that the statistical approach appears inappropriate for the description of light nuclei due to poor level-density.

For comparison, the reaction rates for the ^{14}C$(n,\gamma)^{15}$C case in [9] and from Reifarth *et al.* [11] are shown by the black dashed line and the black solid line, respectively. The reaction rate is assumed to be uncertain by a factor of four in the former publication while the actual deviation is in the order of a factor of ten.

I^π	Fit Parameter				$\Delta\lambda$
	a	b	c	d	
[9]	$1.1\cdot10^3$	40.5	$1.133\cdot10^3$	0.541	×10
	-18.0 ± 0.8	724 ± 1	0 ± 1	11 ± 1	≤60%
$3/2^+$	-2.19 ± 0.03	87.8 ± 0.9	0 ± 1	45 ± 1	55%
$1/2^+$	-11.6 ± 0.2	473 ± 7	$(5\pm1)\cdot10^3$	3.1 ± 0.2	20%
$5/2^+$	-2.08 ± 0.02	83.7 ± 0.9	$(3.0\pm0.5)\cdot10^3$	6.6 ± 0.3	≤1%

Table 6.4.: Parameters of the fit function (6.3) of the stellar reaction-rates from the parametrisation by Sasaqui *et al.* [9]. The parameters from the statistical model in [9] are also given. In the last column the uncertainties of the rates at $T_9 = 1$ GK for the present data are shown.

The parametrisation by Sasaqui *et al.* [9] yields best agreement for d-wave neutron capture in ^{18}C, *i.e.* capture in the ground state ($3/2^+$) and second excited state ($5/2^+$) in ^{17}C. It appears inappropriate for the description of the first excited state ($1/2^+$) shown in figure A.8. However, the approximated curves diverge for all reaction channels at temperatures lower than 0.1 GK. On the other hand, the present exclusive data can be fit with higher accuracy by the parametrisation of Rauscher and Thielemann [25]. Such, the deviation at $T_9 = 1$ GK is less than 2% in all cases.

6.3 Discussion

The measurements of the integral and energy differential Coulomb-dissociation cross sections of ^{17}C presented in section 6.1 were compared to the earlier analysis of a Coulomb-breakup experiment by Pramanik *et al.* [12]. In table 6.2, the experimental spectroscopic factors from theoretical calculations in plane-wave and distorted-wave approximation are summarised. The single-particle cross sections σ_{sp} in distorted-wave approximation in [12] differ strongly from those used here, which results in diverging experimental spectroscopic factors. On the other hand, all experimentally obtained exclusive cross sections are in good agreement. This confirms the accuracy of the presented analysis technique of experimental data, comprising for example the efficiency corrections for the γ- and neutron-detector. The

I^{π}	a	b	c	d	e	f	g
	4.68 ± 0.10	$(-1.3 \pm 0.1) \cdot 10^{-1}$	$(-2.3 \pm 0.5) \cdot 10^{-1}$	-2.69 ± 0.02	$(-2.5 \pm 0.4) \cdot 10^{-1}$	$(-1.4 \pm 0.6) \cdot 10^{-2}$	$(1.0 \pm 0.5) \cdot 10^{-1}$
$3/2^+$	5.4 ± 0.2	$(-2.1 \pm 0.2) \cdot 10^{-1}$	4.1 ± 0.2	-5.02 ± 0.10	$(3.0 \pm 0.3) \cdot 10^{-1}$	$(-2.1 \pm 0.4) \cdot 10^{-2}$	3.59 ± 0.07
$1/2^+$	6.68 ± 0.09	$(-1.9 \pm 0.1) \cdot 10^{-1}$	3.32 ± 0.09	-3.39 ± 0.06	$(1.2 \pm 0.2) \cdot 10^{-1}$	$(-9 \pm 2) \cdot 10^{-3}$	2.92 ± 0.04
$5/2^+$	5.40 ± 0.05	$(-2.06 \pm 0.06) \cdot 10^{-1}$	4.05 ± 0.05	-4.92 ± 0.03	$(2.95 \pm 0.09) \cdot 10^{-1}$	$(-2.1 \pm 0.1) \cdot 10^{-2}$	3.55 ± 0.02

Table 6.5.: Parameters of the fit function (6.4) of the stellar reaction-rates.

cross sections were calculated up to excitation energies $\epsilon = 20$ MeV like in [12]. Based on a comparison of the spectroscopic factors in plane-wave approximation in table 6.2, the precision of experimental data in the present analysis appears slightly improved.

The experimental spectroscopic factors are also in agreement with the analysis of the one-neutron knockout experiment by Maddalena *et al.* [67]. However, the present analysis tends to smaller d-wave contributions, which may exhibit a lower sensitivity of the experimental technique to the respective wave functions. Palit *et al.* [47] classified the regions of the radial wave function of the nucleon where breakup reactions take place. It was pointed out that nuclear induced reactions exceed more to the interior of the density distribution while Coulomb dissociation strongly effects its exterior tail. The single-particle model may not fully describe the Coulomb-excitation process for deeper bound nuclei, which may explain the trend to a lower spectroscopic factor in the present analysis when d-wave neutrons are involved.

In figure 6.9, the energy differential exclusive cross sections of Coulomb dissociation of ^{18}C with respect to the relative energy are shown. Here, theoretical calculations in distorted-wave approximation [20] are given. The final-state interaction in the excitation of d-wave neutron states (upmost and lowest panel) accounts for broader experimental spectra. This results in an additional contribution at around 8 MeV, when the interaction-potential depth was adjusted to around -50 MeV. It may be varied to fit experimental data better. Since the agreement of the plane-wave calculations is sufficient, this was not done.

The experimental spectroscopic factors C^2S were compared to the analysis of a knockout experiment by Kondo *et al.* [75]. In table 6.6, the C^2S from calculations in plane-wave and distorted-wave approximation [20] are summarised and statistical as well as systematic uncertainties for the present analysis are given. In addition, the results from nuclear neutron removal [75] are listed. The spectroscopic factors of transitions to the $3/2^+$ and $1/2^+$ states are in agreement. In contrast, the result differs for the $5/2^+$ case where the deviation amounts to 5% in plane-wave approximation. In the theoretical description default parameters of the Woods-Saxon potential were chosen (2.2.1). The model comprises various possibilities to adjust the single-particle wave functions and hence the spectroscopic factors. In this way the gap in the $5/2^+$ case can be bridged [78].

The reduction factor:

$$R_S = \frac{\sigma_{\text{exp}}}{\sigma_{\text{th}}} \equiv \frac{C^2S_{\text{exp}}}{C^2S_{\text{th}}}, \tag{6.5}$$

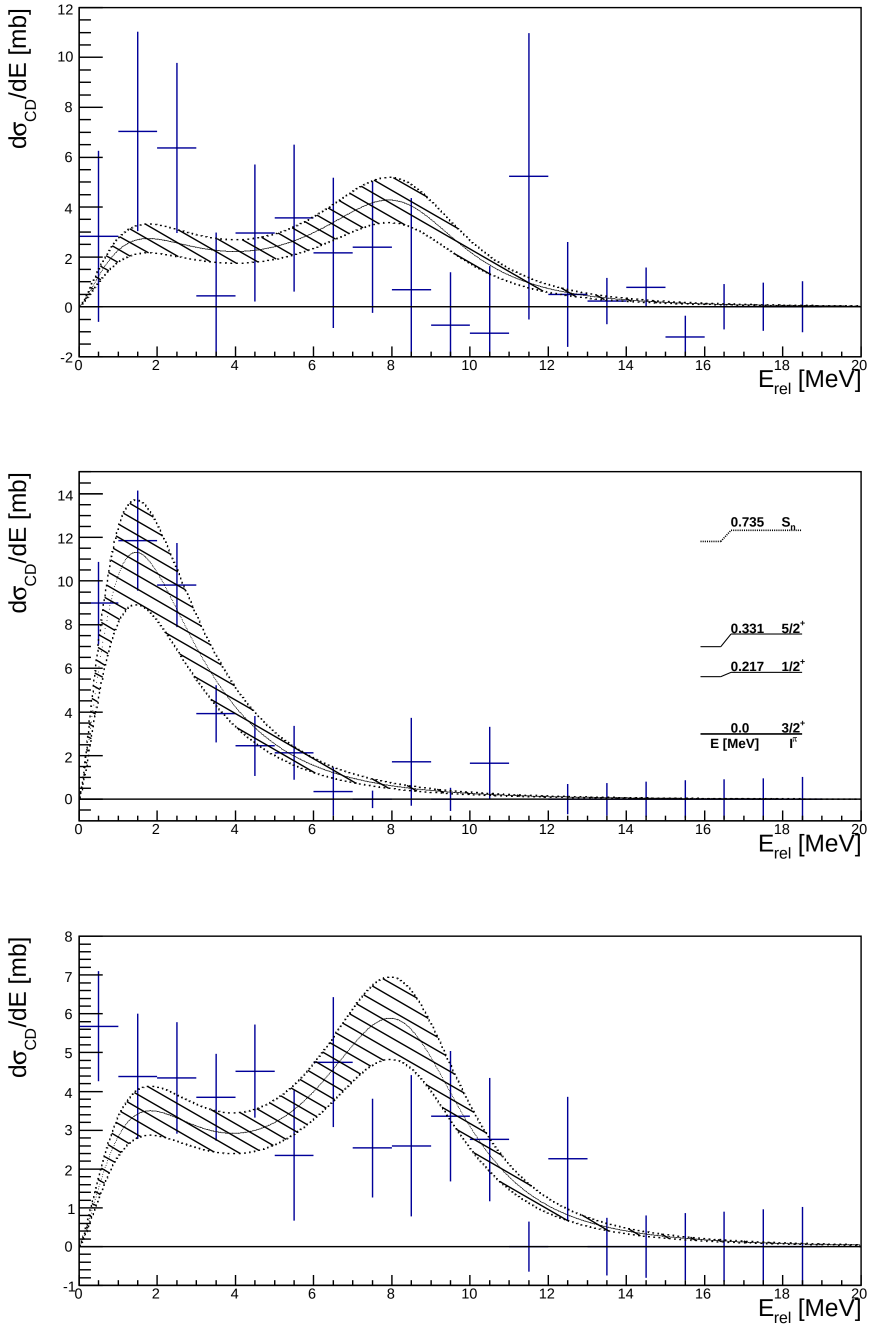

Figure 6.9.: Exclusive differential Coulomb-dissociation cross sections with respect to the relative energy E_{rel} for (up most panel) transitions to the ground state, (middle panel) first excited state and (lower panel) second excited state in ^{17}C. The theoretical calculations in distorted-wave approximation [20] were scaled to the experimental spectroscopic factors in table 6.6. The inset shows the relevant part of the level scheme of ^{17}C [69].

E [MeV]	I^π	C^2S		
		Coulomb Breakup		Knockout [75]
		Plane-Wave	Distorted-Wave	
		stat. sys.	stat. sys.	
0.0	$3/2^+$	$1.18 \pm 0.48 \pm 0.19$	$1.03 \pm 0.42 \pm 0.16$	≤ 0.67
0.22	$1/2^+$	$0.52 \pm 0.11 \pm 0.07$	$0.56 \pm 0.11 \pm 0.07$	0.39 ± 0.07
0.33	$5/2^+$	$1.74 \pm 0.24 \pm 0.04$	$1.48 \pm 0.21 \pm 0.03$	2.39 ± 0.27

Table 6.6.: Experimental spectroscopic factors from Coulomb-dissociation calculations in plane-wave and distorted-wave approximation compared to the results from a knockout experiment [75]. The calculations were performed for the bound states I^π in ^{17}C and were provided by S. Typel [20]. For the present analysis the statistical and systematic uncertainties of experimental data are given.

provides a measure on the reduction of the measured neutron removal cross sections σ_{exp} relative to theoretical values σ_{th}. Here, the third term of (6.5) is of interest, since the spectroscopic factors are somewhat independent of the experimental method. The C^2S_{exp} were extracted as described before while the C^2S_{th} was taken from shell-model calculations in Kondo *et al.* [75]. With equation (6.5) one-neutron removal of ^{18}C *via* Coulex was sorted into the systematics of Gade *et al.* [79] in figure 6.10. The difference in the separation energies of the two nucleon species is defined as $\Delta S = S_n - S_p$ for neutron removal and *vice versa* for proton removal. Therefore, ΔS is big when a strongly bound nucleon of the deficient species is removed and it takes on negative values when a weakly bound nucleon of the excess species is removed. The data point for ^{18}C Coulex in green with a large negative ΔS appears at a reduction close unity and follows the systematics of the presented data. Those are normalised to shell-model calculations by σ_{th} and C^2S_{th}, respectively.

For the calculation of the shell-model spectroscopic factors in the case of ^{18}C nuclear neutron removal in Kondo *et al.* [75] the WPB effective interaction was utilised. The reduction factor presented here is based on the theoretical single-particle cross sections from [75] and close to unity. The correlations in the shell-model apparently are less important, since there is little reduction with respect to the independent-particle model [20]. However, the theoretical spectroscopic strength of 3.55 [75] compares to the occupation number of four neutrons in the sd-valence shell. The difference hints on correlations beyond those in the shell-model calculation, for example short-range correlations.

The experimental partial cross sections of the excited states were derived from the fit of the response function to the summed γ-energy spectrum in figure 6.5. They agree within uncertainties with the results of the analysis of the single-detector spectrum of the γ-detector, which is presented in figure A.4 in the appendix. Finally, the summed spectrum was preferred, because of more efficient background suppression. The cross section to the ground state was obtained from events without response of the γ-detector. Such events were corrected for the detection inefficiency of the crystals. Due to this procedure all cross sections which have been extracted are dependent on each other. Hence, any modification of one cross section and its associated spectroscopic factor will cause a change of all others.

It was depicted in Section 2.2.3 that the Asymptotic Normalisation Coefficient (ANC) quantifies the amplitude of the exterior tail of the radial single-particle wave function. Electromagnetic excitations are most sensitive to this region [23] and the ANC provides a more distinct measure of the independent-particle model than the C^2S. For s- and d-wave neutrons the ANCs corresponding to unity spectroscopic factors are 0.9101 fm$^{-1/2}$ and 3.9546 fm$^{-1/2}$, respectively.

The reaction rates for neutron capture in ^{17}C to the ground state of ^{18}C from a Hauser-Feshbach calculation λ_{HF} by Sasaqui *et al.* [9] are compared to the present results λ_{exp} in figure 6.11. The ratio $\lambda_{\text{HF}}/\lambda_{\text{exp}}$ is presented in the temperature range $T_9 = 0.01 \ldots 10$ GK and the uncertainty from the

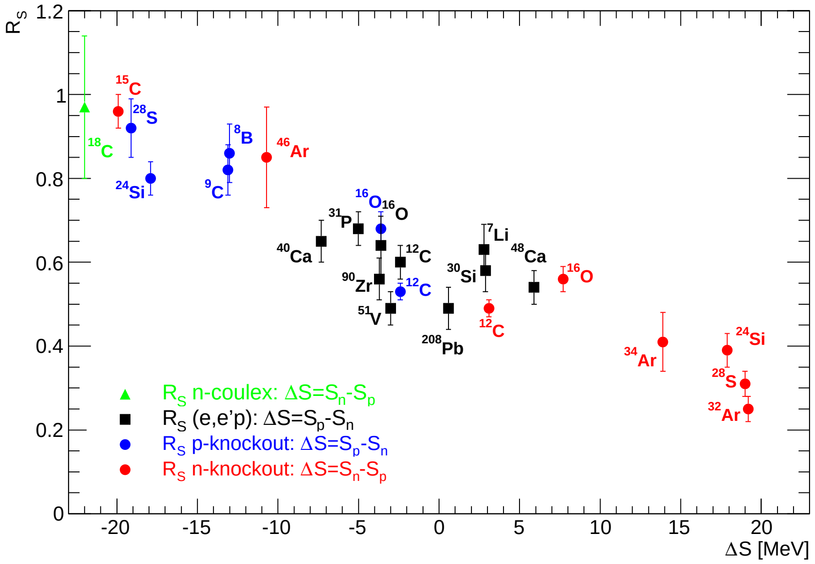

Figure 6.10.: Reduction of the measured nucleon-removal cross sections with respect to theoretical calculations R_S as a function of the difference in the neutron and proton separation-energies ΔS. Values besides the ^{18}C data point were taken from Gade *et al.* [79].

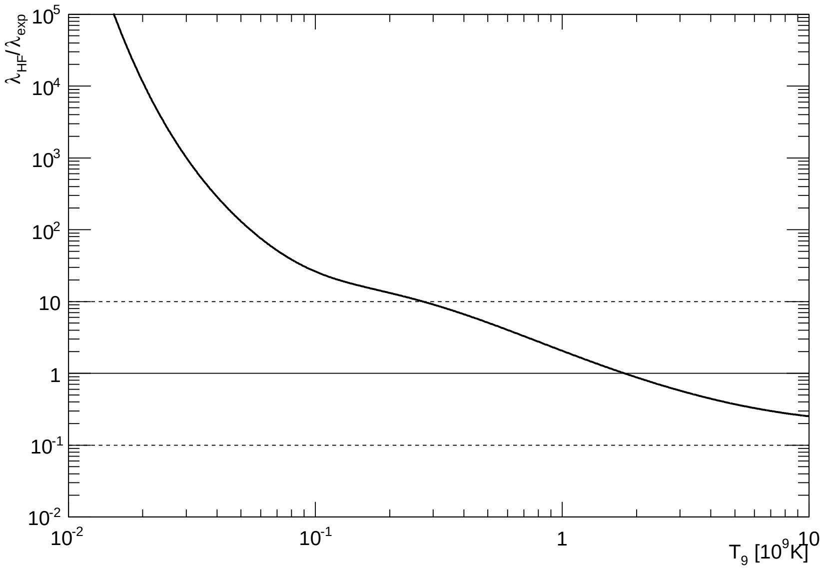

Figure 6.11.: Ratio of reaction rates ^{17}C$(n,\gamma)^{18}$C from the Hauser-Feshbach model in [9] and data presented here. The uncertainties from the theoretical calculations are indicated by the dashed lines. $T_9 = 1$ GK corresponds to $E_{rel} \approx 100$ keV

theoretical calculation is indicated by the dashed lines. Data are consistent over a vast temperature range, but significant deviations occur for $T_9 \leq 0.05$ GK. Note that $T_9 = 1$ GK corresponds to $E_{rel} \approx$ 100 keV. Neutrons with energies corresponding to $T_9 = 0.01 \ldots 10$ GK may be captured directly into states of ^{18}C or into isolated states in the continuum, because the level density (see figure 6.4) is low. Therefore, a statistical treatment may be unsuited. This situation changes at higher temperatures, *i.e.* capture to higher-lying states in the continuum and the Hauser-Feshbach approach yields more adequate results. Note that it was already mentioned by Sasaqui *et al.* [9] that the statistical model may be inappropriate for the description of light nuclei due to low level-density. Additionally, the capture into different states of ^{18}C can play a role. The rates presented here refer to neutron capture to the ground state of ^{18}C due to the experimental approach. Based on (unknown) selection rules the neutron capture to the ground state may be suppressed at temperatures below $T_9 = 0.05$ GK while the ground state may be populated more and more likely with increasing temperature and theory becomes more consistent with the data present here.

7 Conclusions and Outlook

In the analysis presented in this work neutron-capture reaction-rates for neutron-rich carbon were derived from experimental data. Therefor it was illustrated by means of a test case that Coulomb-dissociation reactions were investigated with reliable accuracy. The exclusive experimental spectroscopic factors for Coulomb dissociation of ^{18}C were furthermore validated by comparison to an earlier knockout experiment. Finally, exclusive neutron-capture rates for the bound states of ^{17}C to the ground state of ^{18}C were extracted. Due to the experimental approach transitions to excited states of ^{18}C cannot be investigated. Hence, the total rate of ^{17}C neutron captures including all states of ^{18}C has to be obtained from theoretical considerations. For the present analysis, single-particle Coulomb-dissociation cross sections were calculated for the excitation of the ground state in ^{18}C. In the same manner the according cross sections from excited states in ^{18}C could be calculated, applying spectroscopic factors from shell-model calculations. The ratio of newly calculated data concerning Coulomb dissociation of excited states in ^{18}C and existing calculations then provides an estimate of the relevance of the presented rates with respect to the entity of neutron-capture transitions between ^{17}C and ^{18}C.

An earlier calculation with the Hauser-Feshbach model estimated the uncertainty for the neutron-capture rate on ^{17}C to a factor of ten. The presented results deduced from Coulomb-dissociation have an uncertainty of 60% at maximum. The statistical and systematic errors are of about similar importance. The former simply correlates with the available beam-time while the performance of the γ-detector and the efficiency correction of the neutron detector govern the systematical uncertainty of experimental data. In detail, ambiguities related to the identification of the excitation of the ^{17}C fragment play an important role. The de-excitation energies are critically proximate to each other ($\approx$ 100 keV) with respect to the energy resolution of the γ-detector and to the thresholds of the crystals of the γ-detector. Hence, data accuracy could be improved with detectors of higher energy-resolution and lower zero-noise behavior as well as higher granularity of the entire γ-detector. For this purpose, the so-called CALorimeter for In-Flight emitted pArticles detection (CALIFA) [80], which is under construction at the time of writing this document, is designed.

In a next step the deduced reaction rates have to be incorporated to a full r-process network calculation to validate their influence on the reaction flow and produced abundances. Therein the branching with respect to excited states of ^{18}C has to be taken into account. The results will be compared to calculated abundances with reaction rates from the Hauser-Feshbach model. In this way, the sensitivity of the r-process nucleosynthesis to the neutron-capture reaction-rates on ^{17}C will be derived. Furthermore, the variation of the results within the uncertainties of the presented reaction rates is of interest. Such, the applicability of the presented experimental technique for the calculation of neutron-capture reaction-rates can be confirmed.

The statistical model strongly overestimates the neutron-capture reaction rates at temperatures below $T_9 = 0.1$ GK. This may be a feature of light neutron-rich nuclei, that are considered “neutron poison” in the r-process. From an investigation of other nuclei a systematics can be obtained, which might lead to a common treatment of the neutron-capture reaction-rates of light neutron-rich nuclei in nucleosynthesis simulations.

A Data Analysis

A.1 Issues Related to XB Data for ^{18}C Coulex

Ring	Crystal	$\epsilon_{1/2^+}$ [%]	$\epsilon_{5/2^+}$ [%]
0.	81 (beam line)	–	–
1.	60, 61, 62, 90, 91, 92	8.8	13.7
2.	41, 42, 43, 59, 63, 80, 89, 93, 111, 112, 113, 114	24.5	33.3
3.	24, 25, 26, 27, 40, 44, 58, 64, 94, 110, 115, 127, 128, 129, 130, 131	32.4	47.6
4.	11, 12, 13, 23, 28, 39, 45, 57, 65, 79, 88, 95, 109, 116, 126, 132, 143, 144, 145, 146	34.6	55.2
5.	3, 4, 10, 14, 22, 29, 56, 66, 78, 87, 96, 108, 133, 142, 147, 155, 156, 157	36.3	58.4
6.	1, 2, 5, 9, 15, 38, 46, 86, 117, 125, 148, 154, 158, 161, 162	36.9	59.6
7.	6, 7, 8, 16, 21, 30, 55, 67, 76, 85, 97, 107, 134, 141, 149, 153, 159, 160	37.6	62.0
8.	17, 18, 19, 20, 31, 37, 47, 54, 68, 75, 84, 98, 106, 118, 124, 135, 140, 150, 151, 152	38.2	64.5
9.	32, 33, 34, 35, 36, 48, 53, 69, 99, 105, 119, 123, 136, 137, 138, 139	38.7	65.9
10.	49, 50, 51, 52, 70, 74, 83, 100, 104, 120, 121, 122	39.1	67.1
11.	71, 72, 73, 101, 102, 103	39.3	67.6
12.	82 (beam line)	–	–

Table A.1.: Accumulated detection efficiencies ϵ_i for de-excitations from the $1/2^+$ and $5/2^+$ levels in ^{17}C dependent on the covered polar angle θ. The rings are characterised by the crystal number and correspond to gradually increasing angle. The sixth ring represents $\theta = 90°$ and the entire solid angle is covered, when the twelfth ring is included.

	$\epsilon_{1/2^+}$ [%]		$\epsilon_{5/2^+}$ [%]	
	Entire XB	Forward	Entire XB	Forward
Thr. -100 keV	59.7	55.6	76.9	67.7
Thr. -50 keV	50.9	46.8	73.7	64.7
Thr. -25 keV	45.4	42.0	71.2	62.4
Thr. -10 keV	41.8	39.0	69.2	60.8
Thresholds	39.3	36.9	67.7	59.6
Thr. +10 keV	36.9	34.9	65.8	58.4
Thr. +25 keV	33.2	31.8	62.5	56.6
Thr. +50 keV	26.9	26.2	56.4	53.0
Thr. +100 keV	15.9	15.6	45.7	45.0

Table A.2.: Detection efficiencies ϵ_i for de-excitations from the $1/2^+$ and $5/2^+$ levels in ^{17}C when applying various detector thresholds. The forward direction comprises the crystals up to the sixth ring (see table A.1) and covers around half of the total solid angle.

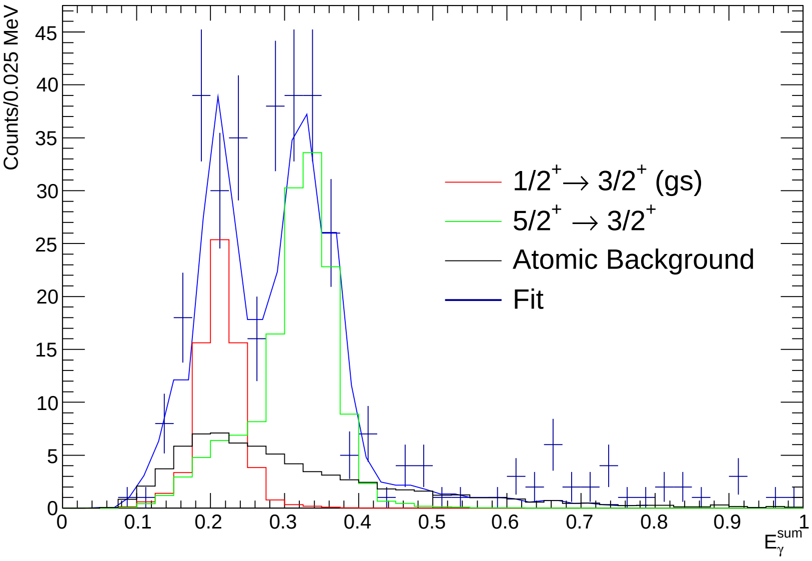

Figure A.1.: The fit of de-excitations from the $1/2^+$ and $5/2^+$ levels in ^{17}C to the XB energy-sum spectrum for ^{18}C at 426 AMeV impinging on lead target is presented. Additionally, atomic background was taken into account.

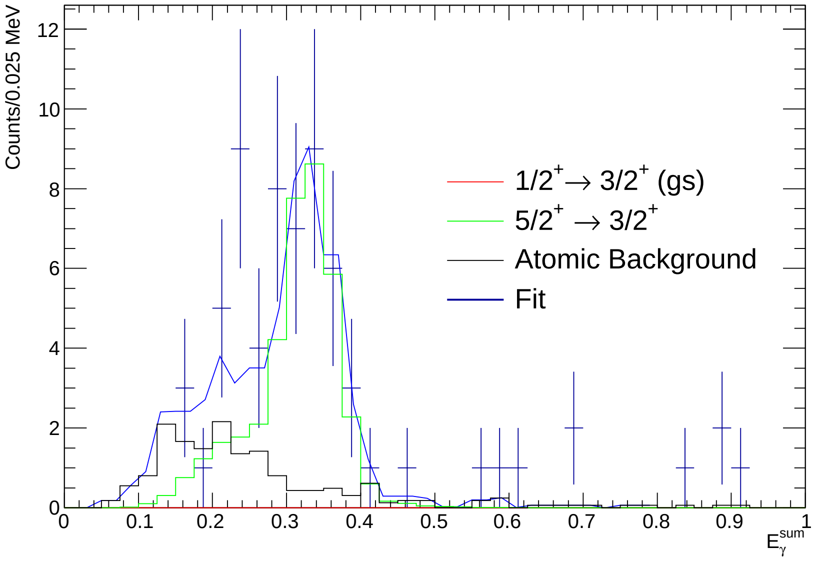

Figure A.2.: The response function is fit to the XB energy-sum spectrum for ^{18}C at 426 AMeV impinging on carbon target.

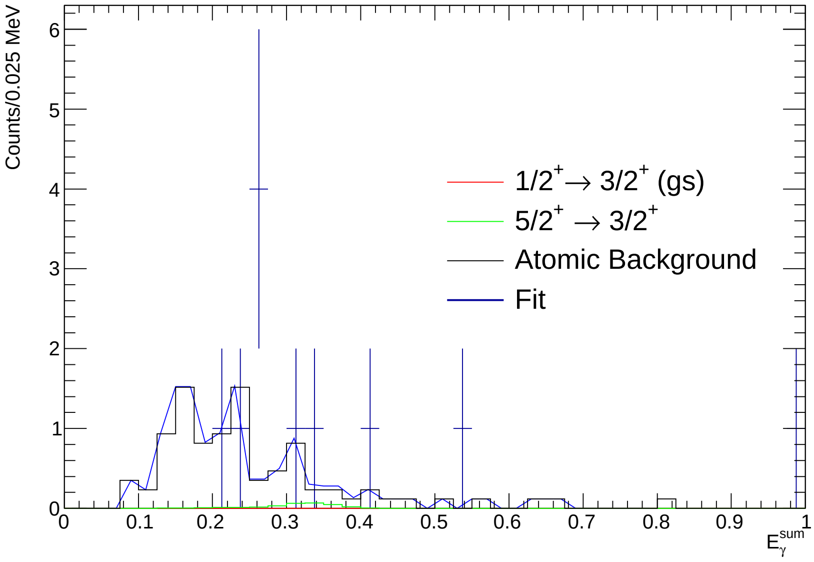

Figure A.3.: The response function is fit to the XB energy-sum spectrum for ^{18}C at 426 AMeV in an empty target runs.

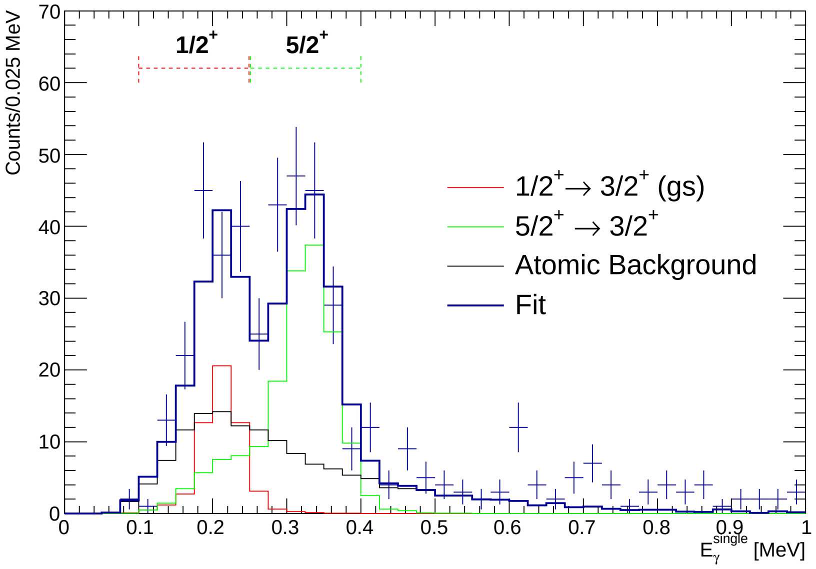

Figure A.4.: The fit of de-excitations from the $1/2^+$ and $5/2^+$ levels in ^{17}C to the single-energy XB spectrum in forward direction for ^{18}C at 426 AMeV impinging on lead target is presented.

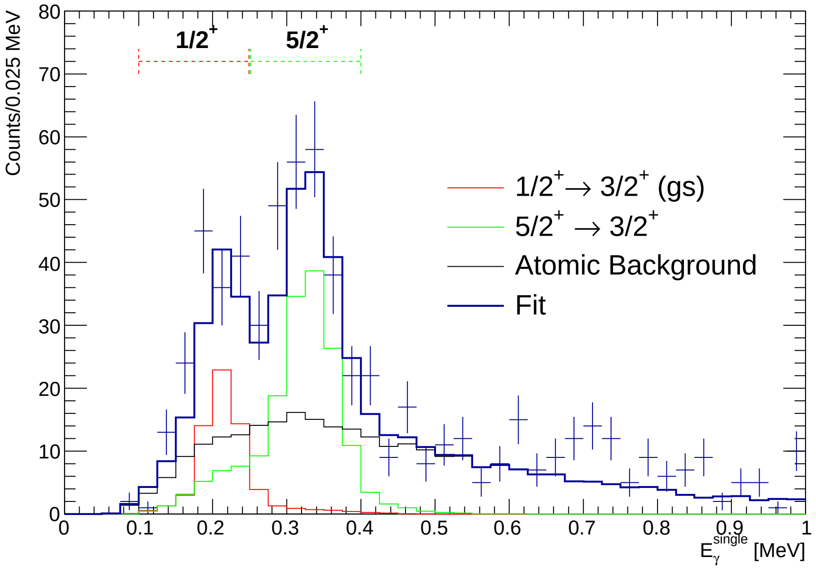

Figure A.5.: Same like above, when considering the entire XB.

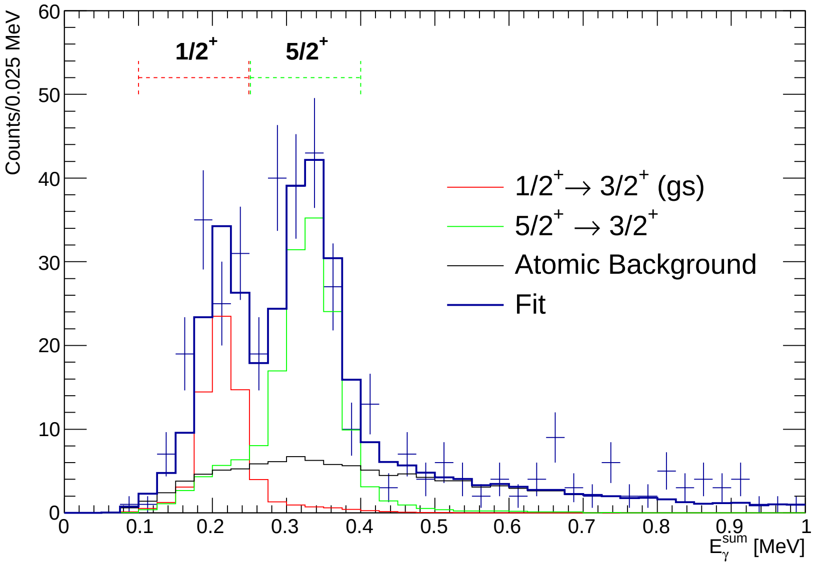

Figure A.6.: The response function is fit XB energy-sum spectrum, utilising all crystals.

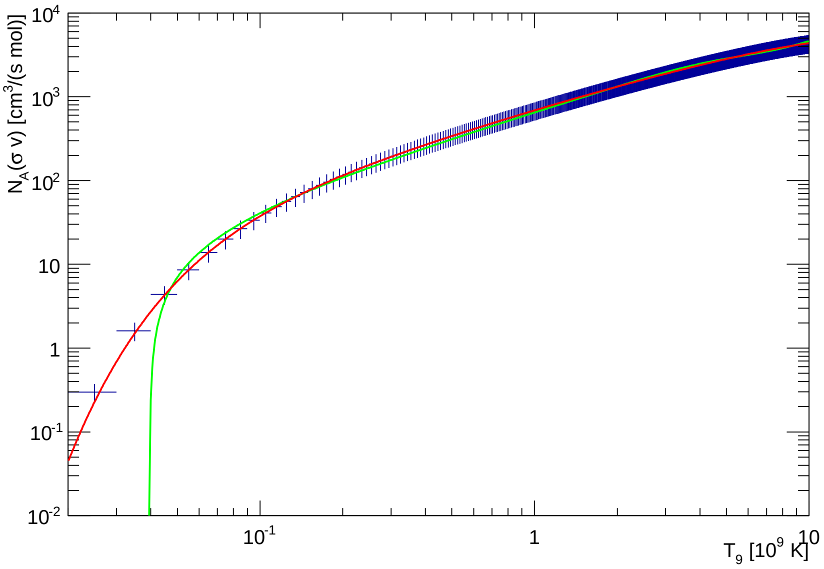

Figure A.7.: Reaction rates for neutron capture in the ^{17}C ground state to the ^{18}C ground state. The fits in green and red are described in the text.

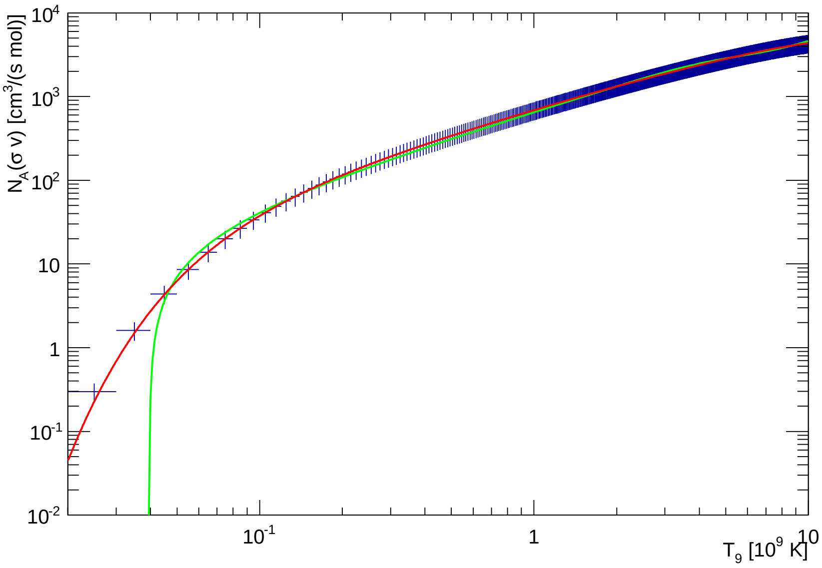

Figure A.8.: Reaction rates for neutron capture in the ^{17}C first excited state to the ^{18}C ground state. The fits in green and red are described in the text.

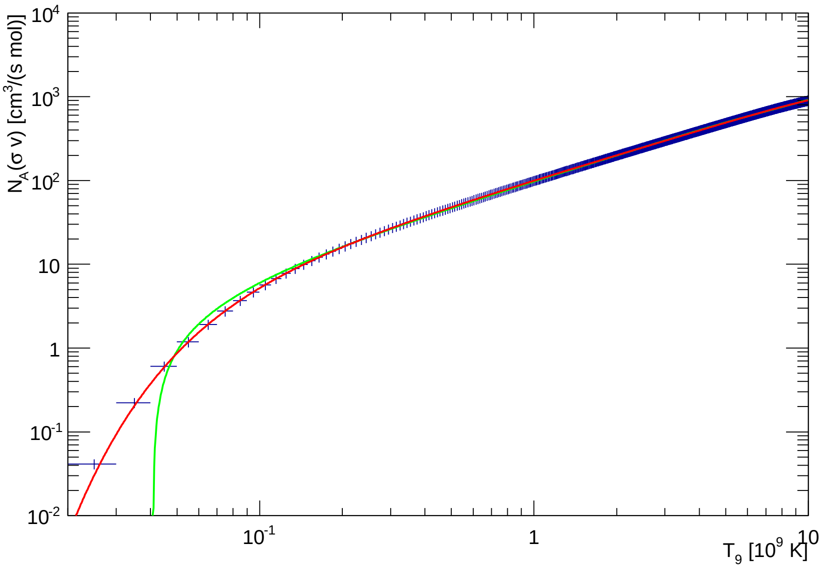

Figure A.9.: Same like above, here with respect to the second excited state in ^{17}C.

B Photogrammetric Position Measurement

The detector positions in the experimental hall are required for the calculation of `TRACK`-level data in `LAND02` and for the reconstruction of the fragment-mass spectrum by the `tracker`. Precise measurements with conventional tools like rulers or lasers of the relatively complicated and partly compact detector position distribution are hampered by readout electronics, supporting and holding structures as well as the complex setup itself. It comprises detectors of several hundreds micrometres thickness (DSSSDs) and likewise LAND with a volume of a few cubic metres. This motivates the use of a measurement technique that is exclusively dependent on visual characteristics of the investigated object, *i.e.* an approach to derive the detector positions from photos.

In the first section, the photo taking and camera equipment is briefly described. Afterwards, an overview on the calculation of a 3D model from this data with the `PhotoModeler`* software package [81] is given, including a *How To* for the reconstruction of the presented position data. Finally, the results are discussed.

B.1 Photo Shooting

The photographs were taken with V. Volkov utilising a 6.3 mega pixel Pentax K100D digital reflex camera. It was equipped with a SMC Pentax DA objective with focal length 18-55 mm and maximum aperture of 3.5-5.6 mm diameter. For the position measurements a focal length of 18 mm, a light sensitivity ISO 400, while auto exposure times were chosen. The latter was shortened in various cases after an instant image-quality check.

Several views on the detector of interest were necessary in the photo taking. In general, it was aimed to cover a wide solid angle to avoid distortions due to poor data, that is missing reference points. Furthermore, pictures were taken such that various detectors are visible in the same photo in order to link their positions unambiguously in the analysis software in the next step of the procedure. Most of the detectors were identified by means of the corners of their housing, because those are precisely defined and visually accessible in a sufficiently wide range of the solid angle. In case of the ToF walls TFW and the Dicke Tof Wand (DTF) prominent points on the holding construction were used. In addition to such references markers as shown in figure B.1 were placed at critical areas of the setup to increase the number of reference points between different views, *i.e.* photos. Such a marker is shown in original size on the left side in figure B.1. The cross at the centre yielded convenient position definition.

The grid for the calibration of the camera is shown on the right side in figure B.1. It was used to correct aberrations from the camera optics in a step wise procedure. Therefor a series of twelve photos from different views in a requested order was taken. The camera orientations were portrait, inverted portrait and landscape format, always rotated by 90° (four times in total) around the grid. It was necessary to keep the lens position and camera adjustment the same. The best calibration was obtained from a run there the grid was imaged completely on all pictures while the covered area on the photograph was maximised. The orientation of the calibration grid is well defined due to the characteristic markers in the corners. A separate program in the `PhotoModeler` software package finally performed the calibration by calculating the residue of the real grid points and the imaged pattern. The calibration parameters were stored in a file which was included into the subsequent analysis.

---

* Eos Systems Inc.

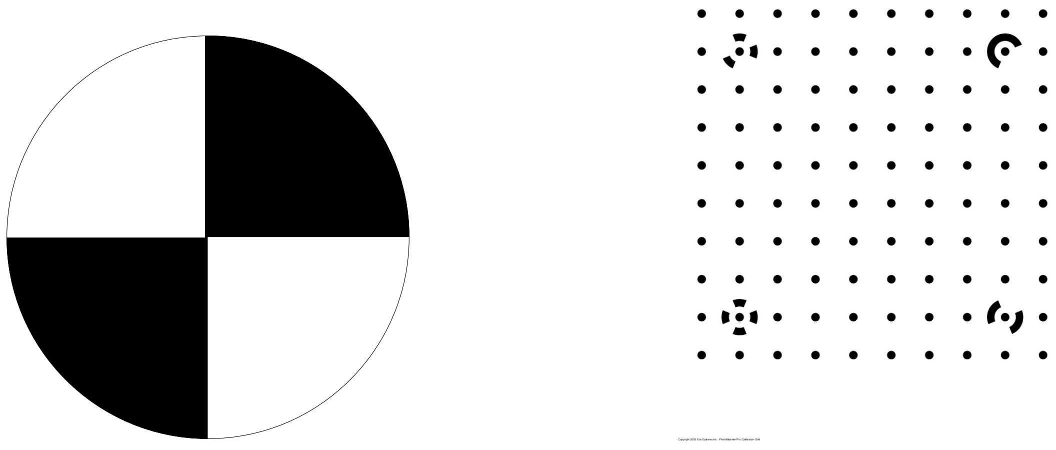

Figure B.1.: (Left) Marker for the photogrammetric position measurement. (Right) Camera calibration grid in the `PhotoModeler`.

B.2 Reconstruction of the Experimental Setup

For the calculation of a 3D model from photos with 2D information the so-called inner and exterior camera orientation have to be taken into account. The former is given from the characteristics of the camera and comprises *e.g.* its focal length, the image format and the principle point. These parameters were either kept fix or were corrected in the calibration of camera aberrations. An example for the exterior camera orientation is the camera position with respect to the imaged object. The situation for a simplified case is shown in figure B.2. The object arrow in red is projected onto the image plane at two different camera positions. Due to simplification the aberrations of the camera lens was not taken into account. The base points of the original arrow and its images are situated in the same plane being indicated by the hatched triangle. Another plane is defined by the tips of the arrows. This *coplanarity*

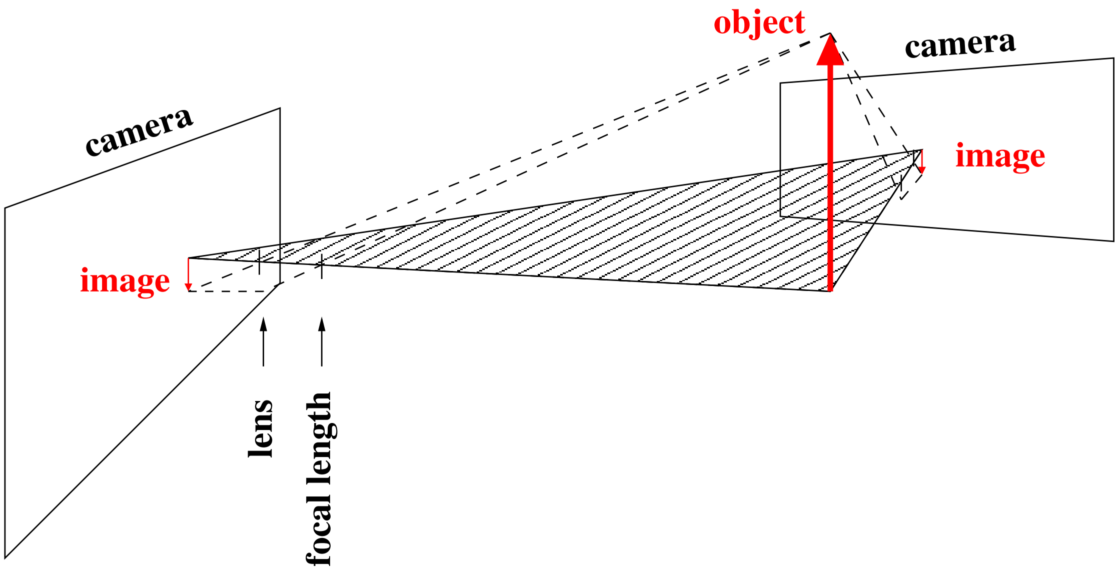

Figure B.2.: Co-planar condition in the photogrammetric position measurement. The sketch shows the projection of the object arrow in red onto the image plane at two different camera positions.

defines the relation of the object points and its images. The entity of those relations are comprised in the so-called col-linear equations that define the transformation between the object and image coordinates [82]. The solution of the system of equations in depicted in the reference. It is based on elementary geometry an performed automatically by the `PhotoModeler`, which is generating an instant 3D-model being visualised by a build-in viewer, is generated.

B.2.1 How to Do Photogrammetric Position Measurements

In a first step the **photos** have been taken as described in section B.1. Therefor adequate references were identified. Since the construction drawings of the GFIs, the Proton Drift Chambers (PDCs) and LAND were available, for such detectors the exterior corners were sufficient to recalculate the location of the respective active detector volume. The target position is supposed to be at the centre of the XB and all other detectors were directly identified by their active detection material. Additionally, makers were placed at positions of the setup with poor references in order to bridge these areas. Markers were also placed on the floor to identify the mean direction of the neutrons, fragments and protons behind ALADiN. Photo shootings were carried out in front of the magnet and behind it. In order to combine these data the respective ALADiN-chamber opening-windows were included to the measurements.

Subsequently, the **camera calibration** was carried out following the guidelines of the according `PhotoModeler` program as depicted before. It has to be performed for each set of internal camera parameters. The calibration file contains corrections for distortion effects like the aberrations of the lens and is included in the next analysis steps.

For the **referencing** between different camera positions a so-called point-based project in the `PhotoModeler` was created, in which the references were linked between the photos by hand. Photos with biggest amount of data, *i.e.* contained markers and reference points were preferred. An example photo is shown in figure B.3, in which the corners of the PDCs and GFIs have been tagged.

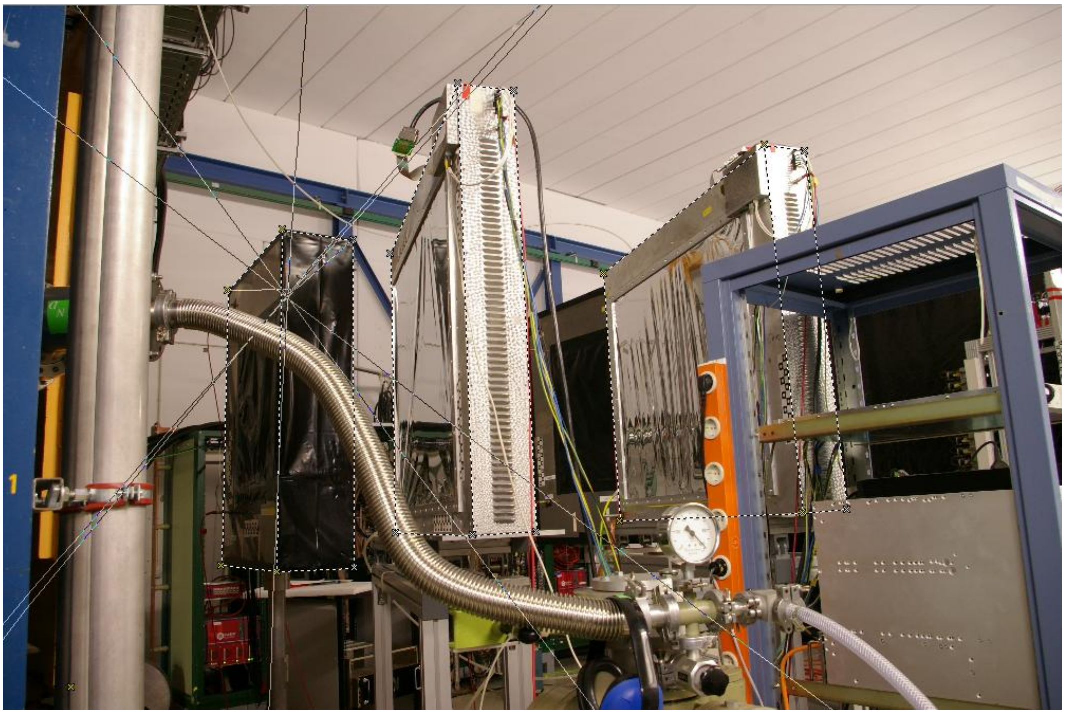

Figure B.3.: Referencing between camera positions in the `PhotoModeler`. The references at the corners of the PDCs and GFIs (crosses) are conducted by dashed lines to guide the eye.

The same (numbered) markers were identified in different photos to define the respective detector. On the very left a part of the yellow ALADiN frame can be seen. It was used to define the detector positions with respect to the dipole magnet. The resulting 3D-model was cross-checked in an instant viewer of the `PhotoModeler`. In total three projects were generated:

1. detector positions behind ALADiN with respect to the rear window of the magnet chamber,
2. detector positions in front of ALADiN with respect to the front window of the magnet chamber,
3. detector positions in the target area (focal length was 35 mm).

The models (1.-3.) are presented in figures B.4 - B.6.

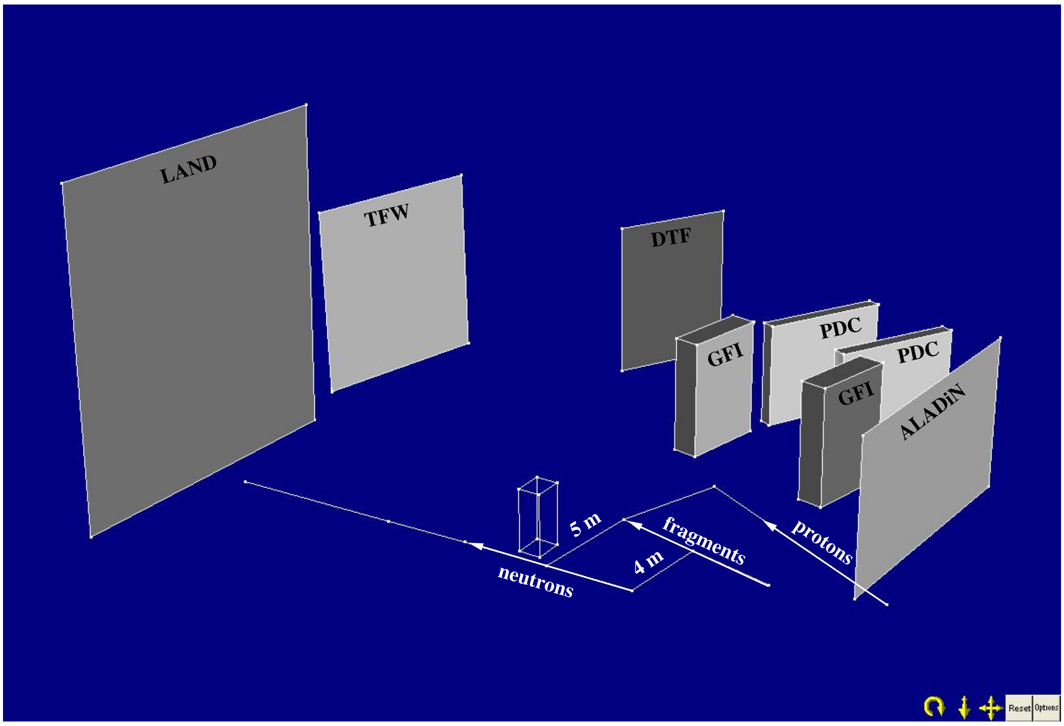

Figure B.4.: Model of the area behind ALADiN. The volumes are labeled and the directions of the neutrons, fragments and protons are indicated on the floor where also the distance with respect to the centre of ALADiN is given.

The `PhotoModeler` program internally calculated **residue** in units of pixels for each reference on all photos. Such residue are the difference between the calculated position using information from the remaining photos and the actual reference on the photo. The residue were minimised in an iterative adaption of the position of the corresponding reference. The maximum residue in the presented data was less than three pixels. The difference may be attributed to deficient camera calibration parameters.

Afterwards, the models 1.-3. were **scaled and oriented** properly using the length of the rear- and front-window of ALADiN for one and two, respectively. The model of the target area was scaled by means of the waver length of the DSSSDs and the axis in units of cm were rotated to a right-handed coordinate system (x, y, z) as used in the `Land02` analysis software. Therefor, the direction of the incoming beam was defined the z-axis and the x- and y-axes point up the left and up in beam direction, respectively.

Finally, all measurements were combined *via* **interface** rectangles, *i.e.* objects being included in both models and, hence, used to link these models. ALADiN had to be bypassed in the photogrammetric measurement, because the areas in front of the magnet and behind it hardly could be accessed visually at the same time due to the size of the magnet. In addition, a separate position measurement of the detectors around the target was carried out for higher precision in this area. The measurements in front of and behind the dipole magnet were conduced by means of its $\vec{B}$-field chamber. A construction

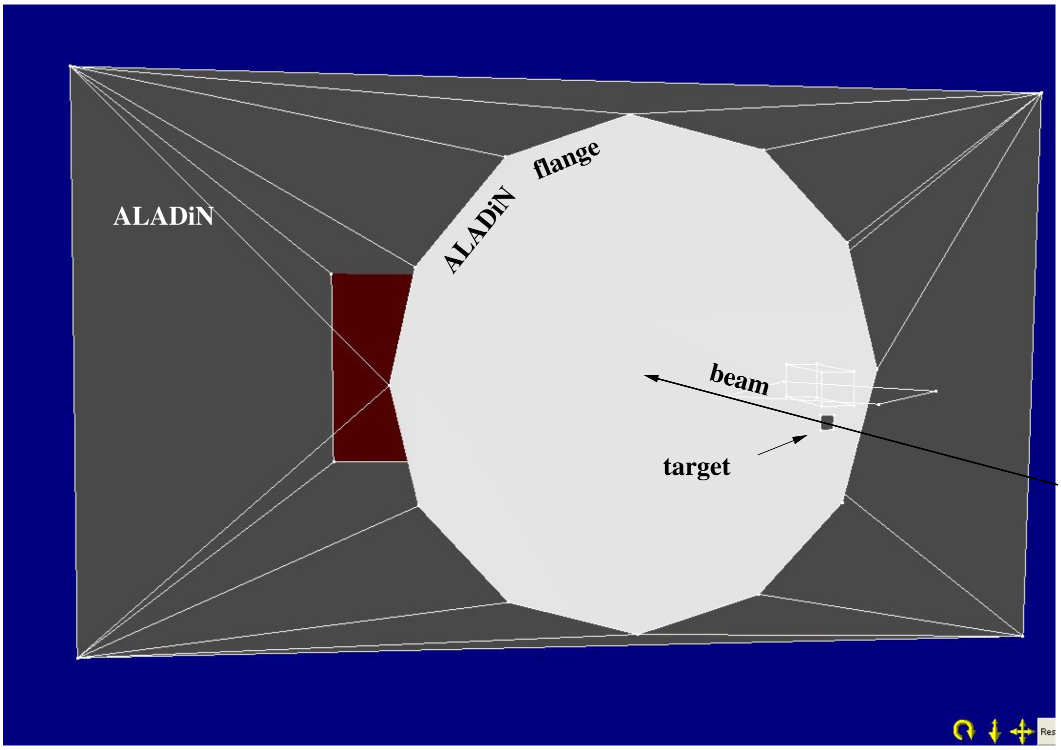

Figure B.5.: Model of the area in front of ALADiN. The reconstructed volumes are label-led.

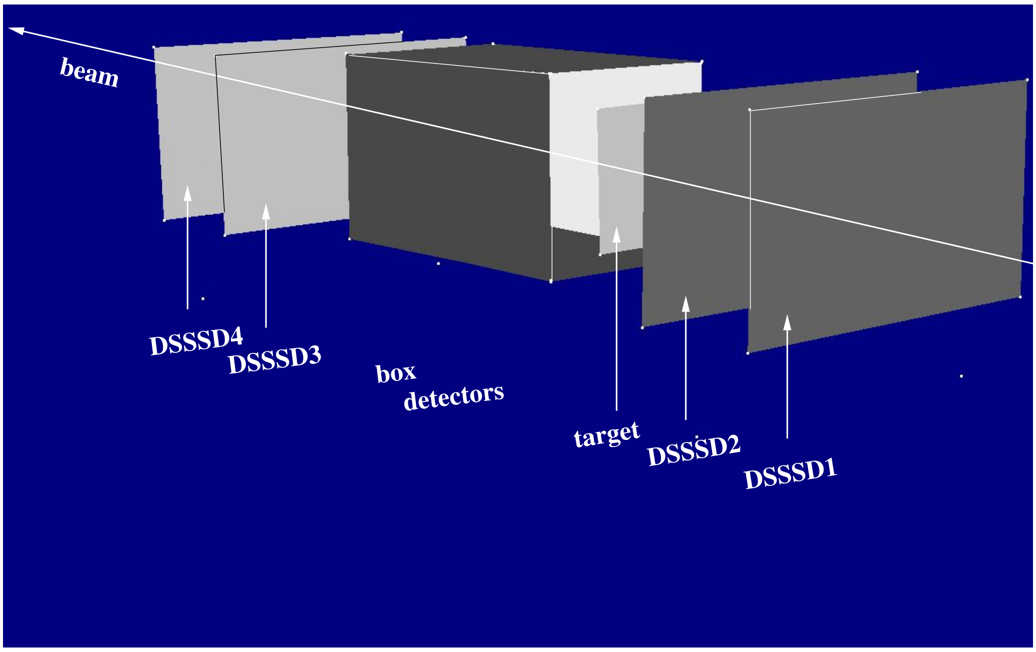

Figure B.6.: Model of the detectors in the target area. The in-beam DSSSDs and the target are labeled and the four DSSSDs around the beam line after the target are named box detectors.

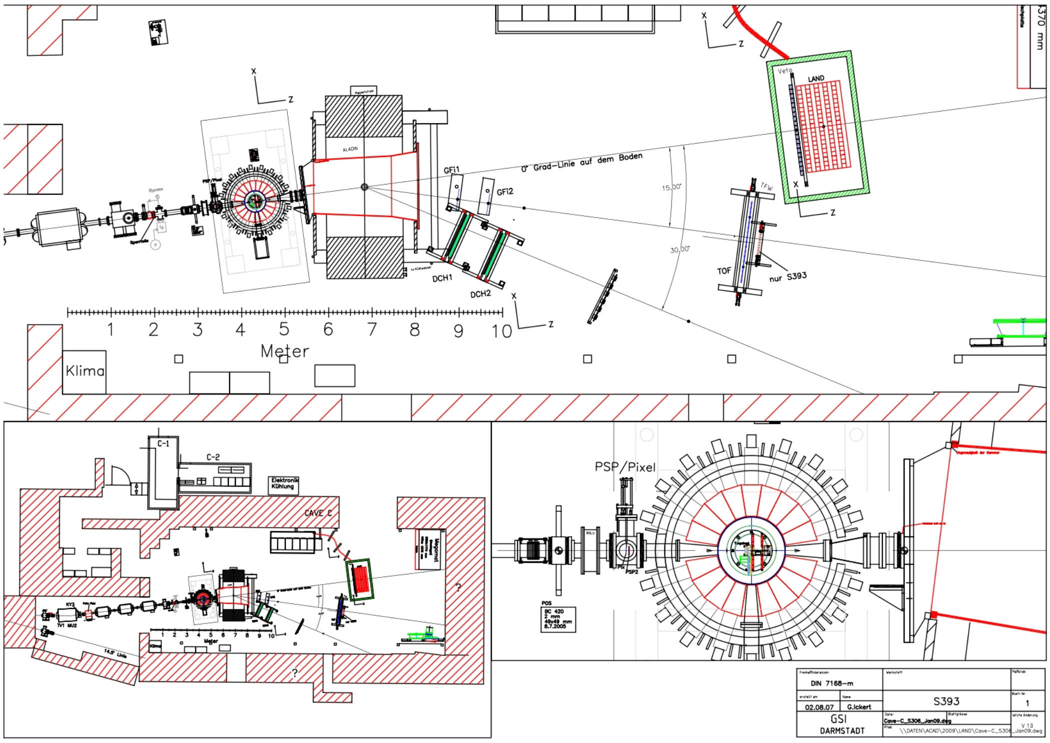

Figure B.7.: CAD drawing of the experimental setup [83]. ALADiN and particularly its $\vec{B}$-field chamber (red) are shown in the centre of the upper panel.

drawing of the experimental setup is shown in figure B.7 [83] The dipole magnet and particularly its $\vec{B}$-field chamber (red) are shown at the centre of the upper panel. The rear window of ALADiN taken from figure B.7 was matched with the according position measurements in model one. And the front window was conducted with its equivalent in model two, where also the position measurement in the target area was fit to. Therefor a rectangle formed by the holding structure of the DSSSDs served as an interface. In general, the interfaces were either reconstructed from position measurements or taken from the construction drawing B.7. A fit procedure was applied to match the interfaces, since the objects from the `PhotoModeler` reconstruction didn't necessarily form exact rectangles. In this procedure, the rectangles from two models were visually matched in a first step. Afterwards the deviation of the corners was minimised in an iterative algorithm recalculating the deviation for each randomly applied offset in (x, y, z) of the models with respect to each other. The models were then shifted by the according offset if it's necessary. The iteration was repeated until the deviation converged. Note that the average deviation for all points of the interfaces was smaller than the position uncertainty of these points from the `PhotoModeler` (see table B.1).

The detector positions were defined by the centres of the active volumes and the reconstructed positions are listed in table B.1 along the position uncertainties from the `PhotoModeler`. These positions can directly be handed to the `Land02` and `tracker` software. The target position refers to the surface in beam direction, because this coordinate was the same for all targets. The first four DSSSDs were located in the beam line, counting from the one being hit first by the incoming beam. The box DSSSDs were labeled according to the ROLU-detector logic. Hence, number five was right in beam direction, number six was on top of the box and number seven and eight were the left and bottom detector, respectively. GFI1 and PDC1 were closer to ALADiN than their companions. Note that GFI2 was moved during the experimental campaign and the listed value refers to the situation at the end of the beam time. It is rather adequate for the analysis of the so-called S389 experiment and in the work presented here, GFI2 was set at $(x, y, z) = (-75.3, 0.0, 526.6)$ cm.

Detector	(x,y,z) [cm]	$\Delta(x,y,z)$ [cm]	Detector	(x,y,z) [cm]	$\Delta(x,y,z)$ [cm]
DSSSD1	(0.02, 0.03, -6.44)	0.05	GFI1	(-56.5, 2.3, 467.1)	0.9
DSSSD2	(-0.03, 0.01, -3.68)	0.05	GFI2*	(-95.1, 3.3, 616.6)	0.9
Target	(0.00, 0.00, 0.00	0.05	PDC1	(-138.5, 3.3, 459.1)	0.9
DSSSD3	(0.06, -0.09, 11.11)	0.05	PDC2	(-171.2, 3.8, 547.0)	0.9
DSSSD4	(0.13, -0.06, 13.88)	0.05	TFW	(-232, 7, 1121)	1.7
DSSSD5	(-2.12, -0.02, 4.58)	0.05	DTF	(-304, 0, 789)	1.7
DSSSD6	(-0.07, 2.10, 4.53)	0.05	LAND	(5, 0, 1337)	5
DSSSD7	(2.05, 0.05, 4.50)	0.05			
DSSSD8	(-0.02, -2.01, 4.54)	0.05	ALADiN	(0, 0, 256)	2

Table B.1.: Detector positions and uncertainties from the photogrammetric measurement. In addition, crucial points (target, ALADiN) of the experimental setup are given.

Detector	x [cm]	y [cm]	z [cm]
DSSSD	7.2045	4.136	0.3
GFI	83.2	116.2	26.0
PDC	125.8	103.4	13.8

Table B.2.: Dimensions of the DSSSD wafers and the GFI and PDC housings [83].

The angle of the dipole magnet with respect to the zero-degree line was calculated from the depicted measurement, too. As the outcome, ALADiN is rotated by 6.0° with respect to the x-axis. Usually, this rotation is set to 7.0°. However, an earlier measurement by a specialised company confirms the former value and excludes the latter [84]. In table B.1, the position of ALADiN refers to the so-called centre of the dipole. The magnet is attributed to this coordinate in a simplified treatment of its geometry in the `tracker` software. All active detector volumes from the photogrammetric position measurement are presented in figure B.8, showing the setup relevant for projectile (pink), fragment (pink) and neutron (green) detection of Coulomb-dissociation reactions. The target is located at the centre of the XB, whose left hemisphere is cut for illustration purpose. ALADiN is indicated by its frame and opening windows. The inset is a zoom on the detectors for projectile identification and the target area. A scale is given in addition, because the presented data refers to the measured detector positions and their real active volumes.

B.3 Discussion

The `PhotoModeler` software provided the uncertainty of each used point, *i.e.* position. In table B.2, the dimensions of the GFI and PDC housings as well as the DSSSD wafers from construction drawings are given. The uncertainties in (x,y,z) for the GFIs and PDCs are 1 mm and for the DSSSD 1 μm [83].

The detector dimensions were calculated from `PhotoModeler` data and compared to the corresponding construction drawings. This difference is named Δ_1 in figure B.9 and presented with Δ_2, which is the corresponding uncertainty from the points in the `PhotoModeler`. The values for the GFIs, the PDCs and the DSSSDs are marked by blue, red and black crosses, respectively. The one-to-one correlation (black line) was added to guide the eye. The Δ_i $(i = 1,2)$ are clearly correlated for the considered detectors and respective areas in the calculated 3D-model. Other regions of the experimental hall were not considered

---

[*] The detector was moved during the experiment. The listed value refers to the situation at the end of the experimental campaign, when the photo shooting took place.

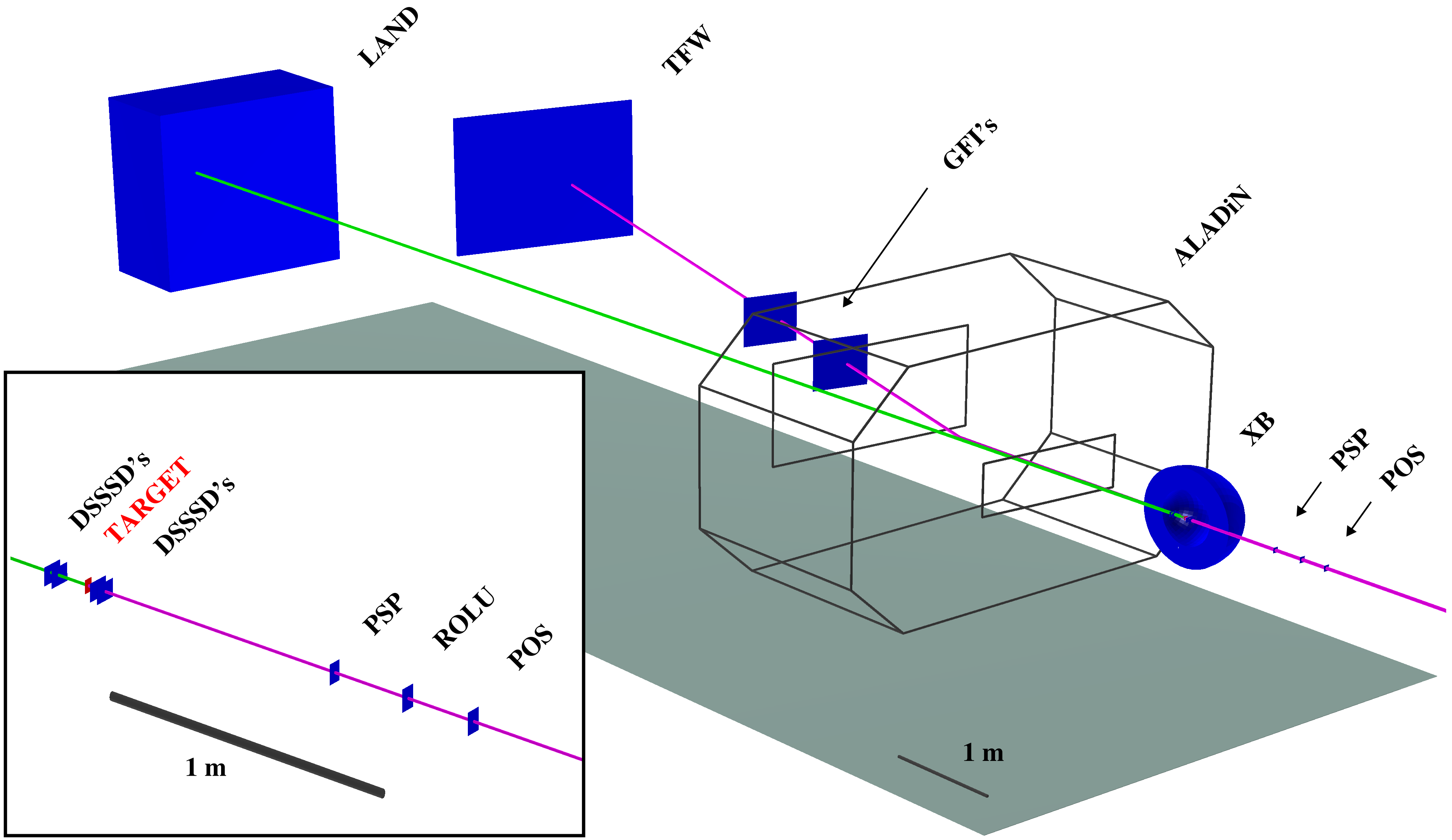

Figure B.8.: R^3B-LAND setup at Cave C relevant for projectile, fragment (pink) and neutron (green) detection. The target is located at the centre of XB and ALADiN is indicated by its frame and opening windows. The inset is a zoom on the detectors for projectile identification and the target area.

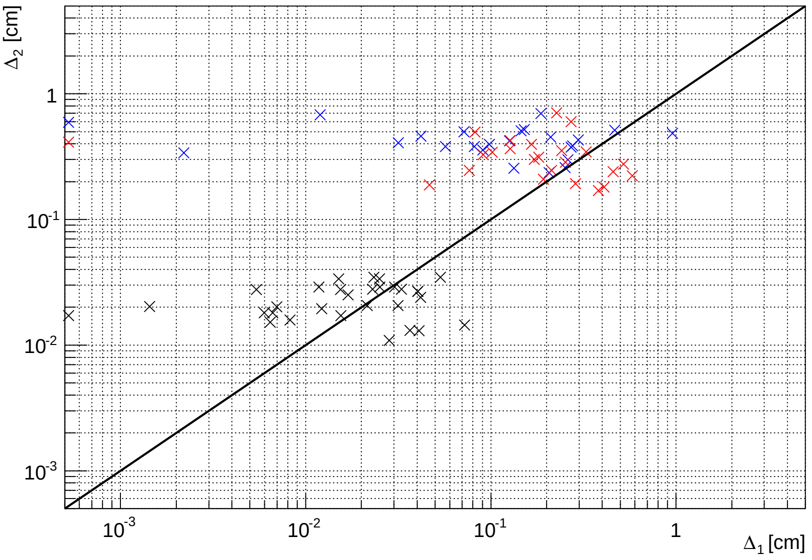

Figure B.9.: The uncertainty Δ_1 was extracted from the according position uncertainties in the `PhotoModeler` and Δ_2 resulted from the comparison of the extracted lengths from the photos with the nominal detector dimension [83]. The colors are explained in the text.

due to poor references. As can be seen, the uncertainties in table B.1 are rather an upper limit and do not refer to the mean values of the uncertainty distributions being 0.02 cm for the DSSSDs, 0.3 cm in the case of the PDCs and 0.4 cm for the GFIs. Furthermore, the `PhotoModeler` tends to overestimate the position uncertainty and provides a conservative estimation of the position error. For that reasons the uncertainties from the photogrammetric method were considered reliable and this conclusion was also drawn for the rest of the setup. Note that the 3D-model from the photos can easily be deformed in cases where the objects cannot be well-defined by different views. Concerning this problem the GFIs and PDCs were most critical in the work presented here, because the configuration of detector housings, supporting structure and readout electronics is most compact in this area of the experimental setup (see figure B.3).

Even though the lengths were reproduced correctly within uncertainties from the photos, angular distortions may remain in the generated 3D-model. Such distortions were identified in the present analysis by means of the housings of the GFIs and PDCs. Therefor the difference $\Delta\theta = \theta_l - \theta_r$ of facing angles in the same plane as illustrated in figure B.10 was calculated for the (x, y, z)-direction. If the model is deformed, the $\Delta\theta$ will systematically deviate from zero. In figure B.12, the differences $\Delta\theta$ for the x-direction in the upper panel, the y-direction in the middle panel and the z-direction in the lower panel are shown. The deviations from zero result from position uncertainties and are on average biggest in z-direction. Nevertheless, no general trend can be seen and the position data presented here were not considered to be angular distorted.

The detector positions from the photogrammetric measurement were finally compared to those from a more conventional position measurement with a laser rangefinder [83]. In figure B.11, the deviations of the detector positions behind ALADiN in a top view on the setup is shown. The present results (brown) deviate significantly from the former measurement (red) and the difference is biggest for the PDCs. The gap between GFI2 and PDC2 is smaller than given from the technical drawing, which can be seen on

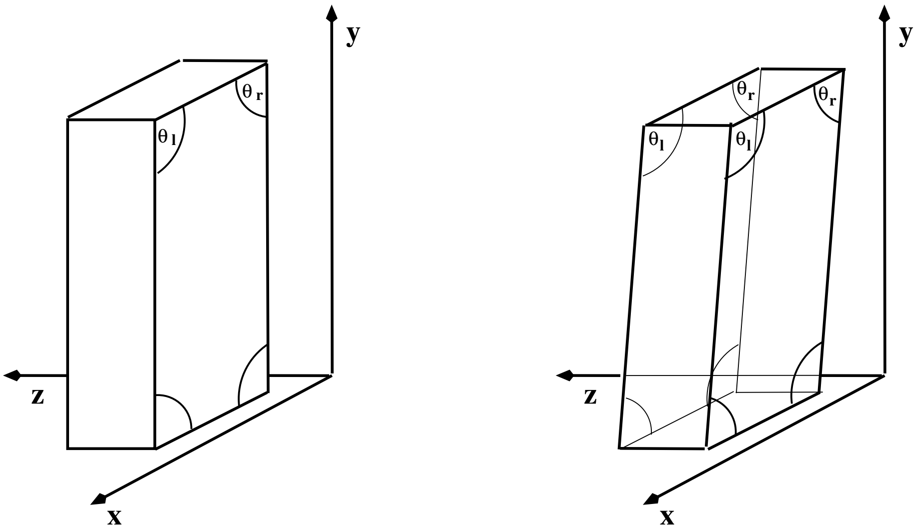

Figure B.10.: (Left) Original detector housing of the GFI. (Right) If the 3D-model is deformed, the difference $\Delta\theta = \theta_l - \theta_r$ will be systematically non-zero.

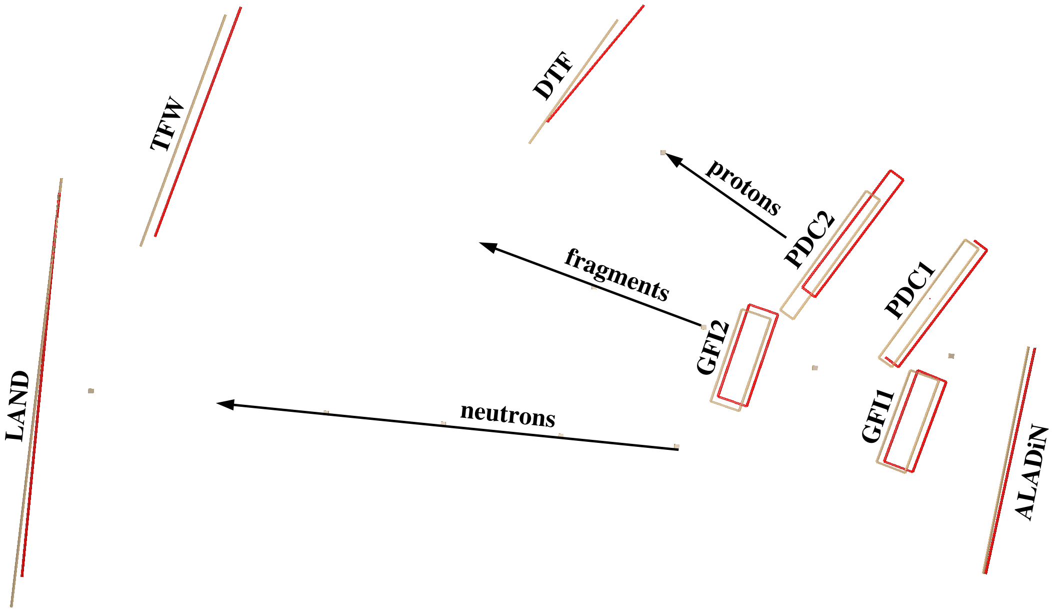

Figure B.11.: Deviation of the positions in the CAD drawing and the `PhotoModeler` measurement. Data from the analysis presented here (brown) is compared to the outcome of a measurement with a laser rangefinder (red) [83].

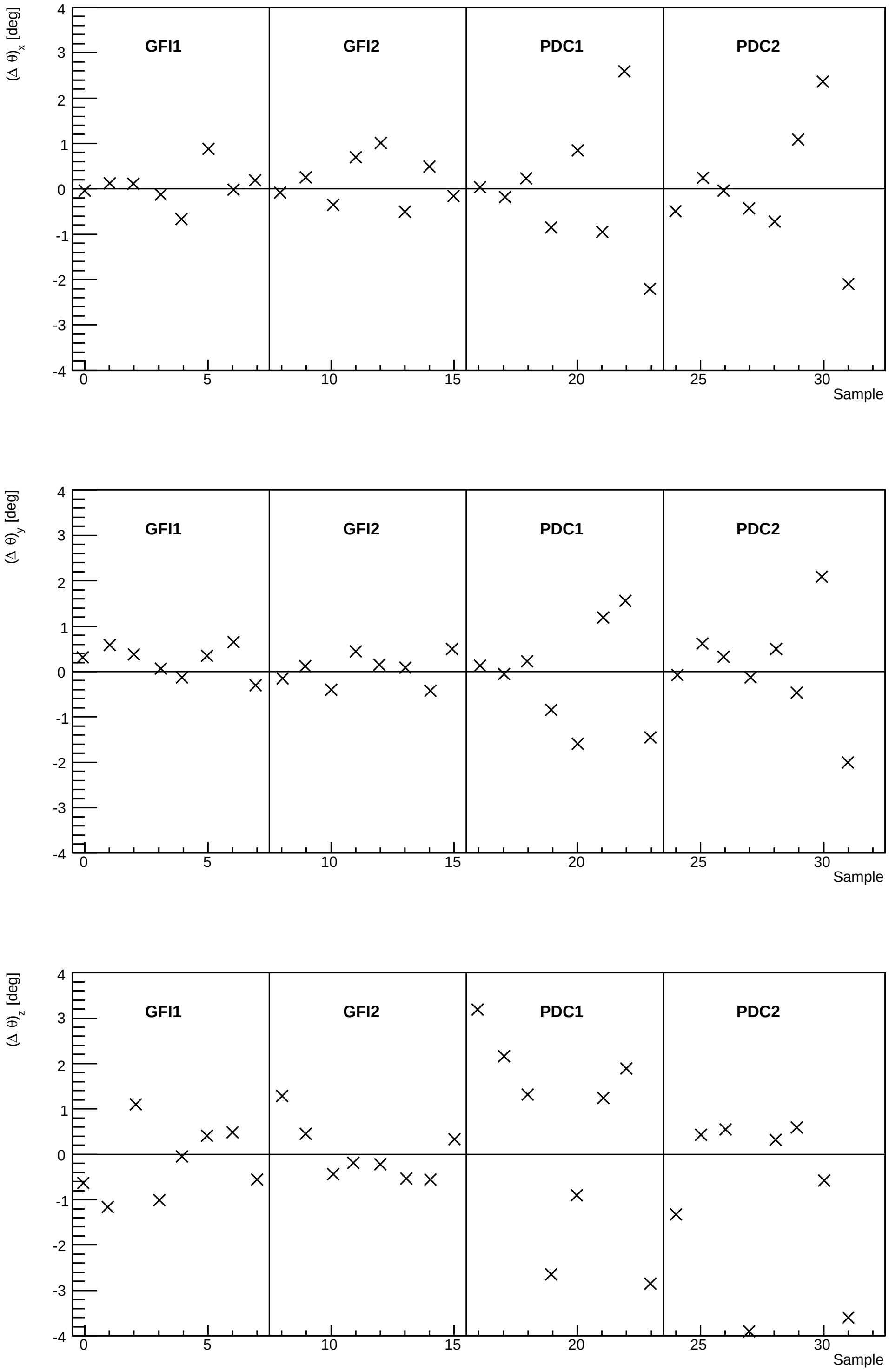

Figure B.12.: Angular distortion $\Delta\theta$ of the 3D-model for the GFIs and PDCs in x-direction (upper panel), y-direction (middle panel) and z-direction (lower panel).

photos from top of ALADiN. The area right behind ALADiN is difficult to handle in the photogrammetric procedure and the spatial limitations from the compact arrangement of detectors, supporting structures and readout electronics significantly effects the accuracy of conventional measurements, too.

B.3.1 Outlook

The accuracy of 0.1 cm of the construction drawings of the detectors defines the required position uncertainty for upcoming measurements based on the photogrammetric method. The problem of lacking references and angular distortions can be overcome with fixed position markers spread in the entire experimental hall. In this way, an immovable model can be created and afterwards the detectors could be distributed. Fixed markers on their housing would simplify the identification of the detectors. These markers should be visually accessible from various directions and, hence, mounted around the corners of the housing, which were already used in the present analysis. The active detection volume can then be reconstructed from the corresponding construction drawings. This referencing system is more handy in the photogrammetric measurement, but on the other hand prone to breakdown then the detectors are moved. Note that the accuracy of the present analysis was mostly hampered by deficient references.

Concerning *any* camera equipment the calibration of the internal camera parameters is supposed to influence the performance strongest. This calibration defines the area on the photos which can be used safely for the analysis. An unsuited calibration may restrict the effective focal length, since just a small part of the image can be utilised for the measurement. Present data were taken with consumer equipment that may already be suited to obtain a position uncertainty of 0.1 cm in the entire setup, because the results for the separate measurement at the target area were certain by 0.05 cm.

The procedure can be automated with coded markers, which are unambiguously identified by an analysis software. The present results were obtained from three different position measurements utilising in total around 500 uncoded markers. Hence, such an automating would provide significant saving of time, especially for consecutive measurements.

Bibliography

[1] E. M. Burbridge et al. Synthesis of the Elements in the Stars. Rev. Mod. Phys., 29:547–605, 1957.

[2] M. Arnould and S. Goriely and K. Takahashi. The r-Process of Stellar Nucleosynthesis. Phys. Rep., 450:97–213, 2007.

[3] `http://www.nndc.bnl.gov/nudat2/`. Accessed: 07.01.2014.

[4] M. Terasawa et al. New Nuclear Reaction Flow During r-Process Nucleosynthesis in Supernovae. Ap. J., 562:470–479, 2001.

[5] T. Otsuka et al. Magic Numbers in Exotic Nuclei and Spin-Isospin Properties of the NN Interaction. Phys. Rev. Lett., 87:082502, 2001.

[6] B. S. Meyer et al. r-Process Nucleosynthesis in the High-Entropy Supernova Bubble. Ap. J., 399:656, 1992.

[7] K. Sumiyoshi et al. Hydrodynamical Study of Neutrino-Driven Wind as an r-Process Site. PASJ, 52:601–611, 2000.

[8] T. Nakamura et al. Coulomb Dissociation of ^{19}C and its Halo Structure. Phys. Rev. Lett., 83:1112–1115, 1999.

[9] T. Sasaqui et al. Sensitivity of r-Process Nucleosynthesis to Light-Element Nuclear Reactions. Ap. J., 634:1173–1189, 2005.

[10] A. Klimkiewicz et al. Nuclear Symmetry Energy and Neutron Skins Derived from Pygmy Dipole Resonances. Phys. Rev. C, 76:051603, 2007.

[11] R. Reifarth et al. The ^{14}C(n, γ) Cross Section between 10 keV and 1 MeV. Phys. Rev C, 77:015804, 2008.

[12] U.D. Pramanik et al. Coulomb Breakup of the Neutron-Rich Isotopes ^{15}C and ^{17}C. Phys. Lett. B, 551:63–70, 2003.

[13] M. Wiescher and J. Görres and F. K. Thielemann. Capture Reactions on ^{14}C in Nonstandard Big Bang Nucleosynthesis. Ap. J., 363:340–343, 1990.

[14] E. Fermi. On the Theory of Collisions between Atoms and Electrically Charged Particles. Nuovo Cimento, 2:143–158, 1924.

[15] C. F. Weizsäcker. Ausstrahlung bei Stößen sehr Schneller Elektronen. Z. Phys., 88:612–625, 1934.

[16] J. D. Jackson. Klassische Elektrodynamik, volume 2. Walter de Gruyter, 1983.

[17] C. J. Benesh and B. C. Cook and J. P. Vary. Single Nucleon Removal in Relativistic Nuclear Collisions. Phys. Rev. C, 40:1189–1206, 1989.

[18] C. A. Bertulani and G. Baur. Electromagnetic Processes in Relativstic Heavy Ion Collisions. Phys. Rep., 163(5–6):299–408, 1988.

[19] W. J. Llope and P. Braun-Munzinger. Electromagnetic Dissociation of Relativistic Heavy Ions. Phys. Rev. C, 41:2644–2653, 1990.

[20] S. Typel. CDXS+ Version 6.30. unpublished, 2007.

[21] S. Typel and G. Baur. Higher Order Effects in Electromagnetic Dissociation of Neutron Halo Nuclei. Phys. Rev. C, 64:024601, 2001.

[22] J. A. Tostevin. Core Excitation in Halo Nucleus Break-up. J. Phys. G, 25:735–739, 1999.

[23] C. Bertulani and L. Canto. Semiclassical Calculation of Coulomb Break-up of Weakly-Bound Nuclei. Nucl. Phys. A, 539:163–176, 1992.

[24] S. Typel. Remarks on Cross Sections and Reaction Rates. unpublished, 2010.

[25] T. Rauscher and F.-K. Thielemann. Astrophysical Reaction Rates from Statistical Model Calculations. Atom. Nucl. Data, 75:1–351, 2000.

[26] `https://www.gsi.de/start/aktuelles.htm`. Accessed: 07.10.2010.

[27] FRS Log Book S393/S306. unpublished, 2010.

[28] H. Geissel et al. The GSI Projectile Fragment Separator (FRS). NIM B, 70:286–297, 1992.

[29] `http://www-w2k.gsi.de/frs-setup/`. Accessed: 22.01.2014.

[30] T. Aumann. Neutron-Rich Nuclei at and Beyond the Dripline in the Range Z=4 to Z=10 Studied in Kinematically Complete Measurements of Direct Reactions at Relativistic Energies. Accessed: 23.01.2014.

[31] T. Aumann. Reactions with Fast Radioactive Beams of Neutron-Rich Nuclei. Eur. Phys. J. A, 26:441–478, 2005.

[32] S. Altstadt. ^{13,14}B(n,γ) via Coulomb Dissociation to Constrain the Astrophysical r-Process. PhD thesis, Goethe Universität Frankfurt, 2014.

[33] G. Knoll. Radiation Detection and Measurement, volume 3. John Wiley & Sons Inc., 2000.

[34] T. Doke et al. A New Two-Dimensional Position Sensitive Detector with a Good Linear Response. NIM A, 261:605–609, 1987.

[35] J. Alcaraz et al. The Alpha Magnetic Spectrometer Silicon Tracker: Performance Results with Protons and Helium Nuclei. NIM A, 593:376–398, 2008.

[36] D. Habs and F. Stephens and R. Diamond. A Proposal for a Crystal Ball Detector System. Technical Report, LBL-8945, 1979. Lawrence Berkeley Laboratory.

[37] J. Cub et al. A Large-Area Scintillating Fibre Detector for Relativistic Heavy Ions. NIM A, 402:67–74, 1998.

[38] K. Mahata et al. Position Reconstruction in Large-Area Scintillating Fibre Detectors. NIM A, 608:331–335, 2009.

[39] Th. Blaiche et al. A Large Area Detector for High-Energy Neutrons. NIM A, 314:136–154, 1992.

[40] H. Essel and N. Kurz. The General Purpose Data Acquisition System MBS. IEEE NPSS, 11:475–478, 1999.

[41] H. Johannson. Hunting Tools Beyond the Driplines. PhD thesis, 2010. Chalmers University of Technology.

[42] H. Johannson. The DAQ Always Runs. Licentiate thesis, 2008. Chalmers University of Technology.

[43] P. Pawlowski et al. Neutron Recognition in the LAND Detector for Large Neutron Multiplicity. NIM A, 694:47–54, 2012.

[44] F. Wamers. Quasi-Free-Scattering and One-Proton-Removal Reactions with the Proton-Dripline Nucleus ^{17}Ne at Relativistic Beam Energies. PhD thesis, 2011. Technische Universtät Darmstadt.

[45] `http://ralfplag.de/tracker/`. Accessed: 27.10.2013.

[46] A. Ozawa et al. Measurements of Interaction Cross Sections for Light Neutron-Rich Nuclei at Relativistic Energies and Determination of Effective Matter Radii. Nucl. Phys. A, 691:599–617, 2001.

[47] R. Palit et al. Exclusive Measurement of Breakup Reactions with the One-Neutron Halo Nucleus ^{11}Be. Phys. Rev. C, 68:034318, 2003.

[48] M. Zinser et al. Invariant-Mass Spectroscopy of ^{10}Li and ^{11}Li. Nucl. Phys. A, 619:151–176, 1997.

[49] K. Boretzky. Systematische Untersuchungen zur Coulombanregung der Zwei-Photonen-Dipolresonanz in ^{208}Pb. PhD thesis, 1995. Goethe-Universität in Frankfurt am Main.

[50] A. Ozawa et al. Measurement of the Reaction Cross Section of ^{18}C and Observations of Fragments from ^{17}C and ^{18}C at 80 AMeV. Phys. Rev. C, 78:054313, 2008.

[51] C. Wu et al. Study of the Density Distribution of ^{17}C from Reaction Cross Section Measurement. Nucl. Phys. A, 739:3–14, 2004.

[52] D. Bertini. R3BRoot, Simulation and Analysis Framework for the R3B Experiment at FAIR. J. Phys., 331:032036, 2011.

[53] C. Lederer and J. Hollander and I. Perlman. Table of Isotopes, volume 2. John Wiley & Sons Inc., 1994.

[54] R. Thies. Prototype Tests and Pilot Experiments for the R^{3}B Scintillator-Based Detection Systems. master thesis, 2011. Chalmers University of Technology.

[55] G. Heusser. Low-Radioactivity Background Techniques. Nucl. Part. Sci., 45:543–590, 1995.

[56] H.T. Fortune et al. Spectroscopy of ^{16}C. Phys. Lett. B, 70:408–410, 1977.

[57] D. Rossi. Investigation of the Dipole Response of Nickel Isotopes in the Presence of a High-Frequency Electromagnetic Field. PhD thesis, 2010. Gutenberg-Universität in Mainz.

[58] J. Cub and K. Grimm and E. Zude. The Detection of Neutrons of Low and High Multiplicities with the LAND-Detector. GSI Sci. Rep., page 275, 1994.

[59] B. Alpat et al. High-Precision Tracking and Charge Selection with Silicon Strip Detectors for Relativistic Ions. NIM A, 446:522–535, 2000.

[60] A. Heikkinen and V. Karimäki. Fine Calibration of Detector Positions by Tracks in Helsinki Silicon Beam Telescop. CMS Note, 21:498–516, 1999.

[61] H. Weick. private communication.

[62] `http://web-docs.gsi.de/~weick/atima/`. Accessed: 20.12.2012.

[63] O.B. Tarasov and D. Bazin. LISE++: Radioactive Beam Production with In-Flight Separators. NIM B, 266:4657–4664, 2008.

[64] D. Bazin et al. One-Neutron Halo of ^{19}C. Phys. Rev. Lett., 74:3569–3572, 1995.

[65] T. Nakamura et al. Coulomb Dissociation of Halo Nuclei. Nucl. Phys. A, 722:C301–C307, 2003.

[66] D. Bazin et al. Probing the Halo Structure of ^{19,17,15}C and ^{14}B. Phys. Rev., 57:2156–2164, 1998.

[67] V. Maddalena et al. Single-Neutron Knockout Reactions: Application to the Spectroscopy of ^{16,17,19}C. Phys. Rev. C, 63, 2001.

[68] D.R. Tilley, H.R. Weller, and CM. Cheves. Energy Levels of Light Nuclei A = 16–17. Nucl. Phys. A, 565:1–184, 1993.

[69] H. Ueno et al. β-Delayed Neutron and γ-Ray Spectroscopy of ^{17}C Utilizing Spin-Polarized ^{17}B. Phys. Rev. C, 87:034316, 2013.

[70] D.P. Balamuth et al. Angular Correlation Study of Levels in ^{16}C. Nucl. Phys. A, 290:65–71, 1977.

[71] Zhongzhou Ren, Z.Y. Zhu, Y.H. Cai, and Gongou Xu. Relativistic Mean-Field Study of Exotic Carbon Nuclei. Nucl. Phys. A, 605:75–86, 1996.

[72] Cenxi Yuan et al. Shell-Model Study of Boron, Carbon, Nitrogen, and Oxygen Isotopes with a Monopole-Based Universal Interaction. Phys. Rev. C, 85:064324, 2012.

[73] A. K. Kerman. Pairing Forces and Nuclear Collective Motion. Ann. Phys., 12:300–329, 1961.

[74] B. R. Mottelson and S. G. Nilsson. Classification of the Nucleonic States in Deformed Nuclei. Phys. Rev., 99:1615–1617, 1955.

[75] Y. Kondo et al. One-Neutron Removal Reactions of ^{18}C and ^{19}C on a Proton Target. Phys. Rev. C, 79:014602, 2009.

[76] D.R. Tilley, H.R. Weller, and CM. Cheves. Energy Levels of Light Nuclei A = 18–19. Nucl. Phys. A, 595:1–170, 1995.

[77] M. Stanoiu et al. Study of Drip Line Nuclei through Two-Step Fragmentation. Eur. Phys. J. A, 20:95–96, 2004.

[78] S. Typel. private communication, 2014.

[79] A. Gade et al. Reduction of Spectroscopic Strength: Weakly-Bound and Strongly-Bound Single-Particle States Studied Using One-Nucleon Knockout Reactions. Phys. Rev. C, 77:044306, 2008.

[80] `http://igfae.usc.es`. Accessed: 23.04.2014.

[81] `http://www.photomodeler.com/index.html`. Accessed: 24.04.2014.

[82] T. Luhmann. Erweiterte Verfahren zur geometrischen Kamerakalibrierung in der Nahbereichsphotogrammetrie. In Bayerischen Akademie der Wissenschaften. professorial dissertation, 2010.

[83] G. Ickert. S393 Construction Drawing, 2010. GSI.

[84] O. Borodina. private communication, 2011.

Curriculum Vitae

Personal Data

Birthday	March 2nd 1981
Birthplace	Bad Muskau, Germany
Nationality	German

Studies

06-2010 -	PhD thesis in the field of nuclear astrophysics at the Nuclear-Reactions Department of the GSI Helmholtzzentrum für Schwerionenforschung in Darmstadt Title: “Measurement of (n,γ)-Rates of Light Neutron-Rich Nuclei for the r-Process Nucleosynthesis” Supervising Professors: Prof. Dr. Thomas Aumann and Prof Dr. Dr. h.c Norbert Pietralla, Institute for Nuclear Physics, Technical University Darmstadt, Germany
05/2010	Degree in physics: “Diplom-Physiker”
10/2008 - 12/2009	Diploma thesis at the Institute for Nuclear and Particle Physics at the Technical University Dresden, Germany Title: “Search for double-beta decays of cadmium-, zinc- and tellurium-isotopes with positron emission” Supervisor: Prof. Dr. Kai Zuber, Institute for Nuclear and Particle Physics, Technical University Dresden
10/2004 - 09/2008	Advanced studies in physics, Technical University Dresden
09/2004	“Vordiplom” (intermediate degree in physics)
04/2001 - 08/2004	Basic studies in physics, Technical University Dresden
10/2000 - 03/2001	Studies of solid waste management, Technical University Dresden, Germany

Civilian service

07/1999 - 06/2000	Hospital “Martin-Ulbrich” in Rothenburg

Education

06/1999	“Abitur” (final high-school exam). High-and Grammar school, “Städtisches Gymnasium” Rothenburg, Germany

Lebenslauf

Persönliche Daten

Geburtstag	02.03.1981
Geburtsort	Bad Muskau
Nationalität	deutsch

Schulbildung

06/1999	Abitur *Städtisches Gymnasium* Rothenburg

Zivildienst

07/1999 - 06/2000	*Martin-Ulbrich Haus* in Rothenburg

Studium

10/2000 - 03/2001	Studium der Abfallwirtschaft und Altlasten, Technische Universität Dresden
04/2001 - 08/2004	Grundstudium der Physik, TU Dresden
09/2004	Vordiplom
10/2004 - 09/2008	Hauptstudium der Physik, TU Dresden
10/2008 - 12/2009	Diplomarbeit am Institut für Kern- und Teilchenphysik der TU Dresden Titel: *Eine Suche nach Doppelbeta-Zerfällen von Cadmium-, Zink- und Tellur-Isotopen mit Positronen-Emission* Betreuender Professor: Prof. Dr. Kai Zuber, Institut für Kern- und Teilchenphysik, TU Dresden
05/2010	Studienabschluß: Diplom-Physiker
06/2010 -	Doktorarbeit in der nuklearen Astrophysik in der Abteilung Kernreaktionen am GSI Helmholtzzentrum für Schwerionenforschung in Darmstadt Titel: *Messung von (n,γ)-Übergangsraten Leichter Neutronenreicher Kerne für die r-Proceß Nukleosynthese* Betreuende Professoren: Prof. Dr. Thomas Aumann and Prof Dr. Dr. h.c Norbert Pietralla, Institut für Kernphysik, Technische Universität Darmstadt

Erklärung zur Dissertation

Hiermit versichere ich, die vorliegende Dissertation ohne Hilfe Dritter nur mit den angegebenen Quellen und Hilfsmitteln angefertigt zu haben. Alle Stellen, die aus Quellen entnommen wurden, sind als solche kenntlich gemacht. Diese Arbeit hat in gleicher oder ähnlicher Form noch keiner Prüfungsbehörde vorgelegen.

Darmstadt, den 27.05.2014

(M. Heine)